Author:
Aghaei Meibodi, Arman

Title:
Geometrical exploration of a generalized nonlinear multi-span bridge system under multi-support excitation

Geometrical exploration of a generalized nonlinear multi-span bridge system under multi-support excitation

By

Arman Aghaei Meibodi

A dissertation is submitted in partial fulfillment of the
requirement for the degree of
Doctor of Philosophy

September 2021

Geometrical exploration of a generalized nonlinear multi-span bridge system under multi-support excitation

by

Arman Aghaei Meibod

DECLARATION

This dissertation is the result of my own work and includes nothing, which is the outcome of work done in collaboration except where specifically indicated in the text. It has not been previously submitted, in part or whole, to any university of institution for any degree, diploma, or other qualification.

In accordance with the Department of Engineering guidelines, this thesis is does not exceed 65,000/80,000 (delete as appropriate) words, and it contains less than 150 figures.

Signed: Arman Aghaei Meibodi

Date: Apr. 15, 21

CONTENTS

ABSTRACT

This study uses a generalized and parametrized reduced-order model to evaluate the effects of asynchronous excitation on the transversal response of bridge structures. Bridge geometry parametric regions, corresponding conceptually to valley profile shapes, are explored. Both modal and bounding analyses, which are dependent on bridge geometry alone, are employed to highlight regions where the first mode is anti-symmetrical and the likely error between identical support excitation (ISE) and multi-support excitation (MSE) analyses is large.

Pier hysteresis is then incorporated into this generalized dynamic system to enable an inelastic time-history analysis of an MDOF bridge under multi-support seismic excitation. The hysteretic, nonlinear, relationship of piers is phenomenologically captured by a calibrated Bouc-Wen model.

A deterministic approach using real spatiotemporal ground motions recorded at the SMART-1 array, Taiwan, is employed as an alternative to a stochastic methodology used in current provision codes.

Benchmark experimental test data, using the multiple support excitation rig of a four-span bridge and SMART-1 array excitation, is used to validate/calibrate the proposed reduced-order model. An operational modal analysis is conducted to obtain least-square estimates of these key dynamic parameters using a Levenberg–Marquardt algorithm.

Numerical time history analyses, using a heuristic bridge case and spatiotemporal ground motion from the SMART-1 array, are employed. These analyses confirm that in parametric configurations where the first mode is anti-symmetrical the error between MSE and ISE is often larger. This confirms the utility of geometry only modal and bounding analyses in identifying critical regions.

Finally, Incremental Dynamic Analysis (IDA) is then performed to identify the performance levels at which this system transitions from elastic to inelastic behavior. A parametric study is then performed to explore the effect of the spatial variability of the ground motion while the pier hysteresis is taken into account.

ACKNOWLEDGEMENTS

I would like to express my deep and sincere gratitude to my research advisor, Dr Nicholas A. Alexander for his infinite patience and his generous supports during my Ph.D. study. I appreciated him for his invaluable guidance, encouragement and immense knowledge that provide me with a strong foundation for conducting a challenging and in-depth research project. His academic and personal qualities have deeply inspired me. It was a great privilege and honor to be his student.

I would like to thank Dr. James Norman and Dr. Adam John Crewe for sharing experimental data. I am extremely grateful to Dr. James Norman for the insightful discussions and invaluable contribution to interpreting of experimental data. I am extending my thanks to Faculty of Engineering at the University of Bristol for their support during my research work.

I wholeheartedly thank my parents for their love, sacrifices, and caring during my research. Without their encouragement and prayers, it is almost impossible to finish my study during this difficult times. I am immensely grateful to my sisters, despite the geological distance, were contiously encouraging me to finisnish this thesis successfully.

LIST OF TABLES

LIST OF FIGURES

Chapter 1

Introduction

1.1 MOTIVATION AND BACKGROUND

The influence of the spatial variation of seismic ground motion time-series on the dynamic response of generic life-line structures, such as bridges has been studied extensively for several decades (Leger et al., 1990, Monti et al., 1996, Der Kiureghian, 1996, Der Kiureghian et al., 1997, Zanardo et al., 2002, Sextos et al., 2003b, Lin et al., 2004, Soyluk, 2004, Lupoi et al., 2005, Ye et al., 2011, Camara and Astiz, 2012, Camara et al., 2014, Zerva, 2016, Liu et al., 2016). The influence of multi-input seismic excitation on long structures is complex. This has resulted in a few antithetical study outcomes that have dissimilar assumed structural models and ground motion inputs (Bogdanoff et al., 1965, Masri, 1976, Hao and Duan, 1995, Loh and Ku, 1995, Der Kiureghian et al., 1997).

In the design of artifacts such as multi-span bridges, the structural engineer would like to know whether, and when, it is necessary to model the spatial variation in ground motion (Nazmy and Abdel-Ghaffar, 1992, Zerva, 2016). There are extensive databases of accelerogram records for singleton stations. However, there exist far fewer record sets that have enough spatially distributed stations, that are close enough together, to accurately estimate the complete spatiotemporal surficial ground motion (Loh et al., 1982). Thus, the structural engineer is often left with the choice of artificially generating spatiotemporal ground motion (Harichandran and Vanmarcke, 1986, Harichandran et al., 1996) or neglecting the spatial variation by using identical ground motion inputs at all supports (Fardis, 2005).

Over the last two decades, the approach using random vibration techniques, in the frequency domain, for example (Abdel-Ghaffar and Rubin, 1982), has frequently been employed as the uncertainty of seismic inputs can be easily modeled and interpreted by structural engineers (Abdel-Ghaffar and Rubin, 1982, Ding et al., 2007). These techniques are generally limited to a linear elastic problem domain. Time-domain analyses (Fajfar, 2000, Lou and Zerva, 2005, Bardakis and Fardis, 2011, Konakli and Der Kiureghian, 2014), that account for spatial ground motions, can be considered in two forms (i) a modal decomposition that makes use of spectral responses and modal combination rules and (ii) a full nonlinear time-history analysis that uses spatiotemporal ground motion time-series. Methodology (i) is an approximate method for the case of nonlinear systems as modal decomposition/superposition is no longer a mathematically valid concept in this case. Nevertheless, some researchers have still proposed extending spectrum-oriented methods into the nonlinear regime by using a statistical linearization technique (Guyader and Iwan, 2006b, Spanos and Giaralis, 2013, Mitseas et al., 2018).

The methods for dynamic analysis can be deterministic or statistical (Kazakov, 1966b). In practical design, a probabilistic approach developed by structural engineers generally involves defining both ground excitation and seismic response through stochastic (frequency domain) procedures such as power spectra, transfer function estimates, and coherency (Iwan, 1980, Lai, 1982, Roberts and Spanos, 2003, Konakli, 2011, Monteiro et al., 2014, Mitseas et al., 2018). The proposed analysis schemes are based on statistical linearization in order to decompose an inelastic multi-degree-of-freedom system (MDOF) into a limited set of an equivalent linear single-degree-of-freedom system (SDOF) with effective linear characteristics (Kazakov, 1966a, Atalik and Utku, 1976, Guyader and Iwan, 2006a, Spanos and Giaralis, 2013, Kougioumtzoglou and Spanos, 2013).

A large number of studies assume that the structural model behaves linearly to make use of the principle of superposition (Price and Eberhard, 1998, Soyluk, 2004, Zhao et al., 2015). However, for a design level seismic event, it is often the case that the design philosophy will make use of the energy dissipation of ductile piers (Gulkan and Sozen, 1974, Kowalsky, 2002, BSI, 2005, Dwairi and Kowalsky, 2006, Paraskeva et al., 2006, Bi et al., 2011). Hence, a system-level reduced-order model needs to accommodate the nonlinear inelastic behavior of the piers. It must provide the necessary hysteretic mechanism to dissipate the considerable amounts of earthquake energy under an extreme seismic event (Kappos, 2010). This is why seismic code provisions favor the utilization of nonlinear methodologies for bridge assessment with the aim of identifying the configuration of plastic hinges in piers, estimate post-yield deformation capacity of ductile members and determine the required strength for the avoidance of failure in the demand-protected elements (Yashinsky and Ostrom, 2000, Kawashima and Unjoh, 2004, BSI, 2005). Various analytical procedures ranging from elastic (equivalent static or dynamic)

to nonelastic (pushover or dynamic time-history) analysis have been proposed to estimate the post-elastic response of a structure. Among all proposed methods, nonlinear dynamic (time-history) analysis has been recognized as the most simplified method, although considerable time and knowledge are required to employ it effectively. The leading code provision such as Eurocode 8 (BSI, 2005) and CALTRANS (Yashinsky and Ostrom, 2000) and the analytical tools developed by different researchers (Sextos et al., 2003b, Lou and Zerva, 2005) aim to employ idealized bilinear models for the stress-strain relationship of ductile members.

Real earthquakes produce spatially heterogeneous, surficial, ground motions. Wavelengths of shear waves at the surface (in granite) are typically between 0.3km and 3km (for 10Hz and 1Hz component frequencies respectively (Bolt 2001)). Thus, long structures can suffer from differential excitations along their length. Nuti and Vanzi [81] discussed many important parameters showing for example spatial incoherence is very influential even for medium-span bridges. This spatial variation in ground motion can be more pronounced over even shorter distances in the case where the superficial geology exhibits heterogeneity, (Lavorato et al., 2017, Lavorato et al., 2018).

Amongst all parameters in the modeling of a dynamic system, ground motion input exhibits the highest level of uncertainty. A variety of methodologies and analytical tools are currently available to address these uncertainties. The spatial incoherence of the ground motion is modeled by empirical formulae (calibrated through regression analyses) (Harichandran and Vanmarcke, 1986, Hao et al., 1989, Loh and Lin, 1990, Abrahamson et al., 1991, Oliveira et al., 1991), semi-empirical approach (Luco and Wong, 1986, Der Kiureghian, 1996, Zerva and Harada, 1997), and fully theoretical models (Zerva and Shinozuka, 1991, Liao and Li, 2002).

The influence of spatial heterogeneity in the ground excitation input is primarily categorized by (Der Kiureghian, 1996): (a) the wave-passage effect due to the time lag of the arriving wave between two arbitrary stations i and j; (b) the loss of coherency due to consecutive reflections and refractions of earthquake waves as they scatter in heterogeneous soil media (c) the local site effects due to variation in local soil conditions underneath each station which propagate seismic waves with different frequency and amplitude content.

The artificial spatiotemporal models of ground motions, such as (Harichandran and Vanmarcke, 1986), define the variation in ground motion expected between any arbitrary stations. These models tend to assume some exponential approximation for the absolute coherency and a linear function for the phase variation between stations. Using ground motion models whose spatial variability are parametrically stochastic is attractive as they enable the use and extension of recorded singleton station records to the generalized spatiotemporal case. This allows pseudo-sensitivity analyses to be performed with respect to these stochastic model parameters. However, and unfortunately, it is well-known that these models fail to capture exactly the complicated and random variations present in real spatially heterogeneous ground motions; e.g. (Alexander, 2008, Lavorato et al., 2018). These parametric models assume a particular spatial coherence which may not be valid in the general case of heterogeneous ground in anything other than an approximate sense. An alternative is to make use of real spatiotemporal ground motions, from multi-station arrays. These significantly reduce the uncertainty of spatial ground motion variation at a particular site but are unfortunately limited to only a few particular locations where these arrays exist. Therefore, we are faced with a choice between imposing uncertain variation caused by *a priori* assumptions implied by parametric stochastic ground motion models or the

uncertainty of a small sample of real spatio-temporal ground motions at a limited number of locations. In this study, we chose to adopt the latter rather than the former, i.e. we make use of real recorded data over multi-station arrays to generate spatiotemporal characteristics of the motions rather than assume *a priori* a parametric coherency model.

In addition to the above advancements, the real seismic ground motion records from digital accelerometer arrays located all over the world like the SMART-1 array in Taiwan (Abrahamson et al., 1987) and Imperial Valley in California (Joyner and Boore, 1981) provide very important sources of information for exploring spatially heterogeneous ground motions.

Varied studies concluded different seismic response patterns for spatially support excitations (Zanardo et al., 2002). Shinozuka and Deodatis (1991) developed a rigorous derivation of the computationally efficient cosine series formula for the generation of sample functions of one-dimensional and univariate nonstationary stochastic processes. In the design of nuclear structures, American Society of Civil (1987) recommended specific seismic reduction factors that account for the effect of spatially varying ground motion. For suspension and cable-stayed bridges, Nazmy and Abdel-Ghaffar (1992) propose the use of simulated ground excitations for analyses of multi-support excitation problems. However, in the design of highway bridges, an equivalent uniform excitation, that simulates the effect of spatially variable ground motion, is suggested in (Fardis, 2005).

Owing to the simplicity of its structural configuration, the majority of investigations are on the effect of spatially varying ground motion on highway bridges (Johnson and Galletly, 1972, Kiureghian and Neuenhofer, 1992, Zerva, 2016). One of the early studies to evaluate the seismic response of highway bridges under a range of multi-support excitations was Monti et al. (1996). They concluded that, in general, using identical support

excitation (ISE), rather than multi-support excitation (MSE), led to a conservative design. However, Tzanetos et al. (2000) drew different conclusions. They questioned the scope and generality of the conclusions (Monti et al., 1996) by pointing out the symmetric bridge configuration and characteristics of the ground motions employed in the study.

Zerva (1991, 1990) carried out comprehensive analyses of two-span and three-span continuous beams, of varying span lengths, under different arrangements of spatially varying ground motions. She concluded that, for symmetrical structural configurations, ISE could only excite the symmetric modes, while MSE could excite all modes, i.e. symmetrical and anti-symmetrical modes. Furthermore, asynchronous excitation increases the modal response for higher modes more remarkably than synchronous excitation. Price and Eberhard (1998) conducted a comprehensive analysis on a two-span bridge under incoherent excitation. In their study, for spatially varying excitation, a significant increase of anti-symmetrical modal responses was observed although the contribution of symmetrical modes tended to decrease.

The structural configuration (symmetry, overall length, regularity, abutment condition, etc.) coupling with ground motion characteristics determines the dynamic response pattern. A parametric study of 27 different bridges conducted by Sextos et al. (2003a, 2003b) reveals that the limit, of an overall length of the bridge, for consideration of spatial variability in the dynamic analysis is in the range of 200-400m for different ground categories which are reconcilable with EC8 classification. Lou and Zerva (2005) highlighted the significant effects of spatial variability for a shorter bridge with supports in which soil conditions at their bases differ considerably. Recent studies primarily examined the response of symmetrical and unsymmetrical structures (Hahn and Liu, 1994, Hao, 1991, Zerva, 1990); investigated the spatial variability effect on suspension and cable

bridges (Nazmy and Abdel-Ghaffar, 1992, Camara and Astiz, 2012); evaluated the effect of the anti-symmetrical mode on the bridge responses (Price and Eberhard, 1998, Lee et al., 2006, Papadopoulos and Sextos, 2018); exploring the effect of valley profile on the accuracy of ISE analyses for linear and nonlinear cases (Meibodi and Alexander, 2020, Meibodi et al., 2020) and developed the nonlinear dynamic analysis to incorporate the effect of spatial variability (Wen, 1976, Guyader and Iwan, 2006a, Sextos and Kappos, 2009, Mitseas et al., 2018).

1.2 OBJECTIVE AND SCOPE

In this context, the objective of this thesis is first to understand and explore the mathematical features of a generalized reduced-order model to calculate the dynamic response of a multi-support bridge when spatial variability of the ground motion is taken into account. This proposed linear model is then transformed into a frequency-domain with the specific aim of quantifying the plausible bounds on the error between multi-support excitation (MSE), and identical support excitation (ISE) analysis. These bounds are expressed in terms of the (a) Auto Modal Participation (AMP) and (b) Cross-Modal participation (CMP) factors. They are only dependent on bridge geometry and hence can be evaluated before any dynamic analysis. This novel reduced order model is then applied to the nonlinear system which is capable of incorporating the hysteretic and inelastic behavior of bridge piers.

Conventional nonlinear finite element analyses use tens of thousands of degrees of freedom for a large bridge in 3D and must have a prescribed explicit geometry. Thus, any parametric exploration using large numbers of ground motions places a huge computational burden on any analysis. This makes such systematic and extensive

parametric explorations of geometric effects, such as valley profile, etc. very difficult to undertake in practice. As an alternative, we seek to develop a reduced-order nonlinear model that enables parametric explorations to be undertaken in a more timely fashion, and thus allows far more parametric cases to be considered.

For ground excitation, we do not use artificial records but employ real spatiotemporal ground motions recorded at the SMART-1 array, Taiwan. We make use of standard correction procedures, amplitude scaling, and spatial interpolation.

For the purpose of validation, we use results from a physical scale model benchmark test. This physical scale model of a bridge with five independently actuated supports were designed and tested previously (Norman and Crewe, 2008, Norman et al., 2006, Norman, 2006). These tests were carried out at the University of Bristol. We make use of the reduced-order multi-input multi-output (MIMO) formulation to perform a novel inverse system identification of the physical benchmark tests. Afterward, this benchmarked linear generalized bridge model is extended to the case of bridges with ductile piers.

To confirm the utility of these *geometry only* bounds an extensive parametric analysis scheme (that made use of tens of thousands of time-history analyses) is undertaken where the geometrical configuration of a heuristic bridge is altered due to valley profile. Therefore, this thesis aims:

i. to assess the relative importance of proposed geometrical parameters, the Auto Modal Participation factor (AMP) and Cross-Modal Participation factor (CMP), and investigate its correlation with bridge responses from large-scale parametric studies conducted in the companion study.
ii. to evaluate, quantitively, the role that symmetric and anti-symmetric modes play in the bridge responses for these critical configurations.

iii. What is the effect of valley profile on the accuracy of ISE analyses? For this objective, we parametrically vary pier-to-deck stiffness ratio and inter-pier stiffness ratio parameters.

iv. to determine the effect of bridge alignment (i.e. the compass bearing of the longitudinal bridge axis) on the accuracy of ISE analyses? For this objective, we explore 12 different horizontal bridge alignments.

v. to explore whether certain *geometry only* bounds (proposed in this study) can help to identify critical bridge configurations where identical support excitation (ISE) and multi-support excitation (MSE) analyses produce significantly different answers.

vi. to determine whether ground motion amplitude affects the accuracy of ISE analyses? For this objective, we explore low (elastic responses of bridge piers), medium (moderate ductility responses of bridge piers), and high (large ductility responses of bridge piers) cases.

1.3 ORGANIZATION OF THE THESIS

This thesis is organized into 8 chapters. Chapter 2 discusses the derivation and implementation of a novel linear reduced-order model. In Chapter 3, This is extended into a nonlinear regime by incorporating pier hysteretic damage which includes both stiffness and strength degradation in discusses the processing of the real seismic ground motion records from the SMART-1 array (Taiwan). These spatiotemporal seismic wavefields are used to determine discrete seismic ground motion inputs for the analysis of bridge responses in Chapter 4. Chapter 5 describes the State-space model of the proposed dynamic system that is used for calibration/validation. This is performed using a grey-box inverse

system identification method. Chapter 6 and 7 explore an extensive parametric analysis scheme to quantify the response differences between multi-support excitation (MSE) and identical support excitation (ISE) analyses. More details and specifications of subjects covered in each chapter are described as follows:

In Chapter 2, a generalized reduced-order model of a multi-span continuous bridge, on flexible discrete supports, that is subjected to multi-support seismic excitation is presented. This model highlights the key non-dimensional system parameters. From the mathematical expression of the dynamic equation of motion, plausible bounds on the error between MSE and ISE analysis are derived in terms of the (a) Auto Modal Participation (AMP) and (b) Cross-Modal participation (CMP) factors. Both terms are structure-specific and independent of the ground motions themselves.

In Chapter 3, the pier hysteresis is incorporated into the proposed linear system. it enables the inelastic time-history dynamic analysis of MDOF bridge under multi-support seismic excitation. The RC piers' hysteretic relationship is facilitated by the Bouc-Wen model where strength deterioration and stiffness degradation are considered.

Chapter 4 explains real spatiotemporal ground motions recorded at the SMART-1 array, Taiwan. The modification and correction process of seismic data are discussed. We make use of standard correction procedures, amplitude scaling, and spatial interpolation. These rotated seismic ground motion records are employed for seismic input of the studied bridge as an alternative to artificial ground motion based on some spatial incoherence kernels. A stochastic descriptor of seismic data including Power Spectrum and co-spectrum for oriented seismic inputs are interpreted and key features of the seismic input data are highlighted.

In Chapter 5, the proposed equations of motion are re-cast into a multi-input-multi-

output (MIMO) system formulation. It allows us to establish a system identification model for the dynamic system using grey-box methods. For the purpose of validation, we use results from physical scale model benchmark tests. This physical scale model of a bridge with five independently actuated supports was designed and tested previously (Norman et al., 2006, Norman, 2006, Norman and Crewe, 2008). These tests were carried out at the University of Bristol. We make use of the reduced-order MIMO formulation to perform inverse system identification of the physical benchmark tests. Then, the results of this inverse system identification are used to calibrate/validate the proposed mathematical model of a nonlinear dynamic system from Chapter 3.

In Chapter 6, systematic and extensive parametric explorations of geometric effects, such as valley profile are undertaken in a more comprehensive fashion. This allows far more parametric cases to be considered. The potential importance of the proposed geometry parameters defined in Chapter 2 is demonstrated in view of numerical results involving parametric analysis of the studied bridges excited by real ground input motion from SMART-1 array.

In Chapter 7, first, nonlinear time history analyses are performed on the generalized 4-span bridge structure with 3 Bouc-Wen hysteretic RC piers to illustrate the applicability of the adopted approach. Then, an extensive parametric analysis scheme similar to the previous chapter is conducted to identify whether the ductile behavior of dissipating members (RC piers) leads to any significant deviations from the linear analysis result where spatially ground motion is taken to account.

Finally, Chapter 8 draws conclusions from this study and remarks on some recommendations for future studies.

Chapter 2

A Linear Reduced Order Model for transversal Responses of Bridge

The contents of this chapter have been partially adapted from the study (Meibodi et al., 2020, Meibodi and Alexander, 2021) that published in:

MEIBODI, A. A. & ALEXANDER, N. A. 2021. Spatiotemporal seismic excitation of bridges with an anti-symmetrical first mode. *Bulletin of Earthquake Engineering*.

MEIBODI, A. A., ALEXANDER, N. A., NORMAN, J. A. & CREWE, A. J. 2020. A theoretical and experimental exploration of the seismic dynamics of multi-span bridges. *Bulletin of Earthquake Engineering*.

2.1 INTRODUCTION

The typical method of setting up the equations of motion for the multi-support excitation of multi-span bridges involves the finite element method as described in (Chopra, 2007, Zerva, 2016). However, in this study, we are seeking a novel reduced order model (i) that is highly computationally efficient so that large-scale future parametric studies can be performed, and it additionally can enable future real-time sub-structuring tests of nonlinear columns (Wagg and Neild, 2010) (ii) that helps to identify the key system parameter groups for this problem and (iii) that is readily extendable to include nonlinear hysteretic phenomenological of soil and columns (Bouc, 1967, Wen, 1976).

The random vibration approach follows directly from the evaluation of the deterministic dynamic response of structures, only in this case, the excitation is described by a random process (or field) rather than a time series. This section illustrates the basic steps that lead from the derivation of the deterministic response of a dynamic system to the evaluation of its mean value and PSD caused by a random excitation.

2.2 FORMULATION OF MULTI-SUPPORTED SYSTEM

2.2.1 Defining Kinetic and Potential energies

Consider a general multi-span bridge subjected to transversal ground excitation shown in Figure 1. This reduced-order model can be likened to the dynamics of a beam on a discrete elastic foundation that is subjected to spatiotemporal support excitation. The total number of deck DOFs is *m* but the two abutments are constraints hence there are *n* free DOFs (unknowns) of the deck which is $n = m - 2$. The system degree of freedom consists of two parts: (i) the *n* deck DOFs (unknowns) and (ii) the *s* ground DOFs (knowns) which

is equal to the number of supports.

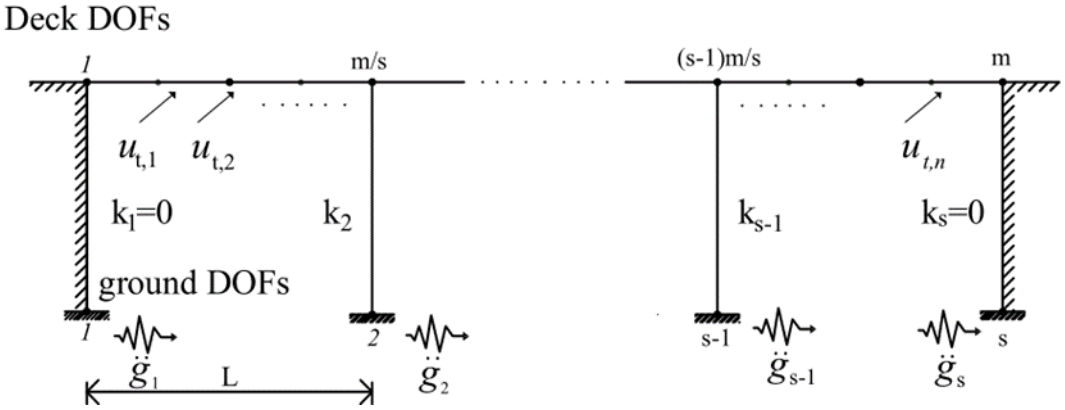

Figure 1; General MDOFs Bridge with *n* unconstrained DOFs (where $n = m - 2$) of deck resting on s supports.

Where $\mathbf{u}_t = [u_{t,1}, \cdots, u_{t,n}]^T \in \mathbb{R}^{n\times 1}$ and $\mathbf{u}_g = [g_1, \cdots, g_s]^T \in \mathbb{R}^{s\times 1}$. The kinetic energy for the deck is as follows:

$$T = \tfrac{1}{2}\int_0^{(s-1)L} m_d \dot{y}_d^2 \mathrm{d}x \tag{2.1}$$

Where m_d mass per unit length and y_d is the deck transversal displacement in the horizontal *xy* plane. Pier masses are neglected in this analysis. Note the Newtonian prime notation indicates differentiation with respect to a spatial variable, hence $y' = \mathrm{d}y/\mathrm{d}x$, while the dot notation indicates differentiation with respect to a temporal variable, hence $\dot{y} = \mathrm{d}y/\mathrm{d}t$. The Potential Energy is given as follows:

$$U = \tfrac{1}{2}\int_0^{(s-1)L} EI_z y_d''^2 \mathrm{d}x + \tfrac{1}{2}\sum_{i=1}^{s} k_i \left(y_d(x_i) - y_g(x_i)\right)^2 - \sum_{i=1}^{s} R_i y_g(x_i) \tag{2.2}$$

where EI_z is the deck flexural rigidity, R_i is the ground reaction underneath the pier, x_i and k_i are the i^{th} pier locations and its transversal flexural stiffness and y_g is the seismically induced free field displacement of the ground surface. The first term in Eq (2.2)

is the flexural strain energy of the deck, the second term is the flexural strain energy of the pier/soil springs, and the final term is the work done by the horizontal ground reactions. The connection between piers and deck is assumed to be moment-less i.e. pinned.

As there are no piers that exist at abutments, no flexural piers energy of these supports would participate in the system energy. Therefore, we assign the value of zero to the first and last pier stiffness ($k_0 = k_s = 0$) to remove the terms of the corresponding abutment from the flexural strain energy of the pier/soil springs.

2.2.2 Employing Discrete Spatiotemporal Rayleigh-Ritz Vectors

By introducing a Rayleigh-Ritz type spatiotemporal function for integral Eq (2.1) and Eq (2.2) we can convert these continuous equations into discrete ones. The seismically induced displacement of ground y_g and deck y_d are defined throughout Rayleigh-Ritz type spatiotemporal function as follows:

$$y_d(x,t) = \mathbf{u}_d(t)^T \boldsymbol{\psi}(x), \qquad y_g(x,t) = \mathbf{u}_g(t)^T \boldsymbol{\psi}_g(x) \tag{2.3}$$

$$\mathbf{u}_d = \left[u_{d,1}, \cdots, u_{d,m}\right]^T \in \mathbb{R}^{m\times 1}, \quad \mathbf{u}_g = \left[g_1, \cdots, g_s\right]^T \in \mathbb{R}^{s\times 1} \tag{2.4}$$

$$\boldsymbol{\psi} = \begin{bmatrix}\psi_1 & \psi_2 & \cdots & \psi_m\end{bmatrix}^{\mathrm{T}} \in \mathbb{R}^{m\times 1}, \quad \boldsymbol{\psi}_g = \begin{bmatrix}\psi_1 & \psi_2 & \cdots & \psi_s\end{bmatrix}^{\mathrm{T}} \in \mathbb{R}^{s\times 1} \tag{2.5}$$

Where $\mathbf{u}_d$ are the degrees of freedom (unknowns) on the deck and $\mathbf{u}_g$ are the constrained degrees of freedom (knowns) connected to the ground ($m \geq s$). Lagrangian interpolants are employed, for these Ritz vectors, because they have certain orthogonal properties that diagonalize all subsequent pier/soil stiffness block matrices. This useful feature makes it simpler to deal with the end constraints of the deck through later

partitioning and condensation. These are employed to define the Ritz vectors basis of deck $\boldsymbol{\psi}$ and ground $\boldsymbol{\psi}_g$ respectively. A general Lagrangian interpolating polynomial is given as:

$$\psi_i(x) = \frac{\ell_i(x)}{\ell_i(x_i)}, \quad \ell_i(x) = \frac{\prod_{q=1}^{m}(x - x_q)}{(x - x_i)} \tag{2.6}$$

Hence, we can write the Lagrangian (Kinetic minus Potential Energies) as follows:

$$\begin{aligned}\Pi = \tfrac{1}{2}\dot{\mathbf{u}}^T\left[\int_0^{(s-1)L} m_d\boldsymbol{\psi}\boldsymbol{\psi}^T \mathrm{d}x\right]\dot{\mathbf{u}} - \tfrac{1}{2}\mathbf{u}^T\left[\int_0^{(s-1)L} EI_z\boldsymbol{\psi}''\boldsymbol{\psi}''^T \mathrm{d}x\right]\mathbf{u} - \tfrac{1}{2}\mathbf{u}^T\left[\sum_{i=1}^{s} k_i\boldsymbol{\psi}(x_i)\boldsymbol{\psi}(x_i)^T\right]\mathbf{u} \\ + \mathbf{u}^T\left[\sum_{i=1}^{s} k_i\boldsymbol{\psi}(x_i)\boldsymbol{\psi}_g^T(x_i)\right]\mathbf{g} - \tfrac{1}{2}\mathbf{g}^T\left[\sum_{i=1}^{s} k_i\boldsymbol{\psi}_g(x_i)\boldsymbol{\psi}_g^T(x_i)\right]\mathbf{g} + \mathbf{g}^T\sum_{i=1}^{s} R_i\boldsymbol{\psi}_g(x_i)\end{aligned} \tag{2.7}$$

where the first term in the above equations is from the Kinetic energy and all subsequent terms are from the Potential energy. Note that all stiffness and inertia terms are in a quadratic form.

2.2.3 Dimensionless Lagrangian.

By introducing a dimensionless coordinate and assuming constant deck mass per unit length and flexural rigidity, the Lagrangian can be re-written as follows:

$$\begin{aligned}\Pi = \tfrac{1}{2}m_d L\dot{\mathbf{u}}^T\left[\int_0^{s-1}\boldsymbol{\psi}\boldsymbol{\psi}^T \mathrm{d}\xi\right]\dot{\mathbf{u}} - \tfrac{1}{2}\frac{EI_z}{L^3}\mathbf{u}^T\left[\int_0^{s-1}\boldsymbol{\psi}''\boldsymbol{\psi}''^T \mathrm{d}\xi\right]\mathbf{u} - \tfrac{1}{2}\mathbf{u}^T\left[\sum_{i=1}^{s} k_i\boldsymbol{\psi}(\xi_i)\boldsymbol{\psi}(\xi_i)^T\right]\mathbf{u} \\ + \mathbf{u}^T\left[\sum_{i=1}^{s} k_i\boldsymbol{\psi}(\xi_i)\boldsymbol{\psi}_g^T(\xi_i)\right]\mathbf{g} - \tfrac{1}{2}\mathbf{g}^T\left[\sum_{i=1}^{s} k_i\boldsymbol{\psi}_g(\xi_i)\boldsymbol{\psi}_g^T(\xi_i)\right]\mathbf{g} + \mathbf{g}^T\sum_{i=1}^{s} R_i\boldsymbol{\psi}_g(\xi_i)\end{aligned} \tag{2.8}$$

In the above Eq(2.8), we re-define the prime to be differentiation with respect to ξ hence, $y'' = \mathrm{d}^2y/\mathrm{d}\xi^2$ and therefore $\mathrm{d}^2y/\mathrm{d}x^2 = \left(1/L^2\right)y''$. By dividing Eq (2.8) by m_dL we obtain:

$$\frac{\Pi}{m_d L} = \tfrac{1}{2}\dot{\mathbf{u}}^T \mathbf{M}_d \dot{\mathbf{u}} - \tfrac{1}{2}\left(\mathbf{u}^T \mathbf{K}_d \mathbf{u} + \mathbf{u}^T \mathbf{K}_g \mathbf{u} - 2\mathbf{u}^T \mathbf{K}_g \mathbf{g} + \mathbf{g}^T \mathbf{K}_{gg} \mathbf{g} - 2\mathbf{g}^T \mathbf{r}\right) \tag{2.9}$$

Where matrices are defined as follows:

$$\mathbf{M}_d = \int_0^{s-1} \boldsymbol{\psi}\boldsymbol{\psi}^T \mathrm{d}\xi \in \mathbb{R}^{m\times m}, \quad \mathbf{K}_d = \varpi^2 \int_0^{s-1} \boldsymbol{\psi}''\boldsymbol{\psi}''^T \mathrm{d}\xi \in \mathbb{R}^{m\times m} \tag{2.10}$$

$$\begin{gathered} \mathbf{K}_g = \varpi^2 \sum_{i=1}^{n} \eta_i \boldsymbol{\psi}(\xi_i)\boldsymbol{\psi}_g^T(\xi_i) \in \mathbb{R}^{m\times s}, \ \mathbf{K}_{gg} = \varpi^2 \sum_{i=1}^{n} \eta_i \boldsymbol{\psi}_g(\xi_i)\boldsymbol{\psi}_g^T(\xi_i) \in \mathbb{R}^{s\times s}, \\ \mathbf{K}_s = \varpi^2 \sum_{i=1}^{n} \eta_i \boldsymbol{\psi}(\xi_i)\boldsymbol{\psi}^T(\xi_i) \in \mathbb{R}^{m\times m}, \ \mathbf{r} = \sum_{i=1}^{s} r_i \boldsymbol{\psi}_g(\xi_i) \in \mathbb{R}^{s\times 1} \end{gathered} \tag{2.11}$$

The system dynamic parameters are defined as follows:

$$\varpi^2 = \frac{EI_z}{m_d L^4}, \qquad \eta_i = \frac{k_i L^3}{EI_z}, \qquad r_i = \frac{R_i L^2}{EI_z} \tag{2.12}$$

2.2.4 Euler-Lagrange Equations of Motion

The Euler-Lagrange equations are as follows:

$$\frac{\mathrm{d}}{\mathrm{d}t}\left(\frac{\partial \Pi}{\partial \dot{\mathbf{u}}}\right) - \left(\frac{\partial \Pi}{\partial \mathbf{u}}\right) = 0 = \tfrac{1}{2}\mathbf{M}_d \ddot{\mathbf{u}} - \left(\mathbf{K}_d \mathbf{u} + \mathbf{K}_g \mathbf{u} - \mathbf{K}_g \mathbf{g}\right) \tag{2.13}$$

$$\frac{\mathrm{d}}{\mathrm{d}t}\left(\frac{\partial \Pi}{\partial \dot{\mathbf{g}}}\right) - \left(\frac{\partial \Pi}{\partial \mathbf{g}}\right) = 0 = \left(-\mathbf{K}_g{}^T \mathbf{u} + \mathbf{K}_{gg}\mathbf{g} - \mathbf{r}\right) \tag{2.14}$$

Hence, the full dimensionless equations of motion (Clough and Penzien, 1995) are as follows:

$$\begin{bmatrix} \mathbf{M}_d & \mathbf{0} \\ \mathbf{0} & \mathbf{0} \end{bmatrix} \begin{bmatrix} \ddot{\mathbf{u}}_d \\ \ddot{\mathbf{u}}_g \end{bmatrix} + \begin{bmatrix} \mathbf{K}_d + \mathbf{K}_g & -\mathbf{K}_g \\ -\mathbf{K}_g^T & \mathbf{K}_{gg} \end{bmatrix} \begin{bmatrix} \mathbf{u}_d \\ \mathbf{u}_g \end{bmatrix} = \begin{bmatrix} \mathbf{0} \\ \mathbf{r} \end{bmatrix} \tag{2.15}$$

2.2.5 Matrix partitioning and Condensation

At this point, we introduce a set of constraint equations for the two ends of the deck. It is assumed that the deck meets the ground at the two ends and therefore must have the same displacement, i.e. $y(0,t)=y_g(0,t)$ and $y\big((s-1)L,t\big)=y_g\big((s-1)L,t\big)$. These two boundary conditions can be dealt with by either (i) assuming very stiff piers at the two ends, or (ii) introducing Lagrange multipliers constraint equations, or (iii) by matrix partitioning and condensation. We chose the latter approach here as it appears to be the most numerically stable and efficient approach. To achieve this matrix partitioning we re-order the dofs thus:

$$\mathbf{u}_d=\begin{bmatrix} u_{d,2} \\ \vdots \\ u_{d,m-1} \\ \hline u_{d,1}=g_1 \\ u_{d,m}=g_s \end{bmatrix}=\begin{bmatrix}\mathbf{u}_t \\ \mathbf{g}_E\end{bmatrix},\quad \mathbf{u}_g=\begin{bmatrix} g_1 \\ g_s \\ \hline g_2 \\ \vdots \\ g_{s-1}\end{bmatrix}=\begin{bmatrix}\mathbf{g}_E \\ \mathbf{g}_I\end{bmatrix} \tag{2.16}$$

As two abutments provide an additional two constraints, the total number of free degrees of freedom is now $n=m-2$. Hence, the DOFs $\mathbf{u}_t\in\mathbb{R}^{n\times 1}$ (unknowns).

The block matrix of two ends of the deck u_1, u_m should be merged into the block matrix of ground DOFs g_1, g_s. We partition mass and stiffness block matrix of Eq (2.15) respectively as follows:

$$\left[\begin{array}{c|c|c} \mathbf{M}_{d11} & \mathbf{M}_{d12} & \mathbf{0} \\ \hline \mathbf{M}_{d12}^T & \mathbf{M}_{d12} & \\ \hline \mathbf{0} & & \mathbf{0} \end{array}\right]\left[\begin{array}{c}\ddot{\mathbf{u}}_t \\ \hline \ddot{\mathbf{g}}_E \\ \ddot{\mathbf{g}}_E \\ \ddot{\mathbf{g}}_I\end{array}\right]+\left[\begin{array}{cc|cc} \mathbf{K}_{d11}+\mathbf{K}_{s11} & \mathbf{K}_{d12} & \mathbf{0} & \mathbf{0} \\ \mathbf{K}_{d12}^T & \mathbf{K}_{d22} & \mathbf{0} & -\mathbf{K}_{g22} \\ \hline \mathbf{0} & \mathbf{0} & \mathbf{0} & \mathbf{0} \\ \mathbf{0} & -\mathbf{K}_{g22}^T & \mathbf{0} & \mathbf{K}_{gg22} \end{array}\right]\left[\begin{array}{c}\mathbf{u}_t \\ \hline \mathbf{g}_E \\ \mathbf{g}_E \\ \mathbf{g}_I\end{array}\right]=\begin{bmatrix}\mathbf{0} \\ \mathbf{r}\end{bmatrix} \tag{2.17}$$

The above Eq (2.17) can be condensed as follows:

$$\left[\begin{array}{c|c|c} \mathbf{M}_{d11} & \mathbf{M}_{d12} & \mathbf{0} \\ \hline \mathbf{M}_{d12}^T & \mathbf{M}_{d22} & \mathbf{0} \\ \hline \mathbf{0} & \mathbf{0} & \mathbf{0} \end{array}\right]\left[\begin{array}{c} \ddot{\mathbf{u}}_t \\ \hline \ddot{\mathbf{g}}_E \\ \hline \ddot{\mathbf{g}}_I \end{array}\right]+\left[\begin{array}{c|c|c} \mathbf{K}_{d11}+\mathbf{K}_{s11} & \mathbf{K}_{d12} & -\mathbf{K}_{g22} \\ \hline \mathbf{K}_{d12}^T & \mathbf{K}_{d22} & \mathbf{0} \\ \hline -\mathbf{K}_{g11}^T & \mathbf{0} & \mathbf{K}_{gg22} \end{array}\right]\left[\begin{array}{c} \mathbf{u}_t \\ \hline \mathbf{g}_E \\ \hline \mathbf{g}_I \end{array}\right]=\left[\begin{array}{c} \mathbf{0} \\ \hline \mathbf{r} \end{array}\right] \quad (2.18)$$

The final form of the equation, in general, would take a form as follows:

$$\left[\begin{array}{cc} \mathbf{M}_{11} & \mathbf{M}_{12} \\ \mathbf{M}_{12}^T & \mathbf{M}_{22} \end{array}\right]\left[\begin{array}{c} \ddot{\mathbf{u}}_t \\ \ddot{\mathbf{u}}_g \end{array}\right]+\left[\begin{array}{cc} \mathbf{C}_{11} & \mathbf{C}_{12} \\ \mathbf{C}_{12}^T & \mathbf{C}_{22} \end{array}\right]\left[\begin{array}{c} \dot{\mathbf{u}}_t \\ \dot{\mathbf{u}}_g \end{array}\right]+\left[\begin{array}{cc} \mathbf{K}_{11} & \mathbf{K}_{12} \\ \mathbf{K}_{12}^T & \mathbf{K}_{22} \end{array}\right]\left[\begin{array}{c} \mathbf{u}_t \\ \mathbf{u}_g \end{array}\right]=\left[\begin{array}{c} \mathbf{0} \\ \mathbf{r} \end{array}\right] \quad (2.19)$$

where the stiffness matrix takes the form as:

$$\left[\begin{array}{c|c} \mathbf{K}_{11} & \mathbf{K}_{12} \\ \hline \mathbf{K}_{12}^T & \mathbf{K}_{22} \end{array}\right]=\left[\begin{array}{c|cc} \mathbf{K}_{d11} & \mathbf{K}_{d12} & -\mathbf{K}_{g22} \\ \hline \mathbf{K}_{d12}^T & \mathbf{K}_{d22} & \mathbf{0} \\ -\mathbf{K}_{g11}^T & \mathbf{0} & \mathbf{K}_{gg22} \end{array}\right] \quad (2.20)$$

And the mass matrix is defined as follows:

$$\left[\begin{array}{c|c} \mathbf{M}_{11} & \mathbf{M}_{12} \\ \hline \mathbf{M}_{12}^T & \mathbf{M}_{22} \end{array}\right]=\left[\begin{array}{c|cc} M_{d11} & M_{d12} & \mathbf{0} \\ \hline M_{d12}^T & M_{d22} & \mathbf{0} \\ \mathbf{0} & \mathbf{0} & \mathbf{0} \end{array}\right] \quad (2.21)$$

The viscous damping matrix is calculated in the standard way using modal damping (Clough and Penzien, 1995, Chopra, 2007) and is defined as follows:

$$\mathbf{C}_{11}=\left(\mathbf{\Phi}^T\right)^{-1}\mathbf{C}_i\,\mathbf{\Phi}^{-1} \quad (2.22)$$

Where dynamic system eigenvector $\mathbf{\Phi}$ is derived from eigenvalues problem $\left(\mathbf{M}_{11}^{-1}\mathbf{K}_{11}-\lambda\mathbf{I}\right)\mathbf{\Phi}=\mathbf{0}$ and $\mathbf{C}_i \in R^{n\times n}$ is a diagonal matrix containing i^{th} diagonal array equal

to $2\gamma_i\omega_i$. It must be noted, that other damping terms will be neglected in this study, therefore the calculation of these matrices is not mentioned here. Note that because we have employed Lagrangian interpolants, the matrices $\mathbf{K}_2$ and $\mathbf{C}_{12}$ are diagonal (in block matrix form) with off-diagonal zero block matrices. Therefore, the second row of the block matrix equation above leads us to the final form of the partitioned and condensed equation of motion.

The final form of the system equation of motion can take the form as:

$$\begin{bmatrix} \mathbf{M}_{11} & \mathbf{M}_{12} \\ \mathbf{M}_{21} & \mathbf{M}_{22} \end{bmatrix} \begin{bmatrix} \ddot{\mathbf{u}}_t \\ \ddot{\mathbf{u}}_g \end{bmatrix} + \begin{bmatrix} \mathbf{C}_{11} & \mathbf{C}_{12} \\ \mathbf{C}_{21} & \mathbf{C}_{22} \end{bmatrix} \begin{bmatrix} \dot{\mathbf{u}}_t \\ \dot{\mathbf{u}}_g \end{bmatrix} + \begin{bmatrix} \mathbf{K}_{11} & \mathbf{K}_{12} \\ \mathbf{K}_{21} & \mathbf{K}_{22} \end{bmatrix} \begin{bmatrix} \mathbf{u}_t \\ \mathbf{u}_g \end{bmatrix} = \begin{bmatrix} 0 \\ \mathbf{r} \end{bmatrix} \tag{2.23}$$

Where $\mathbf{u}_t \in \mathbb{R}^{n\times 1}$ and $\mathbf{u}_g \in \mathbb{R}^{s\times 1}$. The first block row of Eq (2.23) is defined as follows:

$$\mathbf{M}_{11}\ddot{\mathbf{u}}_t + \mathbf{C}_{11}\dot{\mathbf{u}}_t + \mathbf{K}_{11}\mathbf{u}_t = -\mathbf{M}_{12}\ddot{\mathbf{u}}_g - \mathbf{C}_{12}\dot{\mathbf{u}}_g - \mathbf{K}_{12}\mathbf{u}_g \tag{2.24}$$

These Eq (2.23) and (2.24) are defined in terms of a fixed coordinate frame (i.e. so-called total displacements, velocities, and accelerations). Typically, in earthquake engineering, we seek a change of coordinates that switches to a moving coordinate frame (i.e. relative coordinates). Thus, we introduce the following:

$$\mathbf{u}_t = \mathbf{u}_s + \mathbf{u} \tag{2.25}$$

Hence, the Eq (2.24) becomes

$$\mathbf{M}_{11}\ddot{\mathbf{u}} + \mathbf{C}_{11}\dot{\mathbf{u}} + \mathbf{K}_{11}\mathbf{u} = -\mathbf{M}_{11}\ddot{\mathbf{u}}_s - \mathbf{M}_{12}\ddot{\mathbf{u}}_g - \mathbf{C}_{11}\dot{\mathbf{u}}_s - \mathbf{C}_{12}\dot{\mathbf{u}}_g - \mathbf{K}_{11}\mathbf{u}_s - \mathbf{K}_{12}\mathbf{u}_g \tag{2.26}$$

We seek to simplify the above by removing the ground displacement terms from the right hand side (rhs) of the Eq (2.26). So, if we assign

$$\mathbf{u}_s = -\mathbf{R}\mathbf{u}_g, \qquad \mathbf{R} = \mathbf{K}_{11}^{-1}\mathbf{K}_{12} \in \mathbb{R}^{n\times s} \tag{2.27}$$

Note that displacements $\mathbf{u}_s$ can be viewed as the quasi-static displacement imposed on the system by the ground displacements. These impose a quasi-static set of stiffness forces $\mathbf{f}_s$ (partially non-dimensional) on the system as:

$$\mathbf{f}_s = \mathbf{K}_{11}\mathbf{u}_s = -\mathbf{K}_{12}\mathbf{u}_g \tag{2.28}$$

Thus, we can cancel out displacement terms on the rhs of the Eq (2.26) and simplify to

$$\mathbf{M}_{11}\ddot{\mathbf{u}} + \mathbf{C}_{11}\dot{\mathbf{u}} + \mathbf{K}_{11}\mathbf{u} = \mathbf{N}_a\ddot{\mathbf{u}}_g + \mathbf{N}_v\dot{\mathbf{u}}_g \tag{2.29}$$

Where

$$\mathbf{N}_a = \left(\mathbf{M}_{11}\mathbf{R} - \mathbf{M}_{12}\right) \in \mathbb{R}^{n\times s}, \quad \mathbf{N}_v = \left(\mathbf{C}_{11}\mathbf{R} - \mathbf{C}_{12}\right) \in \mathbb{R}^{n\times s} \tag{2.30}$$

Note if the damping matrix is proportional to the stiffness matrix only, then $\mathbf{C} = \alpha\mathbf{K}$ and therefore $\mathbf{N}_v = \mathbf{0}$. In the more general case, where the damping matrix $\mathbf{C}$ is orthogonal (i.e. a Caughey damping model) we can determine the undamped homogeneous solutions to Eq(2.26) by solving the eigenvalue $\Lambda\mathbf{M}_{11}\Phi = \mathbf{K}_{11}\Phi$ Nevertheless to obtain the matrix of eigenvalues $\Lambda \in \mathbb{R}^{n\times n}$ and eigenvectors $\Phi \in \mathbb{R}^{n\times n}$. In general, the term $\mathbf{N}_v\dot{\mathbf{u}}_g$ including the quasi-static velocities is neglected due to the low values of the damping, henceforth we neglect this term.

2.2.6 Modal frequency domain analysis

Let's consider, *k* modes participate in dynamic analysis. By employing generalized

coordinates defined as:

$$\mathbf{u} = \Phi\,\mathbf{q} \tag{2.31}$$

$$\mathbf{\Phi} = \left[\boldsymbol{\phi}_1 \cdots \boldsymbol{\phi}_k\right] \in \mathbb{R}^{n\times k}, \quad \mathbf{q} = \left[q_1;\cdots;q_k\right] \in \mathbb{R}^{k\times 1}, \quad \mathbf{u} = \left[u_1;\cdots;u_n\right] \in \mathbb{R}^{n\times 1} \tag{2.32}$$

where, $\mathbf{\Phi} \in \mathbb{R}^{n\times k}$ are mode-shape matrix and each matrix column specify the mode shape for each mode. By substituting Eq(2.31) into Eq(2.29) and pre-multiplying by $\mathbf{\Phi}^T$, the dynamic equation of motion is uncoupled to:

$$\ddot{q}_i + 2\gamma_i\omega_i\dot{q}_i + \omega_i^2 q_i = \boldsymbol{\phi}_i^T \mathbf{N}_a\, \ddot{\mathbf{u}}_g \tag{2.33}$$

By taking the Fourier transform of the Eq (2.33), we convert this ordinary differential equation into an algebraic equation (in the frequency domain, where ω is the Fourier frequency) as:

$$q_i(\omega) = h_i(\omega)\mathbf{\Gamma}_i^T \ddot{\mathbf{u}}_g(\omega) \tag{2.34}$$

Where the modal participation vector is defined as follows:

$$\mathbf{\Gamma}_i^T(\omega) = \mathbf{f}_i^T \mathbf{N}_a = \left[\Gamma_{i1},\cdots,\Gamma_{is}\right] \in \mathbb{R}^{1\times s} \tag{2.35}$$

and $i = \sqrt{-1}$ the scalar modal transfer function $h_i(\omega)$ is now defined for mode *k* as:

$$h_i(\omega) = \left(\left(\omega_i^2 - \omega^2\right) + \mathbf{i}2\gamma_i\omega_i\,\omega\right)^{-1}, \quad \mathbf{i} = \sqrt{-1} \tag{2.36}$$

Now let us consider a general ground motion for the p[th] support:

$$\ddot{g}_p(\omega) = R_p(\omega)\exp\left(i\theta_p(\omega)\right) \tag{2.37}$$

Therefore, the Power Spectral Density (PSD) of modal response in Eq (2.34) can be stated in general as:

$$\left|q_i(\omega)\right|^2 = \left|h_i(\omega)\right|^2 \left|\sum_{p=1}^{s} \Gamma_{ip} R_p(\omega) e^{i\theta_p(\omega)}\right|^2 \tag{2.38}$$

Further expansion and re-arrangement of Eq(2.38) (using Appendix A) results in the generalized MSE case

$$\left|q_i(\omega)\right|^2_{MSE} = \left|h_i(\omega)\right|^2 \left\{\sum_{p=1}^{s}\left(\Gamma_{ip} R_p(\omega)\right)^2 + 2\sum_{p=1}^{s-1}\sum_{l=p+1}^{s} \Gamma_{il}\Gamma_{ip} R_p(\omega) R_l(\omega)\cos\left(\theta_l(\omega)-\theta_p(\omega)\right)\right\} \tag{2.39}$$

Consider the ISE case where $R_p e^{i\theta_p} = R_l e^{i\theta_l} = Re^{i\theta}$ for $\forall p,l$ then

$$\left|q_i(\omega)\right|^2_{ISE} = \left|h_i(\omega)\right|^2 R(\omega)^2 \left\{\sum_{p=1}^{s} \Gamma_{ip}^2 + 2\sum_{p=1}^{s-1}\sum_{l=p+1}^{s} \Gamma_{il}\Gamma_{ip}\right\} \tag{2.40}$$

2.2.7 Total Response

The dynamic response of Eq (2.31) (and using Eq (2.34)) in the nodal coordinate can be represented as a linear function of modal displacement as:

$$\mathbf{u}(\omega) = \sum_{i=1}^{k} \boldsymbol{\phi}_i h_i \boldsymbol{\Gamma}_i^T \ddot{\mathbf{u}}_{\mathbf{g}}(\omega) \tag{2.41}$$

The power spectral density (PSD) of the dynamic response vector $\mathbf{S}(\omega)$ can be evaluated as:

$$\mathbf{S}(\omega) = \mathbf{u} \circ \bar{\mathbf{u}} = \left[S_{11}(\omega), S_{22}(\omega), \cdots, S_{nn}(\omega)\right]^T \tag{2.42}$$

Where symbol $\circ$ indicates the Hadamard product (element-wise vector multiply), $\bar{\mathbf{u}}$

is the complex conjugate of $\mathbf{u}$, and S_{uu} is the power spectral density of the response of the u^{th} DOF.

2.2.8 Determining the error between MSE and ISE solutions.

It is clear from a consideration of the equation of motion that we do not know *a priori* whether ISE analysis will be conservative or unconservative. Therefore, the first question here is, for what bridge/valley configurations does the ISE assumption produce an over-conservative estimate of the bridge's transversal responses? And, secondly, what is the magnitude of this error (the difference between MSE and ISE estimates)?

The modal error (the difference between MSE and ISE estimates) is defined as follows

$$\varepsilon_{u,i}(\omega) = \phi_{u,i}^2 \left(|q_i|_{MSE}^2 - |q_i|_{ISE}^2 \right) = |h_i(\omega)|^2 R(\omega)^2 \left\{ \alpha_{u,i}(\omega) + \beta_{u,i}(\omega) \right\} \quad (2.43)$$

where $\varepsilon_{u,i}(\omega)$ is the error for the u^{th} DOF due to the i^{th} mode, and the i^{th} eigenvector $\boldsymbol{\phi}_i^T = \left[\phi_{1,i}, \cdots, \phi_{n,i} \right]$ and hence $\phi_{u,i}$ its u^{th} element. Terms, $\alpha_{u,i}(\omega)$ and $\beta_{u,i}(\omega)$ are defined as follows:

$$\alpha_{u,i}(\omega) = \phi_{u,i}^2 \sum_{p=1}^{s} \Gamma_{ip}^2 \left(\frac{R_p(\omega)^2}{R(\omega)^2} - 1 \right), \quad (2.44)$$

$$\beta_{u,i}(\omega) = 2\phi_{u,i}^2 \sum_{p=1}^{s-1} \sum_{l=p+1}^{s} \Gamma_{il} \Gamma_{ip} \left(\frac{R_p(\omega) R_l(\omega) \cos\left(\theta_l(\omega) - \theta_p(\omega) \right)}{R(\omega)^2} - 1 \right) \quad (2.45)$$

These two terms in the modal error are (i) $\alpha_{u,i}(\omega)$ (the summation of support ground motion power terms) ignores the affect of arrival timing of the peaks in the ground motion and (ii) $\beta_{u,i}(\omega)$ (the summation of cross-terms and phases) includes the effect of arrival

timing of the peaks in the ground motion. The power term, $\alpha_{u,i}(\omega)$, is dependent solely on the amplitude contents of the ground motions, although the cross term, $\beta_{u,i}(\omega)$, is dependent on the amplitude and phase-difference content of the ground motions.

2.2.9 An estimate of a geometry only bound on $\alpha_{u,i}(\omega)$ and $\beta_{u,i}(\omega)$

The terms $\alpha_{u,i}(\omega)$ and $\beta_{u,i}(\omega)$ are dependant both on bridge geometry and ground motion characteristics. We seek to obtain a proxy (and in this case abound) for these terms that are independent of ground motion characteristics and dependent on geometry alone. To achieve this we introduce the following assumption. As discussed later in section 4.4, The seismic input used in this study (SAMRT-1 array) is homogenous. It means that despite differences in the pattern of seismic indicators, the peak values of the PSD curve occur at the same frequency content. We assume that there exists a singleton station (that was used for ISE) whose peak power is greater or equal to the power of any of the stations used for MSE, that is

$$R(\omega) \geq \{R_p(\omega) \ : \ \forall p\} \tag{2.46}$$

With this assumption, considering the Eq (2.44), the last bracketed term ranges from zero (when all ground motions are equal in power) to minus one (when all ground motions other than $R(\omega)$ are zero). Similarly, consider Eq (2.45), the last bracketed term ranges from zero (when all seismic inputs are equal in power) to minus two (when the phase difference $\theta_l(\omega) - \theta_p(\omega)$ between stations is exactly π). Additionally, the term $\Gamma_{il}\Gamma_{ip}$ can be positive or negative. Hence the term in Eq (2.45) (which is double summed) must range between $-2|\Gamma_{il}\Gamma_{ip}|$ and $2|\Gamma_{il}\Gamma_{ip}|$, and hence we obtain the strict mathematical bounds

that are defined in the Eq (2.47) below.

Therefore, we obtain an estimated bound of terms $\alpha_{u,i}(\omega)$ and $\beta_{u,i}(\omega)$

$$\begin{aligned} -\mathrm{A}_{u,i} \le \alpha_{u,i}(\omega) \le 0 \\ -2\left|\mathrm{B}_{u,i}\right| \le \beta_{u,i}(\omega) \le 2\left|\mathrm{B}_{u,i}\right| \end{aligned} \tag{2.47}$$

where the positive term $\mathrm{A}_{u,i}$ is designated, in this study, as the Auto Modal Participation (AMP) factor and positive/negative term $\mathrm{B}_{u,i}$ is designated, in this study, as the Cross-Modal Participation (CMP) factor, and are defined as follows:

$$\mathrm{A}_{u,i} = \phi_{ui}^2 \sum_{p=1}^{s} \Gamma_{ip}^2, \quad \mathrm{B}_{u,i} = \phi_{ui}^2 \sum_{p=1}^{s-1} \sum_{l=p+1}^{s} \Gamma_{ip}\Gamma_{il} \tag{2.48}$$

And therefore, we estimate the bound of the modal error (between ISE and MSE), using the triangle inequality, which is given by the following

$$\left|\varepsilon_{u,i}(\omega)\right| \le \left|h_i(\omega)\right|^2 R(\omega)^2 \left\{\mathrm{A}_{u,i} + 2\left|\mathrm{B}_{u,i}\right|\right\} \tag{2.49}$$

Thus, as the magnitude of $\mathrm{A}_{u,i}$ and $\mathrm{B}_{u,i}$ reduces this suggests that the error (between ISE and MSE) will also reduce. And note that this magnitude of $\mathrm{A}_{u,i}$ and $\mathrm{B}_{u,i}$ is dependent on geometry alone.

2.2.10 Modal Cross Response

the Power Spectral Density (PSD) of modal cross response between modes *i* and *j* can be stated as:

$$q_{ij}(\omega)=\sum_{p=1}^{s}\sum_{l=1}^{s}h_i(\omega)h_j^*(\omega)\Gamma_{ip}\Gamma_{jl}R_p(\omega)R_l(\omega)\cos\left(\theta_l(\omega)-\theta_p(\omega)\right)+\cdots$$
$$+\sum_{p=1}^{s}\sum_{l=1}^{s}h_i^*(\omega)h_j(\omega)\Gamma_{ip}\Gamma_{jl}R_p(\omega)R_l(\omega)\cos\left(\theta_l(\omega)-\theta_p(\omega)\right) \quad (2.50)$$

The modal-cross terms contain two components. When $p=l$, the summations of these components in Eq(2.50) represent the contribution of seismic input at p^{th} support. If $p\neq l$, the terms of the summation reflect the effect of multi-support excitation on the modal cross response.

Similarly to the Eq(2.43), the modal cross-analysis error in total coordinates can be defined as:

$$\varepsilon_{u,ij}(\omega)=\phi_{ui}\phi_{uj}\left(h_i(\omega)h_j^*(\omega)+h_i^*(\omega)h_j(\omega)\right)R(\omega)^2\lambda_{ij}(\omega) \quad (2.51)$$

Where

$$\lambda_{ij}(\omega)=\sum_{p=1}^{s}\sum_{l=1}^{s}\Gamma_{il}\Gamma_{jp}\left(1-\frac{R_p(\omega)R_l(\omega)\cos\left(\theta_l(\omega)-\theta_p(\omega)\right)}{R(\omega)^2}\right) \quad (2.52)$$

The effect of spatially ground motion on the dynamic structural response can be evaluated by exploring the modal error of each individual mode as defined in Eq (2.43). However, this modal cross-analysis error will be employed in the future parametric study to confirm the accuracy of the result. Further discussions of the effect of the modal cross-terms on structural dynamic responses can be found in the study (Lee, 2002).

2.3 SUMMARY

In this chapter, we derive a reduced-order model for the transversal vibrations of a continuous multi-span bridge. This model is based on linear elastic system behavior and makes use of real multi-station ground motion array records. Linearity limits the scope to small magnitude seismic events, therefore, results obtained should be viewed as contingent on the scope of the assumptions employed. The reduced-order model employed highlights the key system parameters, namely pier to deck stiffness ratio, inter-pier stiffness ratio, and the system fundamental frequency parameter. It allows us to represent the proposed model in Multi-input Multi-output (MIMO) system framework for the sake of model validation later in Chapter 5.

This proposed linear model was then transformed into a frequency-domain with the specific aim of quantifying the dynamic parameters that estimate the likely influence of the spatial incoherence of the ground motion.

2.4 NOMENCLATURE

Dimensions in the following list are force [F], length [L], and time [T] with non-dimensional angles defined in Radians [Rad] and other dimensionless quantities defined by [ ].

$A_{u,i}$	Auto Modal Participation (AMP) factor of uth DOF due to ith mode []
$B_{u,i}$	Cross-Modal Participation (CMP) factor of uth DOF due to ith mode []
$\mathbf{C}_{11}, \mathbf{C}_{12}, \mathbf{C}_{22}$	Non-dimensional damping block matrices []
$\mathbf{C}_i$	the diagonal matrix containing i^{th} diagonal array equal to $2\gamma_i\omega_i$ []
EI_z	Deck flexural rigidity (about z-axis) [F][L]^2

$\boldsymbol{f}_s$	Partially Non-dimensional quasi-static set of stiffness forces [L]
$\mathbf{g}_E$	Displacement ground DOF vector at exterior/end supports [L]
g_i	Displacement *of* i^{th} ground DOF [L]
$\mathbf{g}_I$	Displacement ground DOF vector at interior pier supports [L]
$\mathrm{h}_i(\omega)$	i^{th} modal transfer function [rad]$^{-2}$[T]$^{-2}$
k_i	Pier transversal flexural stiffness [F][L]$^{-1}$
$\mathbf{K}_{11}, \mathbf{K}_{12}, \mathbf{K}_{22}$	Non-dimensional block deck stiffness matrices []
$\mathbf{K}_d$	Non-dimensional deck stiffness matrix []
$\mathbf{k}_g, \mathbf{k}_{gg}$	Non-dimensional block pier stiffness matrices []
L	Span length [L]
m	Number of deck DOF []
m_d	Deck mass per unit length [F][T]^2[L]$^{-2}$
$\mathbf{M}_{11}, \mathbf{M}_{12}, \mathbf{M}_{22}$	Non-dimensional deck block mass matrix []
$\mathbf{M}_d$	Non-dimensional deck mass matrix []
n	free DOFs (unknowns) of the deck free DOFs (unknowns) of the deck []
$\mathbf{N}_a$	Non-dimensional influence matrix []
$\boldsymbol{q}$	Eigenvalues vector [L]
q_i	Eigenvalues of i^{th} mode [L]
$\mathrm{q}_{ij}(\omega)$	Power Spectral Density (PSD) of modal cross response between mode i and j can be stated [L]^2
$\boldsymbol{r}$	Partially non-dimensional horizontal reaction block [L]
r_i	Partially Non-dimensional horizontal reaction under ith pier [L]
$\boldsymbol{R}$	Non-dimensional quasi-static stifness matrix []
R_i	Horizontal reaction at i^{th} pier [F]
s	Number of supports []
$\mathbf{S}(\omega)$	power spectral density of dynamic response vector (PSD). [L]^2

S_{uu}	the power spectral density of the response of the u^{th} DOF. $[L]^2$
t	Time [T]
T	Kinetic Energy [F][L]
$u_{d,i}$	i^{th} Bridge deck DOF (including free and constrained DOFs) [L]
$u_{t,i}$	i^{th} Bridge deck DOF (including only free DOFs) [L]
$\mathbf{u}$	Dynamic bridge deck DOF vector [L]
$\mathbf{u}_d$	Bridge deck DOF vector (including free and constrained DOFs) [L]
$\mathbf{u}_g$	Ground DOF vector [L]
$\mathbf{u}_s$	Pseudo-static bridge deck DOF vector[L]
$\mathbf{u}_t$	Bridge deck DOF vector (including only free DOFs) [L]
U	Potential Energy [F][L]
y_d	Deck transversal displacement [L]
y_g	Ground transversal displacement [L]
$\alpha_{u,i}(\omega)$	the summation of power terms coefficient in the modal error of u^{th} DOF due to the i^{th} mode []
$\beta_{u,i}(\omega)$	the summation of cross-terms and phases coefficient in the modal error of u^{th} DOF due to the i^{th} mode []
$\mathbf{\Gamma}_i(\omega)$	i^{th} modal participation vector[]
Γ_{ip}	Participation factor i^{th} mode corresponding to p^{th} ground motion input []
γ_i	i^{th} modal damping ratio []
$\varepsilon_{u,i}(\omega)$	the modal error of u^{th} DOF due to the i^{th} mode $[L]^2$
$\varepsilon_{u,ij}(\omega)$	modal cross-analysis error of u^{th} DOF due to the i^{th} and j^{th} modes $[L]^2$
η_i	i^{th} pier to deck stiffness ratio []
ξ	Non-dimensional x coordinate along the length of the bridge []
Π	Lagrangian [F][L]
$\boldsymbol{\phi}_i$	Eigenvector of i^{th} mode []
Φ	Partial eigenvector matrix []

$\boldsymbol{\psi}$	Bridge deck Ritz vector []
$\boldsymbol{\psi}_g$	Ground DOF Ritz vector []
ω	Fourier frequency in the frequency domain [Rad][T]$^{-1}$
ϖ	System frequency parameter [Rad][T]$^{-1}$
ω_i	i^{th} modal Natural frequency [Rad][T]$^{-1}$

Chapter 3

A Generalized Nonlinear Multi-span Bridge System

The contents of this chapter have been adapted from the study (Meibodi and Alexander, 2020) that published in:

MEIBODI, A. & ALEXANDER, N. A. 2020. Exploring a generalized nonlinear multi-span bridge system subject to multi-support excitation using a Bouc-Wen hysteretic model. *Soil Dynamics and Earthquake Engineering*, 135, 106-160.

3.1 INTRODUCTION

The main aim of this chapter is to first develop a novel reduced order model that is capable of incorporating the hysteretic and inelastic behavior of bridge RC piers. This reduced-order model should contain the smallest reasonable set of degrees of freedom and system parameters. The simulation of the simplified bridge physics is not based on either modal projection or static condensation in a classic sense as these techniques are limited to elastic analysis. We reduce the number of system DOFs by using explicit assumptions, namely limiting plasticity to piers via the Bouc-Wen element, which provides a very efficient way of reducing system complexity and numerical run-times.

3.2 A NONLINEAR REDUCED-ORDER BRIDGE MODEL

The proposed model concerns the seismic analysis of ordinary standard highway bridges. In the area with medium to high seismicity, it is generally advisable and cost-effective that bridge piers are designed for ductile behavior (Bardakis and Fardis, 2011). Under the no-collapse requirement, flexural hinges are permitted to form in the piers to provide energy dissipation and to limit the overall design seismic action. The superstructure (a capacity-protected member) should be designed to remain essentially elastic in order to retain its functionality during/after seismic action. Therefore, in this context, nonlinear inelastic piers and a linear elastic deck shall be assumed in our proposed model as shown in Figure 2. This figure is a 2D plan view that shows the total deformation $y_t(x,t)$ of the bridge and piers in the horizontal x-y plane when subjected to ground deformations $y_g(x,t)$.

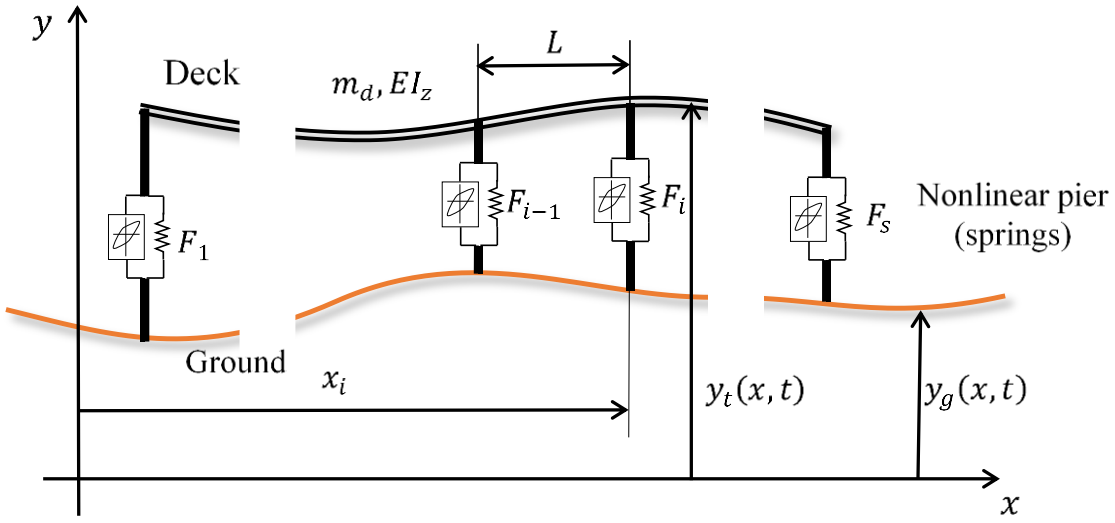

Figure 2; The *x-y* plan view of bridge layout including transversal deformation of piers, ground, and deck

The generalized bridge system consists of m degree of freedom resting on s support ($m > s$) nonlinear springs. F_i denotes hysteretic spring force at ith pier located at x_i coordinate. m_d (x) is mass per unit length and $EI_z(x)$ is the deck transversal flexural rigidity. It is assumed that the bridge deck is continuous longitudinally (with respect to transversal flexure) and ductile members are assumed as cantilever columns with a fixed base. Therefore, there is shear but no significant moment transfer from deck to piers.

The bridge has s-1 equal span with the length of length L and the overall bridge length is $(s-1)L$. The total bridge deck displacements can be re-expressed in terms of a moving coordinate frame as follows :

$$y_t = y + y_g \tag{3.1}$$

where $y(x,t)$ is the deck's transversal displacements relative to the moving ground. Using D'Alembert's principle (Chopra, 2007), the seismic acceleration induced inertial force per unit length on the deck is given by:

$$f_I = -m_d \ddot{y}_t \tag{3.2}$$

where, $m_d(x)$ is deck mass per unit length. The piers masses can be assumed lumped at the deck and ground levels and hence although superficially neglected they are present parametrically through $m_d(x)$. Note the Newtonian prime notation is used for derivatives of a spatial variable whereas the dot notation is used for derivatives of a temporal variable. External virtual work done by inertia force f_I acting through the virtual displacement $\Delta y(x)$:

$$\Delta W_E = \int_0^{(s-1)L} f_I \, \Delta y \, \mathrm{d}x \tag{3.3}$$

Similarly, the internal virtual work due to this virtual displacement $\Delta y(x,t)$ is given as:

$$\Delta W_I = \int_0^{(s-1)L} EI_z y_t'' \Delta y'' \, \mathrm{d}x + \sum_{i=1}^{s} \{F_i \Delta y(x_i)\} \tag{3.4}$$

The first term in the above expression is due to deck flexure, where EI_z is the transversal flexural rigidity of the deck, y_t'' is the deck curvature. The second term in the above equation is due to the work done by the nonlinear stiffness forces F_i in the i[th] pier in moving through a virtual displacement (deformation) $\Delta y(x_i)$. We introduce a spatiotemporal orthogonal basis (Rayleigh-Ritz) form for the ground and relative displacement respectively, as follows:

$$y(x,t) = \boldsymbol{\psi}(x)^T \mathbf{u}(t), \qquad y_g(x,t) = \boldsymbol{\psi}_g(x)^T \mathbf{g}(t) \tag{3.5}$$

Where column vector $\mathbf{u} \in \mathbb{R}^{m\times 1}$ denotes the degrees of freedom (DOFs) on the superstructure (deck) and vector $\mathbf{g} \in \mathbb{R}^{s\times 1}$ denotes restrained DOFs of ground. The orthogonal shape function vector for deck and ground is defined by $\boldsymbol{\psi}(x) \in \mathbb{R}^{m\times 1}, \boldsymbol{\psi}_g(x) \in \mathbb{R}^{s\times 1}$ respectively. Now if a Lagrangian interpolation scheme is used for ψ as follows:

$$\boldsymbol{\psi}^{\mathrm{T}} = \begin{bmatrix} \psi_1 & \psi_2 & \cdots & \psi_m \end{bmatrix}, \quad \psi_i(x) = \frac{\ell_i(x)}{\ell_i(x_i)}, \quad \ell_i(x) = \frac{\prod_{q=1}^{m}(x - x_p)}{(x - x_i)} \tag{3.6}$$

These Lagrangian interpolants have the added property that $\psi_i(x_i) = 1$ and $\psi_i(x_j) = 0$ ($\forall\ j \neq i$). Similarly, the known ground DOFs which include the coordinate of piers and abutments at ground level are defined by the similar orthogonal shape function vector as:

$$\boldsymbol{\psi}_g^T = \begin{bmatrix} \psi_1 & \psi_2 & \cdots & \psi_s \end{bmatrix}, \quad \psi_i(x) = \frac{\ell_i(x)}{\ell_i(x_i)}, \quad \ell_i(x) = \frac{\prod_{q=1}^{s}(x - x_p)}{(x - x_i)} \tag{3.7}$$

Now let the virtual displacements be defined as follows:

$$\Delta y = \boldsymbol{\psi}^T \Delta \mathbf{u} \tag{3.8}$$

Substituting Eq (3.5) and Eq (3.8) in Eq (3.3) and Eq (3.4) is given respectively:

$$\Delta W_E = -\int_0^{(s-1)L} m_d \left(\boldsymbol{\psi}^T \ddot{\mathbf{u}} + \boldsymbol{\psi}_g^T \ddot{\mathbf{g}}\right)\left(\boldsymbol{\psi}^T \Delta \mathbf{u}\right) \mathrm{d}x \tag{3.9}$$

$$\Delta W_I = \int_0^{(s-1)L} EI_z \left(\boldsymbol{\psi}''^T \mathbf{u} + \boldsymbol{\psi}_g''^T \mathbf{g}\right)\left(\boldsymbol{\psi}''^T \Delta \mathbf{u}\right) \mathrm{d}x + \sum_{i=1}^{s} \left\{F_i \left(\boldsymbol{\psi}(x_i)^T \Delta \mathbf{u}\right)\right\} \tag{3.10}$$

For a product of a row and column vector $\mathbf{a}^T\mathbf{b}$ is a scalar hence, $\mathbf{a}^T\mathbf{b}=\mathbf{b}^T\mathbf{a}$. Therefore, the above work Eq (3.9) and Eq (3.10) are re-expressed as follows:

$$\Delta W_E = -\Delta\mathbf{u}^T\left[\left(\int_0^{(s-1)L} m_d\ \boldsymbol{\psi}\boldsymbol{\psi}^T \mathrm{d}x\right)\ddot{\mathbf{u}} + \left(\int_0^{(s-1)L} m_d\ \boldsymbol{\psi}\boldsymbol{\psi}_g^T \mathrm{d}x\right)\ddot{\mathbf{g}}\right] \tag{3.11}$$

$$\Delta W_I = \Delta\mathbf{u}^T\left[\left(\int_0^{(s-1)L} EI_z\boldsymbol{\psi}''\boldsymbol{\psi}''^T \mathrm{d}x\right)\mathbf{u} + \left(\int_0^{(s-1)L} EI_z\boldsymbol{\psi}''\boldsymbol{\psi}_g''^T \mathrm{d}x\right)\mathbf{u} + \sum_{i=1}^{s} F_i\boldsymbol{\psi}(x_i)\right] \tag{3.12}$$

By employing virtual work principle ($\Delta W_I = \Delta W_E$), the final form of the equation of motion can be expressed as:

$$\overline{\mathbf{M}}\ddot{\mathbf{u}} + \overline{\mathbf{K}}_d\mathbf{u} + \sum_{i=1}^{s} F_i\boldsymbol{\psi}(x_i) = -\overline{\mathbf{L}}\ddot{\mathbf{g}} - \overline{\mathbf{K}}_g\mathbf{g} \tag{3.13}$$

where the dimensional system matrices are defined as follows:

$$\begin{aligned} &\overline{\mathbf{M}} = \int_0^{(s-1)L} m_d\boldsymbol{\psi}\boldsymbol{\psi}^T \mathrm{d}x \quad , \quad \overline{\mathbf{K}}_d = \int_0^{(s-1)L} EI_z\boldsymbol{\psi}''\boldsymbol{\psi}''^T \mathrm{d}x \\ &\overline{\mathbf{L}} = \int_0^{(s-1)L} m_d\boldsymbol{\psi}\boldsymbol{\psi}_g^T \mathrm{d}x, \quad \overline{\mathbf{K}}_g = \int_0^{(s-1)L} EI_z\boldsymbol{\psi}''\boldsymbol{\psi}_g''^T \mathrm{d}x, \end{aligned} \tag{3.14}$$

3.2.1 Incorporation of piers hysteretic energy to the system by Bouc-Wen model

The inelastic behavior of a dynamic system is associated with a hysteretic correlation between the resisting pier transversal force and deck-ground displacement (Song and Der Kiureghian, 2006). Under assumption of Bouc–Wen class models, the resisting force of i^{th} pier is derived by a summation of a hysteretic and an elastic component as (Charalampakis and Koumousis, 2006):

$$F_i = k_i\left\{\alpha u_i + (1-\alpha)u_{yi}z_i\right\} \tag{3.15}$$

$$F_{yi} = k_i u_{yi} \tag{3.16}$$

Where u_{yi} and k_i denote the pseudo-yield displacement and linear elastic stiffness of the i^{th} pier. Hence, F_{yi} denotes the pseudo-yield force for the i^{th} pier. α is the ratio of post- to pre-yield (elastic) stiffness and $z_i(t)$ is a dimensionless auxiliary variable that describes hysteretic behavior. The following auxiliary ordinary differential equation is employed to determine the hysteretic variable.

$$\dot{z}_i = \frac{1}{1+\delta_n \epsilon_n}\left\{A - \left(1+\delta_v \varepsilon_n\right)\left(\gamma \,\mathrm{sgn}(\dot{u}_i z_i) + \beta\right)\left|z_i\right|^n\right\}\frac{\dot{u}_i}{u_{yi}} \tag{3.17}$$

where A, β, γ, n are dimensionless parameters controlling the shape of hysteretic loops (δ_v, δ_n) are dimensionless parameters to incorporate strength deterioration and stiffness degradation respectively. These values are identical for all piers as they are only dependent on the physical characteristic of a column. The parameter ϵ_n is dissipated energy normalized by $F_{yi}u_{yi}$ given as:

$$\epsilon_n(t) = (1-\alpha)\int_0^t \frac{\dot{u}_i}{u_{yi}} z_i \,\mathrm{d}t \tag{3.18}$$

With suitably chosen values of parameters γ and β, the model can generate a hysteretic loop corresponding to the physical properties of the system (Sivaselvan and Reinhorn, 2000). It is convenient and proven that conditions $A = \beta + \gamma = 1$ simplify the representation of the Bouc-Wen model for engineering purposes provided compatibility with smooth softening hysteretic characteristic of structures (Charalampakis and Koumousis, 2006, Giaralis and Spanos, 2013). The suggested range of degradation parameters are

$0 \le \delta_n \le 0.3$ and $0 \le \delta_v \le 0.05$ (Ma et al., 2004, Goda et al., 2009). The Bouc-Wen parameters $A = 1, \beta = \gamma = 0.5, \alpha = 0.15$ are adopted to exhibit a smooth softening-strain model (Giaralis and Spanos, 2013), as well as the degradation parameters, δ_n, δ_v which are taken equal to 0.3 and 0.05 respectively throughout analyses in this study. Figure 3 shows the schematic of the hysteretic system as well as hysteretic loops of different restoring force peaks normalized to the yielding force where the bridge piers are subjected to synchronous harmonic excitation.

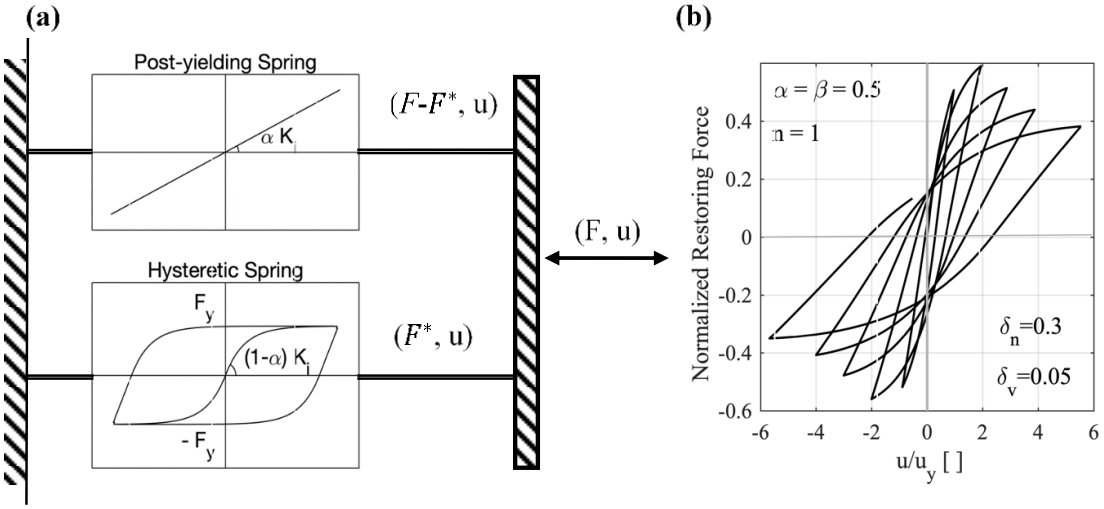

Figure 3;(a) the idealized hysteretic system with a post-yielding and a hysteretic spring; (b) force-displacement cycle represented by the Bouc-Wen model with strength deterioration and stiffness degradation under synchronous excitation.

Vectors $\boldsymbol{\psi}(x_i) \in \mathbb{R}^{m\times 1}$ and $\boldsymbol{\psi}_g(x_i) \in \mathbb{R}^{s\times 1}$ are single-entry vectors containing a single unity at the DOF locations corresponding to the i^{th} pier. All other vector elements are zero which is a natural consequence of Eq(3.6). So, we can introduce the following relationships:

$$u_i = \boldsymbol{\psi}\left(x_i\right)^T \mathbf{u}, \quad z_i = \boldsymbol{\psi}_g\left(x_i\right)^T \mathbf{z} \tag{3.19}$$

Where the vector containing all the auxiliary variables is defined as follows:

$$\mathbf{z} = \left[z_1(t), z_2(t), \dots, z_s(t) \right]^T \in \mathbb{R}^{s\times 1} \tag{3.20}$$

Substituting Eq (3.15) and Eq (3.19) into the hysteretic term in the Eq (3.13) we obtain

$$\sum_{i=1}^{s} \boldsymbol{\psi}(x_i) F_i = \bar{\mathbf{K}}_u \mathbf{u} + \bar{\mathbf{K}}_z \mathbf{z} \tag{3.21}$$

Where matrices are defined as follows:

$$\begin{aligned} \bar{\mathbf{K}}_u &= \alpha \sum_{i=1}^{s} k_i \, \boldsymbol{\psi}\left(x_i\right) \boldsymbol{\psi}\left(x_i\right)^T \in \mathbb{R}^{m\times m}, \\ \bar{\mathbf{K}}_z &= \left(1-\alpha\right) \sum_{i=1}^{s} \left(k_i \, u_{yi} \boldsymbol{\psi}\left(x_i\right) \boldsymbol{\psi}_g\left(x_i\right)^T \right) \in \mathbb{R}^{m\times s} \end{aligned} \tag{3.22}$$

By adding this hysteretic term, Eq (3.21) to the dynamical system, the final form would be as:

$$\overline{\mathbf{M}}\,\ddot{\mathbf{u}} + \overline{\mathbf{K}}_d \,\mathbf{u} + \overline{\mathbf{K}}_s \,\mathbf{u} + \overline{\mathbf{K}}_z \mathbf{z} = -\overline{\mathbf{L}}\ddot{\mathbf{g}} - \overline{\mathbf{K}}_g \mathbf{g} \tag{3.23}$$

3.2.2 System parameters of the nonlinear system

It is rational that the units of the system equation are partially or fully removed by a non-dimensionalization process. This technique provides simplification to present the problem throughout dimensionless parameters, where the intrinsic properties of the system would be recovered.

We introduce a dimensionless coordinate $x = \xi L$ and assume that the mass per unit length m_d and flexural rigidity EI_z remains constant. By application of change of variable

rule from Differential calculus (Hilton, 1958), The dynamical Eq (3.23) is re-cast as:

$$\mathbf{M}\ddot{\mathbf{u}}+\left(\mathbf{K}_d+\mathbf{K}_u\right)\mathbf{u}+\mathbf{K}_z\mathbf{z}=-\mathbf{L}\ddot{\mathbf{g}}-\mathbf{K}_g\mathbf{g} \tag{3.24}$$

Where matrices are defined as follows:

$$\mathbf{M}=\int_0^{(s-1)}\boldsymbol{\psi}\boldsymbol{\psi}^T\mathrm{d}\xi\in\mathbb{R}^{m\times m},\quad \mathbf{K}_d=\varpi^2\int_0^{(s-1)}\boldsymbol{\psi}''\boldsymbol{\psi}''^T\mathrm{d}\xi\in\mathbb{R}^{m\times m} \tag{3.25}$$

$$\mathbf{K}_u=\alpha\varpi^2\sum_{i=1}^{s}\eta_i\,\boldsymbol{\psi}\boldsymbol{\psi}^T\in\mathbb{R}^{m\times m},\quad \mathbf{K}_z=\left(1-\alpha\right)\varpi^2\sum_{i=1}^{s}\eta_i u_{yi}\boldsymbol{\psi}\left(x_i\right)\boldsymbol{\psi}_g\left(x_i\right)^T\in\mathbb{R}^{m\times s} \tag{3.26}$$

$$\mathbf{L}=\int_0^{(s-1)}\boldsymbol{\psi}\boldsymbol{\psi}_g^T\,d\xi\in\mathbb{R}^{m\times s},\quad \mathbf{K}_g=\varpi^2\int_0^{(s-1)}\boldsymbol{\psi}''\boldsymbol{\psi}_g''^T\,d\xi\in\mathbb{R}^{m\times s} \tag{3.27}$$

Where, frequency system parameters ϖ and dimensionless system parameter η_i which denotes the i^{th} pier to deck stiffness ratio, are defined as follows:

$$\varpi^2=\frac{EI_z}{m_dL^4},\qquad \eta_i=\frac{k_iL^3}{EI_z} \tag{3.28}$$

3.2.3 Rayleigh damping model

The most common method to model damping in the context of MDOF systems is to assume viscous damping. This approach was first introduced by Rayleigh (1896). Modes of proportionally damped systems preserve the simplicity of the real normal modes as in the undamped case. Unfortunately, there is no physical reason why a general system should behave like this. In fact, practical experience in modal testing shows that most real-life structures do not do so, as they possess complex modes instead of real normal modes. This implies that in general linear systems are non-classically damped. When the system is non-classically damped, some or all of the N differential equations of motion are coupled and

can not be reduced to N second-order uncoupled equation. This coupling brings several complications in the system dynamics – the eigenvalues and the eigenvectors no longer remain real and also the eigenvectors do not satisfy the classical orthogonality relationship as given by Eq (2.33).

An usual approach, in this case, is simply to ignore the off-diagonal terms of the modal damping matrix which couple the equations of motion. This approach is termed the decoupling approximation. For large-scale systems, the computational effort in adopting the decoupling approximation is an order of magnitude smaller than the methods of complex modes. The solution of the decoupled equation would be close to the exact solution of the coupled equations if the non-classical damping terms are sufficiently small.

In this study, it is assumed that the elasto-mechanical system follows the classical, proportional damping model (Clough and Penzien, 1995). The basic assumption is that a classical damping matrix can be diagonalized throughout a dynamic matrix of the undamped system. For the sake of simplicity, the viscous damping mechanism is modeled using only the linear-system terms, hence:

$$\mathbf{C} = \beta_m \mathbf{M} + \beta_k \left(\mathbf{K}_d + \mathbf{K}_u \right) \tag{3.29}$$

where β_m and β_k are mass-proportional and stiffness-proportional damping coefficients respectively.

3.2.4 Adding abutment constraints and the final form of the equation of motion

The two DOFs at the ends of the deck (the abutments) have the same displacement as the ground. Therefore, we should either augment equations of motions (3.24) with Lagrange multiplier and constraint equations or partition and condense equations of motion (3.24); the latter is chosen as it reduces the sizes of all matrices and aids computational

efficiency.

Herein, it is assumed that the bridge deck lays on the valley at its two ends and therefore the relative transversal displacement at the two ends is known $u_1(t) = u_m(t) = 0$. Hence, the DOFs of ground and deck are reordered as:

$$\mathbf{u} = \begin{bmatrix} u_1 = 0 \\ u_m = 0 \\ \hdashline u_2 \\ \vdots \\ u_{m-1} \end{bmatrix} = \begin{bmatrix} \mathbf{0} \\ \mathbf{w} \end{bmatrix}, \quad \mathbf{z} = \begin{bmatrix} \mathbf{0} \\ \mathbf{z}_I \end{bmatrix} \tag{3.30}$$

where $\ddot{\mathbf{g}}_E \in \mathbb{R}^{2\times 1}$ denotes the ground acceleration time-series at exterior supports of the bridge, $\ddot{\mathbf{g}}_I \in \mathbb{R}^{(s-2)\times 1}$ denotes the ground acceleration time-series at the inner pier columns, and $\mathbf{w} \in \mathbb{R}^{(m-2)\times 1}$ is the vector of relative displacement at the free (unconstrained) DOFs of the superstructure (deck). Similarly, $\mathbf{z}_I$ denote auxiliary hysteretic displacements of deck DOFs at interior piers. Now, matrix partitioning is employed to decouple the constrained from unconstrained DOFs as follows:

$$\begin{aligned} &\begin{bmatrix} \mathbf{M}_{11} & \mathbf{M}_{12} \\ \mathbf{M}_{12}^T & \mathbf{M}_{22} \end{bmatrix} \begin{bmatrix} \mathbf{0} \\ \ddot{\mathbf{w}} \end{bmatrix} + \begin{bmatrix} \mathbf{C}_{11} & \mathbf{C}_{12} \\ \mathbf{C}_{12}^T & \mathbf{C}_{22} \end{bmatrix} \begin{bmatrix} \mathbf{0} \\ \dot{\mathbf{w}} \end{bmatrix} + \begin{bmatrix} \mathbf{K}_{d11} & \mathbf{K}_{d12} \\ \mathbf{K}_{d,12}^T & \mathbf{K}_{d22} \end{bmatrix} \begin{bmatrix} \mathbf{0} \\ \mathbf{w} \end{bmatrix} + \dots \\ &\begin{bmatrix} \mathbf{K}_{u11} & \mathbf{K}_{u12} \\ \mathbf{K}_{u12}^T & \mathbf{K}_{u22} \end{bmatrix} \begin{bmatrix} \mathbf{0} \\ \mathbf{w} \end{bmatrix} + \begin{bmatrix} \mathbf{K}_{z11} & \mathbf{K}_{z12} \\ \mathbf{K}_{z12}^T & \mathbf{K}_{z22} \end{bmatrix} \begin{bmatrix} \mathbf{0} \\ \mathbf{z}_I \end{bmatrix} = -\begin{bmatrix} \mathbf{L}_{11} & \mathbf{L}_{12} \\ \mathbf{L}_{12}^T & \mathbf{L}_{22} \end{bmatrix} \begin{bmatrix} \ddot{\mathbf{g}}_E \\ \ddot{\mathbf{g}}_I \end{bmatrix} - \begin{bmatrix} \mathbf{K}_{g11} & \mathbf{K}_{g12} \\ \mathbf{K}_{g12}^T & \mathbf{K}_{g22} \end{bmatrix} \begin{bmatrix} \mathbf{g}_E \\ \mathbf{g}_I \end{bmatrix} \end{aligned} \tag{3.31}$$

and partitioned to achieve the reduced and final form of the equations of motion for this generalized nonlinear bridge system as follow:

$$\mathbf{M}_{22}\ddot{\mathbf{w}} + \mathbf{C}_{22}\dot{\mathbf{w}} + (\mathbf{K}_{d22} + \mathbf{K}_{u22})\mathbf{w} + \mathbf{K}_{z22}\mathbf{z}_I = -\mathbf{L}_{12}^T\ddot{\mathbf{g}}_E - \mathbf{L}_{22}\ddot{\mathbf{g}}_I - \mathbf{K}_{g12}\mathbf{g}_E - \mathbf{K}_{g22}\mathbf{g}_I \tag{3.32}$$

Where $\mathbf{w} \in \mathbb{R}^{(m-2)\times 1}$ denotes the relative displacement at free (unconstraint) DOFs. Hence the equations of motion are defined by Eq (3.17) and Eq (3.32)

The key feature of the proposed dynamic system is to represent the inelastic structural equation of motion throughout with only a small number of system parameters. These parameters consist of two parts: (i) Linear system parameters including frequency system parameters ω and pier to deck stiffness ratio η_i Which express linear properties of the bridge and (ii) Hysteretic parameters which quantify deformation ductility capacity in the RC piers. Note that all Bouc-Wen model parameters $A, \beta, \gamma, \alpha, \delta_n, \delta_v$ are dependent on the physical characteristic of the concrete structure and are generically considered constant for all piers of a bridge. However, yield displacement u_{yi} (of the ith pier) depends on design philosophy/geometry. This is discussed further in the next section.

3.2.5 Estimation of yielding displacements

In order to estimate of local ductility capacity of piers, the yielding displacement should be calculated. It is assumed that no bearing and isolation are incorporated into the bridge structure. Hence, all piers are designed for the ductile behavior necessary for a dissipating mechanism. The yield displacement of the piers at the point of the intended plastic hinge is estimated in our study as (Yashinsky and Ostrom, 2000):

$$u_{yi} = \frac{h_i^2}{3}\phi_{yi} \tag{3.33}$$

Where h_i is the height of the ith column, ϕ_{yi} denotes the idealized curvature at the yield point determined by the M-φ curve of the cross-section at the formation of the plastic hinge. The yield curvature of the rectangular column is estimated by the following dimensionless formulation (Priestley, 2000):

$$\phi_{yi} = \frac{2.12\,\varepsilon_{yi}}{d_i} \tag{3.34}$$

Where ε_{yi} denotes the yield strain of the reinforcement bar in the columns and d_i is the depth of the i^{th} pier's sections. Substituting Eq (3.34) in Eq (3.33) gives:

$$\frac{u_{yi}}{h_i} = 0.71\varepsilon_{yi}\frac{h_i}{d_i}\frac{u_{yi}}{h_i} = 0.71\varepsilon_{yi}\frac{h_i}{d_i} \tag{3.35}$$

where design yield drift ratio $\left(u_{yi}/h_i\right)$ is a function of pier span/depth ratio $\left(h_i/d_i\right)$ and yield strain ε_{yi}.

3.3 SUMMARY

The simplified time-history model has been developed accounting for spatial variability ground motion. The dissipation zone (plastic hinge) was allowed to occur at vertical components (piers). The bridge deck has been considered for linear behavior to remain its functionality during seismic action. The design 'philosophy' of the proposed model is applicable to the bridge category with non-collapse (ultimate limit state) requirement in a region with medium to high seismicity. The hysteresis behavior of a bridge was associated using the Bouc-Wen model. This hysteretic model incorporates parameters δ_n, δ_v to express strength deterioration and stiffness degradation respectively. The suitable range of Bouc-Wen model parameters for RC piers has been suggested for the future parametric study.

3.4 NOMENCLATURE

Dimensions in the following list are force [F], length [L], and time [T] with non-dimensional angles defined in Radians [Rad] and other dimensionless quantities defined by [ ].

$\mathbf{A}, \boldsymbol{\beta}, \boldsymbol{\gamma}$	Basic hysteresis shape control **[]**
$\mathbf{B}_1, \mathbf{B}_2, \mathbf{B}_3$	State-space system matrices []
$\mathbf{C}$	Non-dimensional damping matrices []
$\mathbf{C}_{11}, \mathbf{C}_{12}, \mathbf{C}_{22}$	Non-dimensional damping block matrices []
d_c	Depth of the pier's sections [L]
EI_d	Deck flexural rigidity (about z-axis) [F][L]^2
$f_I(x,t)$	inertia force [F]
F_i	hysteretic spring force at i^{th} pier [F]
F_{yi}	Yield force of i^{th} pier [F]
$\mathbf{g}$	Ground DOFs vector []
$\mathbf{g}_E$	Ground DOFs vector at exterior/end supports []
$\mathbf{g}_I$	Ground DOFs vector at interior pier supports []
I_d	The moment of inertia of deck [L]^4
I_{ci}	The moment of inertia of i^{th} pier [L]^4
k_i	Pier transversal flexural stiffness [F][L]$^{-1}$
$\mathbf{K}_d$	Non-dimensional deck stiffness matrix []
$\overline{\mathbf{K}}_d$	Generalized deck stiffness matrix [F][L]$^{-1}$
$\mathbf{k}_{d,11}, \mathbf{k}_{d,12}, \mathbf{k}_{d,22}$	Non-dimensional block deck stiffness matrices []
$\mathbf{K}_g$	Non-dimensional ground stiffness matrix []
$\overline{\mathbf{K}}_g$	Generalized ground stiffness matrix [F][L]$^{-1}$

$\mathbf{k}_{g,11}, \mathbf{k}_{g,12}, \mathbf{k}_{g,22}$	Non-dimensional block ground stiffness matrices []
$\mathbf{K}_u$	Non-dimensional pier stiffness matrix []
$\bar{\mathbf{K}}_u$	Generalized pier stiffness matrix [F][L]$^{-1}$
$\mathbf{k}_{u,11}, \mathbf{k}_{u,12}, \mathbf{k}_{u,22}$	Non-dimensional block Pier stiffness matrices []
$\mathbf{K}_z$	Non-dimensional hysteretic stiffness matrix [L]
$\mathbf{k}_{z,11}, \mathbf{k}_{z,12}, \mathbf{k}_{z,22}$	Non-dimensional block hysteretic stiffness matrices [L]
$\bar{\mathbf{K}}_z$	Generalized hysteretic stiffness matrix [F]
L	Span length [L]
$\bar{\mathbf{L}}$	Generalized excitation factor []
$\mathbf{L}$	Non-dimensional excitation factor []
$\mathbf{L}_{11}, \mathbf{L}_{12}, \mathbf{L}_{22}$	Non-dimensional block excitation factor []
m	Number of deck DOFs []
m_d	Deck mass per unit length [F][T]^2[L]$^{-2}$
$\mathbf{M}$	Non-dimensional mass matrix []
$\bar{\mathbf{M}}$	Generalized mass matrix []
$\mathbf{M}_{11}, \mathbf{M}_{12}, \mathbf{M}_{22}$	Non-dimensional block mass matrices []
n	Sharpness of yield []
PGA	Peak ground acceleration [L] [T]$^{-2}$
s	Number of Piers []
t	Time [T]
$\mathbf{u}$	Bridge deck DOFs vector (including free and constrained DOFs) [L]
u_{yi}	yield displacement of ith pier [L]
$y\ (x,t)$	transversal displacement relative to the ground at time t [L]
$y_t(x,t)$	transversal total displacement at time t [L]

$y_g\ (x,t)$	The transversal deformation of the ground at time t [L]
$\mathbf{w}$	Deck displacement DOFs (including only free DOFs) [L]
$z_i(t)$	dimensionless auxiliary variable []
z(t)	Hysteretic vector of Deck DOFs []
$\mathbf{z}_E$	Hysteretic DOFs vector at exterior/end supports []
$\mathbf{z}_I$	Hysteretic DOFs vector at interior pier supports []
α	post- to preyield stiffness ratio; []
β_m, β_k	Rayleigh damping coefficients []
γ_i	i^{th} modal damping ratio []
δW_I	Internal virtual work [F][L]
δW_E	External virtual work [F][L]
δy(x)	Virtual displacement [L]
δ_v	Strength degradation []
δ_n	Stiffness degradation []
ϵ_n	Normalized dissipated energy []
ε_y	Nominal yield strain []
ξ	Non-dimensional *x* coordinate along the length of the bridge []
η_i	i^{th} pier to deck stiffness ratio []
Π	Lagrangian [F][L]
Φ_Y	idealized curvature at the yield point $[L]^{-1}$
$\boldsymbol{\psi}$	Bridge deck Ritz vector []
$\boldsymbol{\psi}_g$	Ground DOFs Ritz vector []
ϖ	System frequency parameter $[Rad][T]^{-1}$

Chapter 4

Seismic Ground Motion Input

The contents of this chapter have been partially adapted from the study (Meibodi et al., 2020, Meibodi and Alexander, 2020, Meibodi and Alexander, 2021) that published in:

MEIBODI, A. & ALEXANDER, N. A. 2020. Exploring a generalized nonlinear multi-span bridge system subject to multi-support excitation using a Bouc-Wen hysteretic model. *Soil Dynamics and Earthquake Engineering,* 135**,** 106-160.

MEIBODI, A. A. & ALEXANDER, N. A. 2021. Spatiotemporal seismic excitation of bridges with an anti-symmetrical first mode. *Bulletin of Earthquake Engineering*.

MEIBODI, A. A., ALEXANDER, N. A., NORMAN, J. A. & CREWE, A. J. 2020. A theoretical and experimental exploration of the seismic dynamics of multi-span bridges. *Bulletin of Earthquake Engineering*.

4.1 INTRODUCTION

In this study, we employ an actual seismic dataset from the SMART-1 (Taiwan) array rather than some artificially constructed spatiotemporal ground motion. The SMART-1 Array was one of the biggest seismic databases specifically used to explore the near-field characteristics of ground excitation (Abrahamson et al., 1987). The records from event 43 (IES, 1980- 1990) are used in this study. This seismic event with the epicenter close to the array is the largest event recorded at the SMART-1 Array. It occurred on 30/Jul/1986 at 11:31:47.5 (UTC), it had a magnitude of 6.2M_L. The epicenter of the event was at depth and distance of around 2 km and 5 km from the center of the array, respectively. The epicenter was discovered at an estimated bearing of 150° from the center of the array.

4.2 THE SMART-1 ACCELEROGRAPH ARRAY DATABASE

Over the last decades, several dense seismograph arrays have been installed to investigate spatial variation of seismic ground motions. It is a matter of concern when the practical engineers and scientific community try to understand the effect of spatially varying ground motions on extensive structures like bridges and dams. However, the absence of data for large magnitude events in most of the arrays like the El Centro differential array (Bycroft, 1980) provided a substantial uncertainty of strong ground motions. The first specially designed arrays of strong-motion seismograph called SMART-1 (with radius 2 km and 37 accelerometers) was able to record substantial ground excitation (up to 0.24g horizontal acceleration). It was in operation in September 1980 in an area of Taiwan with high seismicity. Throughout the first operational year, the SMART-1 array captured fifteen earthquakes with local magnitudes (M_L) in the range of 3.4 to 6.9. Three

seismic events that had shallow depths with epicentral distances from 59 to 76 km occurred right below the array instruments. The rest of the twelve events had focal depths of 1.8 to 76 km. The seismic recorded data from 27 triaxial accelerometers were taken from a magnitude 6.9 (M_L) seismic event in January 1981. However, SMART-1 was designed to record earthquakes much larger than this. The dynamic range of the triaxial forced-balanced instrument, SA-3000, was $\pm 1g$ suggesting events of the local magnitude of greater than M_L= 8.0 were permissible without clipping. However, no earthquakes occurred near this upper amplitude limit. The largest earthquake used a third of the available amplitude range. Thus, for events with low PGA noticeable quantization errors were impressed on the data. Consequently, we will use a set of the largest events detected by the array. Event-43 is the largest event recorded by the array and covers a range of magnitudes, depth, and epicenter distances.

The array consists of three concentric rings with radii of 0.2, 1, and 2 km, respectively namely the Inner ring donated by I, the Middle ring donated by M, and the Outer ring donated by O. Each circle has 12 equal-spaced stations, numbered from 1 to 12 and Central station C00 was situated at the center of rings see Figure 4. Two more stations, E01 and E02, were later incorporated into the array in 1983, at distances of 2.8 and 4.8 km respectively in the south direction of C00.

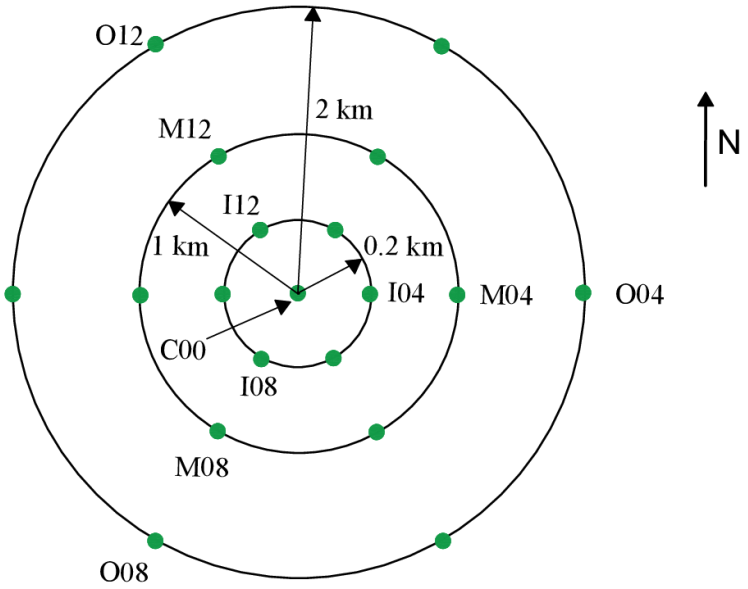

Figure 4; The layout of the SMART-1 accelerometers. The figure depicts the positions of Central station C00, inner stations (I01-I12), and outers stations (O01-O12). The location of stations E01 and E02 at distances of 2.8 and 4.8 km respectively in the south direction of C00 are not illustrated in these figures after (Abrahamson et al., 1987).

The array was set up in a sedimentary valley, mainly used for the Transplanting of rice. The water level in rice fields is at or close to ground level. The location of E02 was on a slate outcrop which is different from other station positions. In 1985, a new triaxial array, with a smaller scale, the Lotung Large Scale Seismic Test (LSST) array was added in the southwest of the SMART-1 array. The LSST array has 15 free-surface and 8 downhole three-component accelerometers.

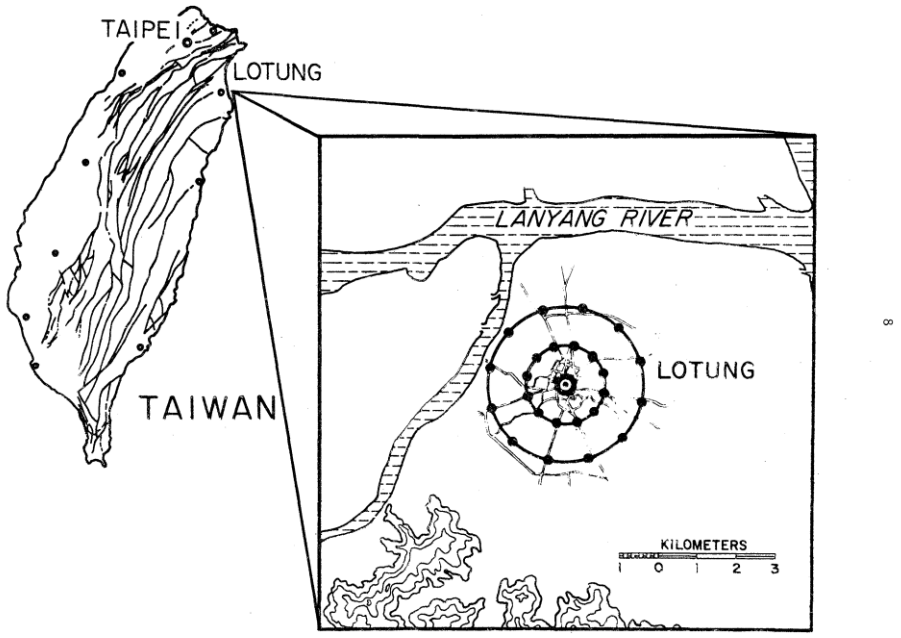

Figure 5; Geographic position of SMART-1 array in an earthquake-prone region in Taiwan, after (Abrahamson et al., 1987).

Figure 6 depicts the spatial variability of vertical ground accelerations for stations of the inner ring (I01-I012) at a particular moment in time. A biharmonic cubic spline interpolation scheme is employed to calculate surface values (Alexander, 2008). It can be suggested that there are substantial differential variants from the center station (C00) to stations of the inner ring.

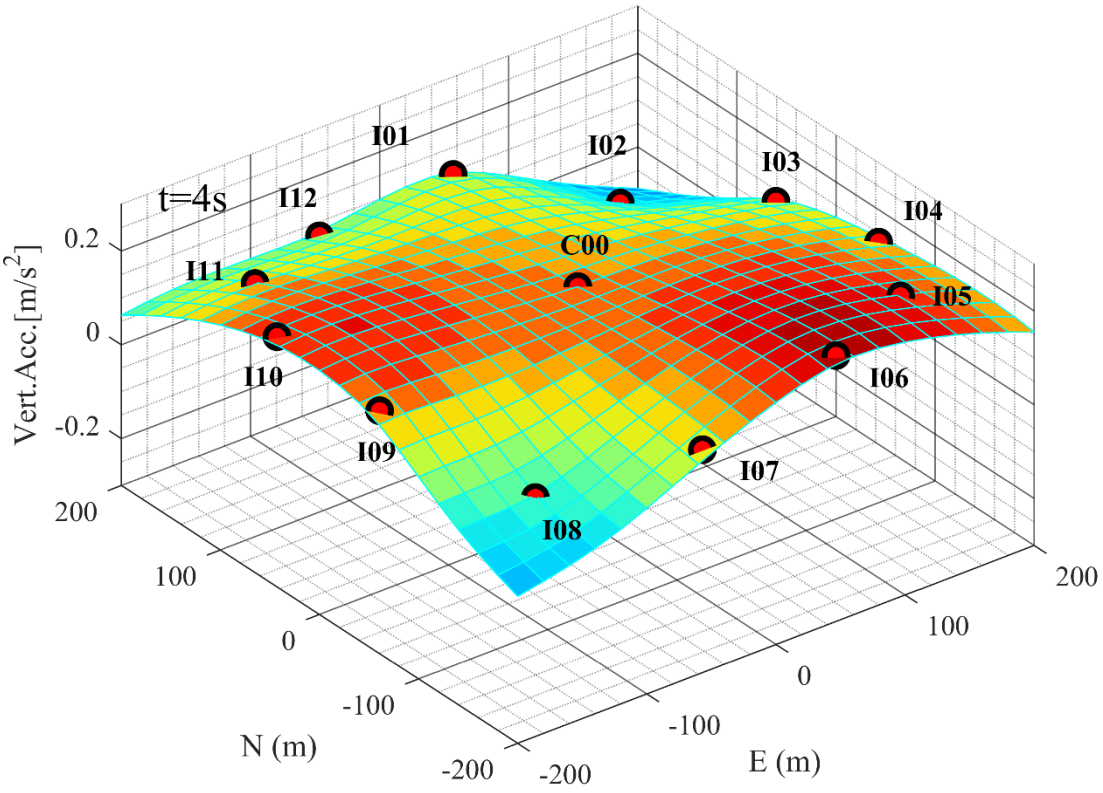

Figure 6; Illustration of typical spatial variability of seismic accelerations for inner stations (I01-I12).

4.3 GENERATION OF SEISMIC INPUT

In order to produce ground displacements, the rotated ground acceleration time-series are numerically integrated twice by Simpson's 1/3rd rule. Low-cut filtering is performed on the acceleration and the velocity-time histories to reduce the influence of spurious increasing trends in the displacement time histories. Very low-frequency Fling components (Chanerley and Alexander, 2010) were not extracted. The details of the correction procedure for these records are discussed in (Alexander et al., 2001, Chanerley and Alexander, 2007, Chanerley and Alexander, 2008). The location of the center station (C00) and inner (I00-I12) in a concentric circle with radii 200 m are illustrated in Figure 7. The array components are recorded in three directions: north, east, and vertical. The easterly $\ddot{a}_e$

and northerly $\ddot{a}_n$ components are rotationally transformed into a local coordinate system corresponding to the bridge longitudinal alignment. The fully spatiotemporal ground motion time-series across the array are estimated using a biharmonic interpolation (Alexander, 2008). Thus, using these interpolating functions we can estimate the two horizontal components of the ground motion anywhere in the inner circle of the SMART-1 array. From these two components we estimate the transversal (to the bridge) ground motion at the abutments and bridge pier supports for any bridge in any of 12 radial alignments as shown in Figure 7.

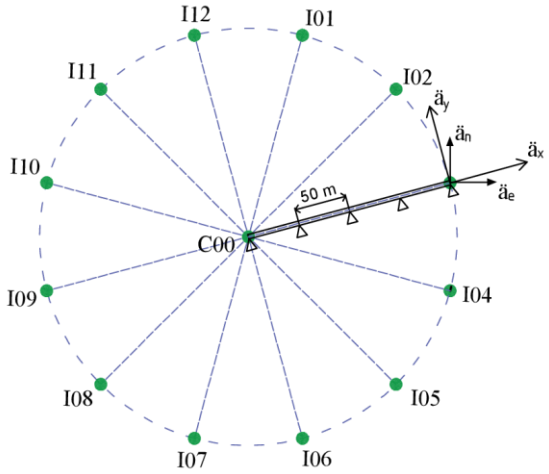

Figure 7; Example of radial bridge orientation and the configuration of SMART-1 array including center (C00) and inner ring station (I01-I12).

The acceleration components, $\ddot{a}_x$ radial and $\ddot{a}_y$ normal to radial acceleration at any stations are derived using a standard rotational transform function as:

$$\begin{bmatrix} \ddot{a}_x \\ \ddot{a}_y \end{bmatrix} = \begin{bmatrix} \cos\phi & \sin\phi \\ -\sin\phi & \cos\phi \end{bmatrix} \begin{bmatrix} \ddot{a}_e \\ \ddot{a}_n \end{bmatrix} \tag{4.1}$$

Where $(\ddot{a}_e, \ddot{a}_n)$ are easterly and northerly components of acceleration and ϕ is the anti-clockwise angle between the easterly component $\ddot{a}_e$ and radial direction of the bridge.

4.4 STOCHASTIC ESTIMATION OF SEISMIC DATA

Figure 8 (a) shows the power spectrum of the rotated seismic data at the center and inner ring station and co-spectrum between origin station C00 and selected inner ring stations. Note that in this figure the seismic data are rotated to be orthogonal to the bridge longitudinal orientation. The spectra are obtained using the Welch method (Welch, 1967) and a Hanning (Gruber, 1997) smoothing window function. It can be suggested from Figure 8 that the PSD at the chosen stations has closely analogous frequency contents in which, the peaks of the PSD curve for all stations occur at roughly 0.8 and 2 Hz.

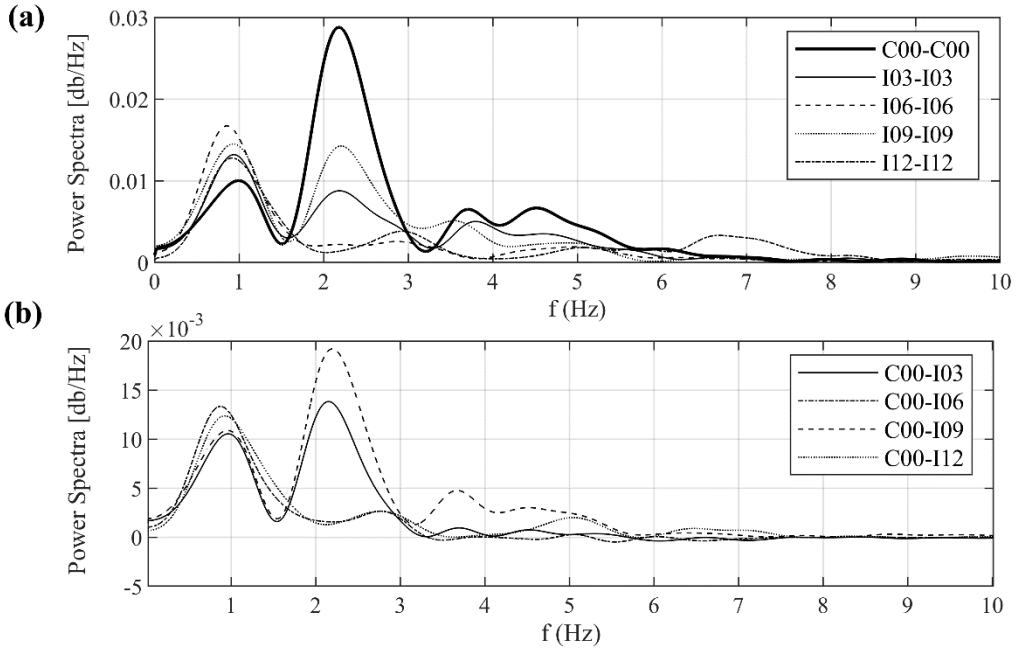

Figure 8; (a) Power Spectrum of acceleration time-series at selected inner ring station. PSD of station C00 is rotated with the orientation C00-I03.(b)Co-spectrum between C00 and selected inner ring stations of SMART-1 array for event 43.

The co-spectrum is derived from the cross-spectrum which provides helpful details to interpret seismic data. The co-spectrum is the real part of the cross-spectral density function at two different stations. Figure 8 (b) indicates that in the range of dominant frequency (up to 5 Hz), the phase difference spectra are primarily positive. From 5 Hz

onwards, the co-spectrum starts to fluctuate around the x-axis and reach negative values at some frequencies. However, the amplitude of seismic waves in this range is small.

In this study, it is assumed that the ground motion inputs are stationary and homogenous. The assumption of stationarity implies that the stochastic descriptors of the motions do not depend on absolute time, but are functions of time differences (or time lag) only. The concept of homogeneity is similar to that of stationarity. Homogeneity, generally, refers to the space variables and implies that the stochastic descriptors of the motions are functions of the separation distance-vector, but not of the absolute location of the stations, the same way that stationarity, which refers to the time variable, implies dependence on the time lag only but not the absolute time. Physically, homogeneity suggests that the power spectral densities of the seismic motions at different recording stations do not vary significantly, i.e., they are station-independent.

Clearly, the power spectral densities of Figure 8 differ at the various stations of the SMART-1 array, but, on the average, their frequency content follows the same trend with fluctuations. It is, generally, considered that seismic data recorded at dense instrument arrays, which are located on uniform site conditions, are homogeneous. The assumption of homogeneity, however, is not valid for seismic ground. Variable site conditions can have a significant effect on, e.g., the seismic response of highway bridges crossing narrow sediment valleys, when their lateral supports rest on a rock outcrop and their middle supports on the sediments.

4.5 ELASTIC RESPONSE SPECTRA FOR SMART-1 ARRAY

Figure 9 displays the elastic response spectra for station accelerograms for north-south and east-west directions. These plots are suggestive of significant spatial incoherence,

particularly in the east-west directions (at 6Hz).

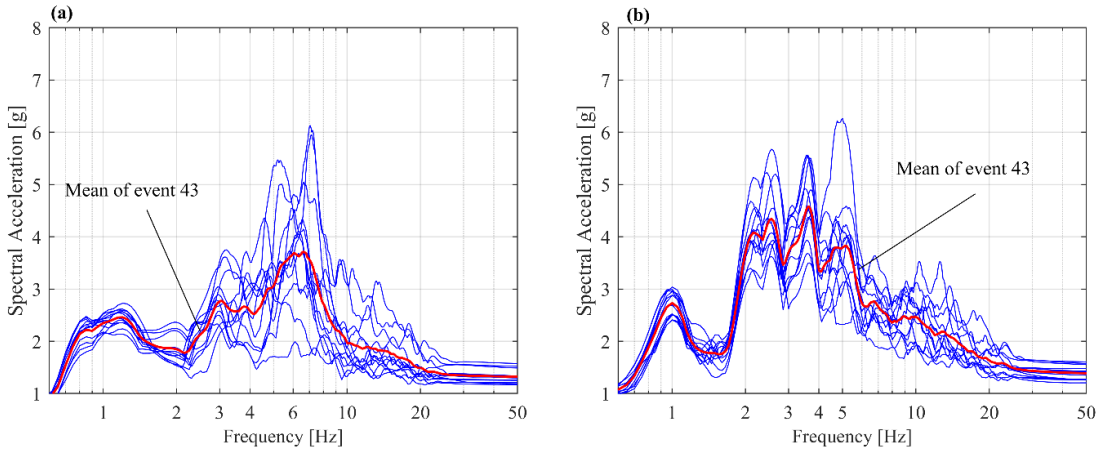

Figure 9. Elastic response spectra for SMART-1 Array inner ring stations I00 to I12 for event 43 for (a) East-West Component and (b) North-South Component.

4.6 TIME SERIES OF SEISMIC INPUT

Figure 10 represents the rotated time histories series in bridge transversal direction at the central station and selected stations of the inner ring (I03, I06, I09, and I12). The ground motion acceleration records are directly used in this study as seismic input for abutments.

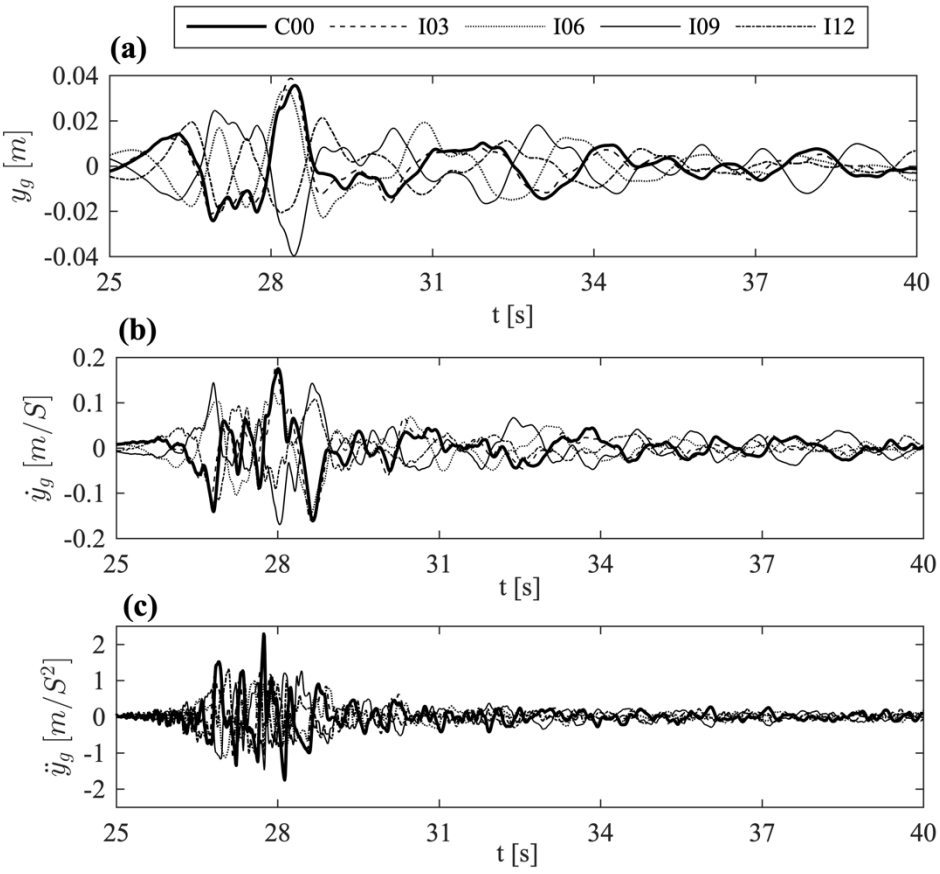

Figure 10; rotated time histories recorded at selected stations of the inner ring from SMART-1 array (event 43), (a) ground motion displacement input (b) ground motion velocity input (c) ground motion acceleration input.

4.7 SUMMARY

The set of times-series from the SMART-1 (Taiwan) array was chosen to generate seismic excitation input in this study. The event 43 was selected as it is the largest event recorded by the accelerometers. The data processing and modification of recorded time-series have been reviewed. The spatial distribution of accelerometers in the SMART-1 array has been illustrated. The random vibration approach has been deployed to describe excitations in the frequency domain. These plots indicate the presents of low-frequency spatial correlations between seismic inputs. Time-histories series at selected stations in the normal direction to the bridge longitudinal axis (i.e. normal a SMART-1 radial axis and

transversal to the SMART-1 circle) have been derived using a rotational transformation matrix.

Chapter 5

System Identification and Model Validation

The contents of this chapter have been partially adapted from the study (Meibodi et al., 2020) that published in:

MEIBODI, A. A., ALEXANDER, N. A., NORMAN, J. A. & CREWE, A. J. 2020. A theoretical and experimental exploration of the seismic dynamics of multi-span bridges. *Bulletin of Earthquake Engineering*.

5.1 INTRODUCTION

The calibration/validation of the mathematical model for a dynamical structure is a vital step in the process of structural analysis (Alvin et al., 2003, Zapico-Valle et al., 2010). Over the recent decade, several identification methods have been established to estimate unknown parameters of dynamical structural systems based on experimental data (Ljung, 1995, Ibrahim, 2002, Zhou and Chelidze, 2008). Ibrahim (2002) introduced a time-domain algorithm based on generalized eigenvalue decomposition. Least-Squares Complex Exponential Method has been developed based on Prony's method (Zhou and Chelidze, 2008). In these methods or any time-domain algorithms introduced later, it is assumed that the solution is a summation of some complex exponential terms. From these terms, the modal damping and frequency can be obtained implicitly. These methods are known as black-box methods (Ljung, 1995) as there is no need for the equation of motion of the structure.

However, State-space models provides explicit techniques of linear multi-input multi-output (MIMO). This representation allows the direct estimation of unknown parameters if the explicit equations of motion demonstrating the physics of the dynamical system can be expressed mathematically. These methods known as Grey-Box (Ljung, 1987) require that the equation of the dynamical system is expressed in the framework of ordinary differential or difference equations (ODEs).

The mathematical background and details of system identification methods are fully expressed in well-known books (Ljung, 1987, Söderström and Stoica, 1988). The overview of basic principles and innovation in this field has been sketched in the article 'Perspectives on system identification' by Ljung (Ljung, 2010).

5.2 STATE-SPACE EQUATIONS OF DYNAMIC MODEL

In this section, we aim to re-cast the equations of motion (2.29) in a form that permits system identification of a multi-input-multi-output (MIMO) system. A general linear time-invariant (LTI) system typically has a state-space form as follows:

$$\begin{bmatrix} \dot{\mathbf{x}}(\tau) \\ \mathbf{y}(\tau) \end{bmatrix} = \begin{bmatrix} \mathbf{A}(\boldsymbol{\theta}) & \mathbf{B}(\boldsymbol{\theta}) \\ \mathbf{C}(\boldsymbol{\theta}) & \mathbf{D}(\boldsymbol{\theta}) \end{bmatrix} \begin{bmatrix} \mathbf{x}(\tau) \\ \mathbf{f}(\tau) \end{bmatrix}, \qquad \mathbf{x}(\tau) = \begin{bmatrix} \mathbf{w}(\tau) \\ \dot{\mathbf{w}}(\tau) \end{bmatrix} \tag{5.1}$$

Where $\mathbf{f}(\tau)$, $\mathbf{x}(\tau)$ and $\mathbf{y}(\tau)$ are system input, state, and observed output (measured displacement) respectively. The block matrices in Eq (2.29) are defined as follows:

$$\mathbf{A}(\boldsymbol{\theta}) = \begin{bmatrix} \mathbf{0} & \mathbf{I} \\ -\mathbf{M}_{11}^{-1}\mathbf{K}_{11} & -\mathbf{M}_{11}^{-1}\mathbf{C}_{22} \end{bmatrix}, \quad \mathbf{B}(\boldsymbol{\theta}) = \begin{bmatrix} \mathbf{0} \\ \mathbf{N}_a \end{bmatrix}, \tag{5.2}$$

$$\mathbf{C}(\boldsymbol{\theta}) = [\mathbf{j} \quad \mathbf{0}], \quad \mathbf{D}(\boldsymbol{\theta}) = \mathbf{0} \tag{5.3}$$

where matrices **0**, **I** and **j** denote null, identity, and all-ones matrices respectively. The vector **θ** is a set of system parameters that are optimization arguments.

5.3 PARAMETER IDENTIFICATION OF LINEAR BRIDGE SYSTEM

5.3.1 Physical experimental model

The reference bridge studied in (Lupoi et al., 2005, Crewe and Norman, 2006, Alexander et al., 2006) is selected to exemplify the proposed procedure. The bridge model is a 1:50 scale model of a prototype 200m long bridge. The bridge has 4 spans 50m long and is supported by two abutments and three piers. In this experimental study, the piers are

of an equal length of 1m. A 200m long bridge was chosen because similar bridges have been used in studies by (Zapico et al., 2003, Lupoi et al., 2005) and these studies have shown that bridges of this size may be susceptible to a significant increase in response when considering MSE. The length was also chosen because a large proportion of bridges on major road projects are of a similar length. For example, on the new Egnatia Motorway in Greece, 103 of the 612 bridges were between 100m and 300m long, whilst only 4 were longer than 600m (Ahmadi-Kashani, 2004).

Table 1; Structural parameters and estimated model parameters for the experimental bridge

Parameters	Value	Units
m_b	125	[kg/m]
EI_z	4.46E+04	[Nm^2]
k_i	1.42E+05	[N/m]

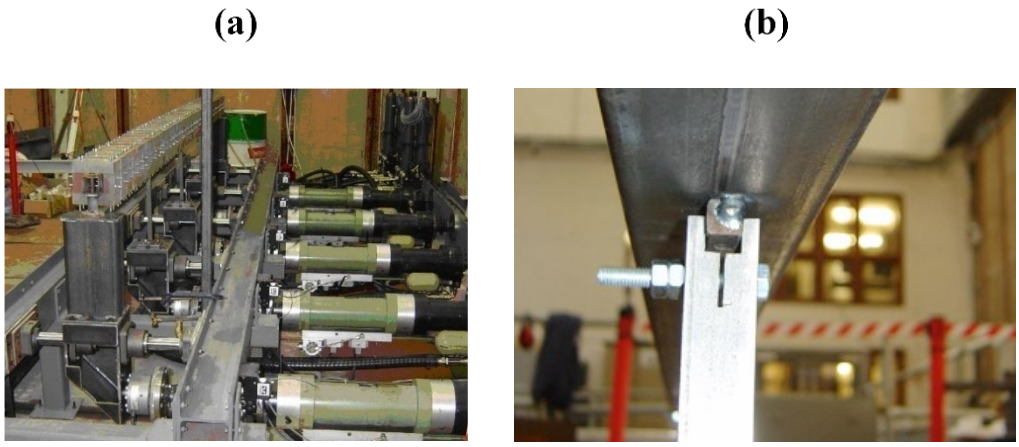

Figure 11; (a) The five, single axis, actuators with the bridge model (b) Pier support fixity arrangement

The bridge model was constructed from a 4m, $60 \times 60 \times 3.2$ mm box section. The piers are 420mm long and have a 20×25 mm solid section. The abutments are pinned in the plan

but fixed in elevation. This is achieved by having a smooth/greased sliding bearing. All the bridge components are made from S275 grade steel. 160 added masses were attached to the bridge deck, increasing the mass of the bridge model to 500kg. The masses are attached in groups of four and are isolated from each other so as not to change the flexural properties of the bridge deck. The ground excitations were simulated by use of the five-single axis, actuators, see Figure 11(a). Each actuator is mounted on a pair of bearings, which move over a single steel shaft. The shaft is attached at each end to a stiff frame. The beam is connected to the piers with a semi-rigid connection shown in Figure 11(b). The bolted connection provides a negligible moment restraint. For further performance specifications, see (Norman et al., 2006).

5.3.2 Numerical model of the physical test bridge

The generalized mathematical model shown in Figure 12 is adapted for the specific case of the benchmark 4 span bridge shown in Figure 12. Our aim here is to derive the simplest, most computationally efficient, reduced-order model. This bridge has four equal spans L and is of total length $4L$. To explore the influence effect of the number of DOF m on the system accuracy we consider two cases:

i. Using $m = s = 5$ resulting in a 3-DOFs reduced-order model. In this case, only the displacements at the top of piers are included.

ii. Using $m = 9, s = 5$, which results in a 7-DOFs reduced-order model. In this case displacements at the top of piers and at the mid-span of beams are included.

Figure 12 displays graphically the bridge. The beam DOFs shown in black are associated with the 3-DOFs system (i) and those in blue are the DOFs for case (ii) the 7-DOFs system.

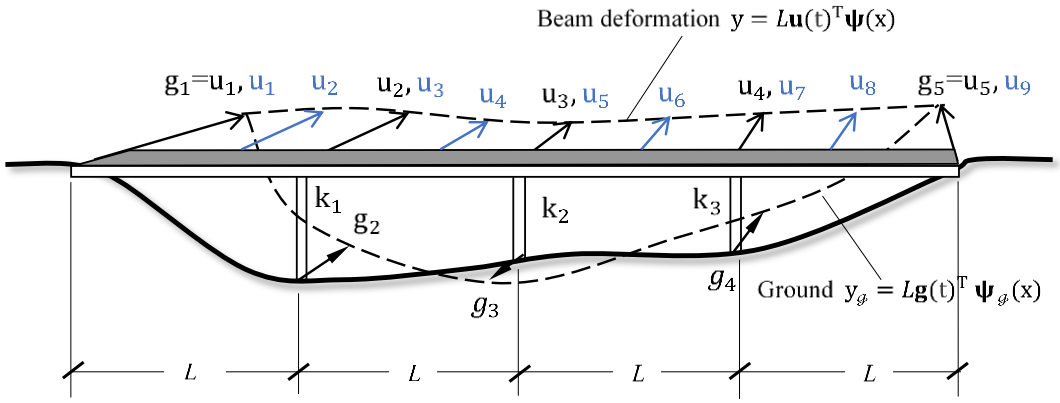

Figure 12; A four-span continuous-beam on three flexible supports

Note that the beam degrees of freedom at the edge supports ($u_{d,1}, u_{d,5}$) for the 3-DOFs system and ($u_{d,1}, u_{d,9}$) for the 7-DOFs system are restrained completely. Therefore, those displacements are equal to the ground displacements at these points. The details of the dynamic system block of the studied bridge model for the 3-DOFs and 7-DOFs system can be found in Appendix B and Appendix C respectively.

5.3.3 Estimation of linear model parameters from experimental responses

The MIMO optimization of the 3-DOFs and 7-DOFs models (equations) are performed for both free vibration and forced (MSE) vibration cases. The part of the time-series after the end of the seismic ground excitation is used for the free vibration case. For this problem, the parameter vector θ is defined as follows:

$$\boldsymbol{\theta} = \left[\gamma_1, \gamma_2, \varpi, \eta_1, \eta_2, \eta_3\right]^T \tag{5.4}$$

Thus, given the recorded inputs and responses we seek the optimal system parameters **θ** that minimize the least square errors in Eq (5.2). In this case, we employ (Matlab system identification toolbox, Grey-Box Model Estimation (Ljung, 1995) that makes use of the

Levenberg–Marquardt algorithm (LMA) (Moré, 1978). For well-behaved mathematical formulations, this LMA is a powerful method to obtaining an optimal solution even if the initial state is selected far away from the final optimum.

The summary of these optimal analyses is shown in Table 2. In this table, the success ratio percentage is used as a goodness-of-fit statistic (Ljung, 1987). This statistic measures the correlation between observed output responses and predicted responses using Eq (2.29) . The finite element results were obtained with Diana FEA package (Norman, 2006, DIANA, 2010). Experimental white-noise tests, at low excitation amplitudes, were performed to estimate the first three modes of vibration using a classical frequency-domain linear input/output inverse system identification (Norman et al., 2006). The performance of the 7-DOFs system shows some slight improvement over the 3-DOFs system in terms of success ratio. That is, overall, for both forced and unforced cases, the 7-DOFs model seems to perform marginally better. However, it should be stated that the reduced-order 3-DOFs system performs remarkably well given that it only contains 3-DOFs. The optimal solution for the 3-DOFs system suggests that the piers have marginally varying stiffnesses, which should not have been the case as they are constructed with identical geometries and materials. Although it was difficult to estimate experimentally the fixity of the top of the piers (shown in Figure 13b) precisely. The 7-DOFs optimal solution suggests that these piers are identical. Does the 7-DOFs system overfit the test results predicting equal pier stiffnesses and/or is the 3-DOFs model too simple to completely capture the higher modal behavior? Without recourse to the physical specimen and further tests, it is not clear which of 7-DOFs or 3-DOFs systems are truer to reality. However, the main aim here is to confirm the robustness and fidelity of the reduced-order models, therefore this discussion is not critical for this study.

The equivalent viscous damping for this experimental model was very low as shown in Table 2. An interesting result that emerges from the MIMO optimal analyses is that there is significantly more damping under forced vibrations than there is under free (unforced) vibrations. This suggests that there is an amplitude-dependent frictional mechanism active in this physical model. Figure 13 shows, graphically, a comparison of the model-updated numerical solution to the system in Eq (5.1) with the experimentally recorded results. This figure compares the displacement time-histories at the top of the central column for both 3-Dof and 7-Dof systems in the alignment C00-I03. More results are represented in Appendix D for other alignments. For both these numerical models' time-histories match the experimental model extremely well; this confirms that the low order system is a reasonable model of a multi-support excited multi-span bridge.

Table 2; Comparison of MIMO optimal dynamical parameters and system frequency estimates

	(Norman 2006)		Forced System		Unforced System	
	FEA	Exp.	3-Dof	7-Dof	3-Dof	7-Dof
Success ratio	-	-	88.34%	92.37%	96.65%	97.3%
ϖ [rad/s]	-	-	18.5	18.53	18.33	18.3
η_1	-	-	3.2	3.12	3.5	3.5
η_2	-	-	3.1	3.12	3.3	3.5
η_3	-	-	3.2	3.12	3.2	3.5
γ_1	0.05	0.05	0.0103	0.010	0.0042	0.004
γ_2	0.05	-	0.0202	0.0145	0.003	0.003
f_1[Hz]	5.38	5.39	5.53	5.52	5.62	5.75
f_2 [Hz]	9.14	10.15	10.53	8.95	10.49	9.03
f_3 [Hz]	16.8	16.31	24.6	17.17	24.37	17.08

Align.3

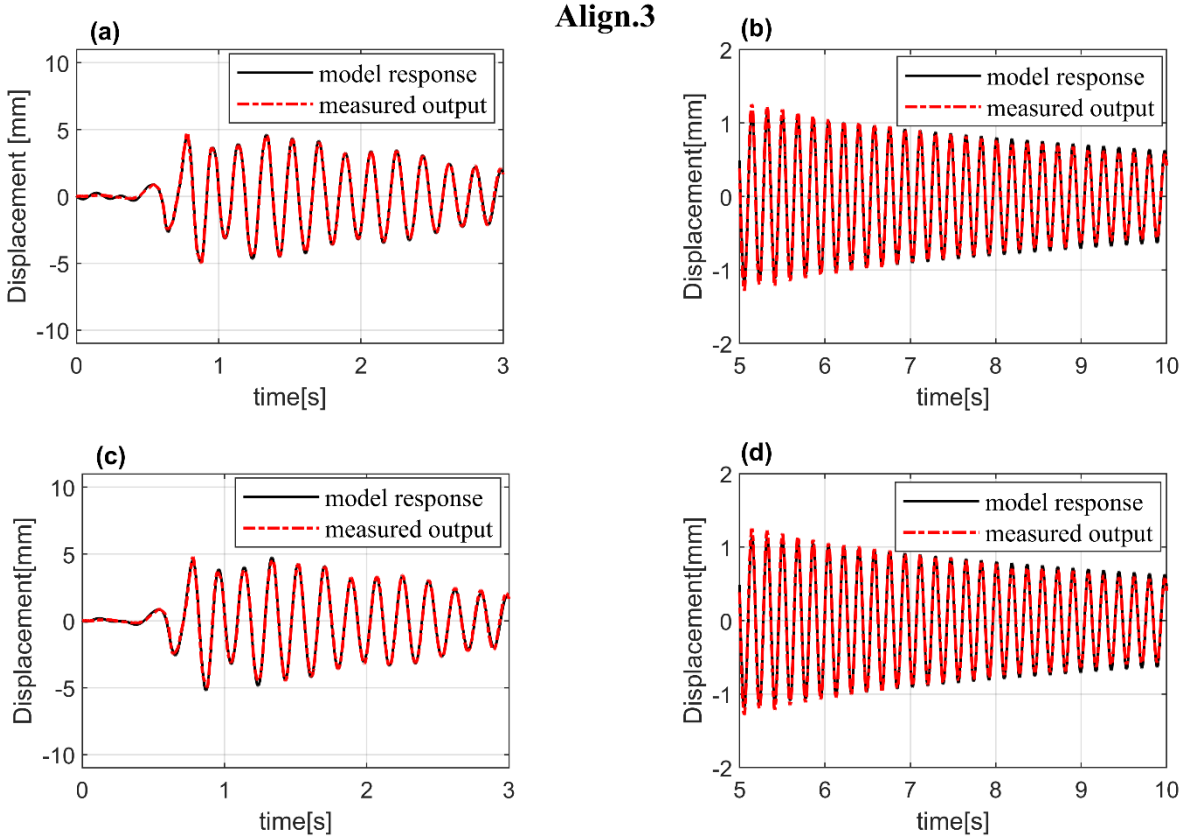

Figure 13; Result of curve fitting of experimental bridge model, alignment C00-I03. (a) 7-Dof system under multi-support excitation, (b) 7-Dof system under free-vibration, (c) 3-Dof system under multi-support excitation, and (d) 3-Dof system under free-vibration.

Figure 14 displays the Spectral-density function of system identification results for both 7-DOFs and 3-DOFs systems. The power-spectrum is obtained using the P-Welch method (Welch, 1967). As it can be seen from forced-system results, the 7-DOFs model calibrates more frequency contents in the low-frequency range from 0 to 16 Hz. In the duration of free vibration, there is no substantial difference between the 7-DOFs and 5-DOFs model results. It again shows greater sensitivity of the proposed dynamic system to forced vibrations.

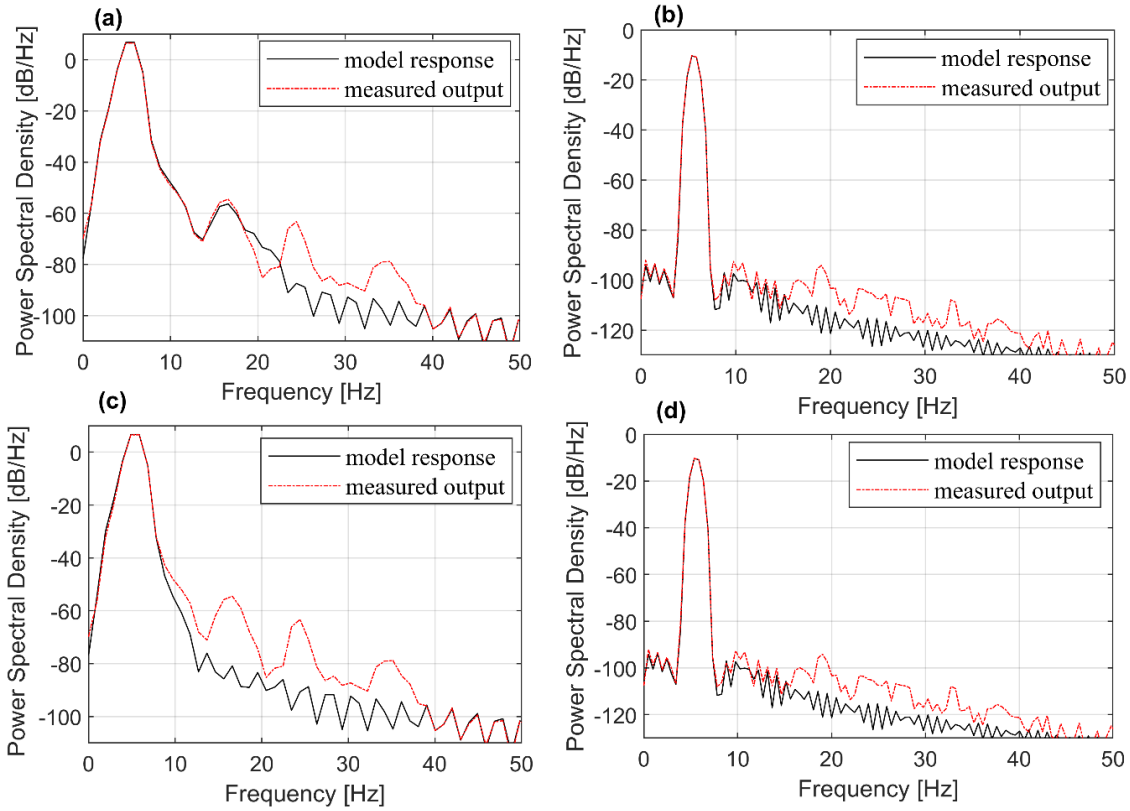

Figure 14; Welsh PSD estimate of curve fitting result of experimental bridge model, alignment C00-I03. (a) 7-Dof system under multi-support excitation, (b) 7-Dof system under free-vibration, (c) 3-Dof system under multi-support excitation, and (d) 3-Dof system under free-vibration.

5.4 EVALUATION OF NONLINEAR BRIDGE SYSTEM

The proposed mathematical model of a nonlinear dynamic system Eq (3.32) will be benchmarked. The displacement time-series data from Experimental bridge tests from previous section 5.3.3 has been used to validate the proposed dynamic system. The dynamic response quantities of the bridge experiment are limited to the linear region, therefore the linear version of the proposed analytical model is compared with experimental data. An accurate calibration of a hysteresis loop with the experimental data has been established for a single column in recent studies (Kunnath et al., 1997, Ning et al., 2019). The Bouc-Wen parameters implemented in our reduced-order system (Eq(3.15)

to Eq(3.18)) lie within the range previously reported in these recent studies.

From all Bouc-Wen parameters that can be chosen suitably from the recommended range, yielding displacement should be estimated from the pier dimension (see Section 3.2.5). As the experimental piers do not have the real dimension and the experimental bridge was designed to be excited in the elastic region only, therefore the yielding displacement for all three piers is assumed to be 6 mm which enforces the dynamic nonlinear system behaves linearly. The response quantity of interest is obtained by solving the first-order state-space form of the dynamic system. The example of the representation of nonlinear differential equations of motion in the state-space form of the 3-DOFs system is shown for the prototype bridge in Appendix E. The ODE solver (ode45 in Matlab) was employed. The dynamical linear model of the bridge system is obtained from Eq (3.32) where α is taken equal to 1. The scaled maximum of the PGA of 0.023g is employed at stations. Figure 15 confirms that the experimental results were accurately simulated by the linear space-state form (where $\alpha=1$) of the proposed analytical model. The full nonlinear equations (where $\alpha=0.05$) results in solutions that exhibit a small amount of ductility during the high amplitude part of the earthquake as expected. Thus, we conclude that the Eq (3.17) and (3.32) are reasonable.

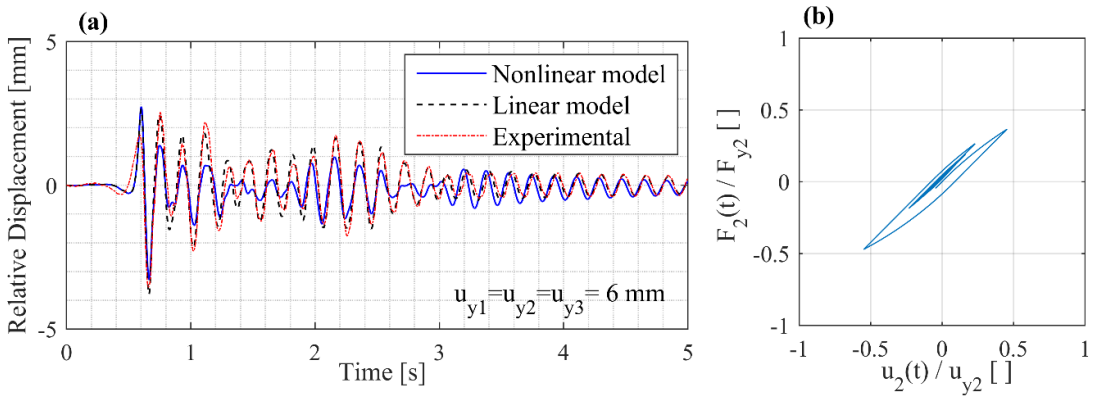

Figure 15 ;(a) evaluation of dynamic nonlinear and linear system by Benchmark experimental test data; (b) force-deformation curve of proposed Bouc-Wen inelastic model for the linear experimental bridge. PGA=0.023g.

5.5 SUMMARY

In this chapter, the proposed reduced-order model has been recast in form of a linear State-space framework. It makes use of a Multi-input Multi-output (MIMO) system formulation to simulate the dynamic behavior of multi-span bridges. The system identification of 3-DOFs and 7-DOFs models has been established for both free-vibration and forced vibration systems.

The summary of the optimal analyses suggests that 7-DOFs model seems to simulate the bridge behavior slightly better. It can be suggested from the Spectral-density function of optimization results as well, The 7-DOFs forced system can capture more frequency contents in the range of low-frequency.

Finally, The non-elastic time-history model has been evaluated using the same experimental framework. Bouc-Wen parameters have been chosen in a suitable range to get the linear version of the proposed dynamic model. Although piers exhibit a slight hysteresis, the proposed non-linear model simulated experimental results accurately in the linear region.

5.6 NOMENCLATURE

Dimensions in the following list are force [F], length [L], and time [T] with non-dimensional angles defined in Radians [Rad] and other dimensionless quantities defined by [ ].

$\mathbf{A}(\boldsymbol{\theta}), \mathbf{B}(\boldsymbol{\theta}), \mathbf{C}(\boldsymbol{\theta}), \mathbf{D}(\boldsymbol{\theta})$	State-space system matrices []
$\mathbf{C}_{11}, \mathbf{C}_{12}, \mathbf{C}_{22}$	Non-dimensional damping block matrices []
EI_z	Deck flexural rigidity (about *z*-axis) [F][L]^2
f_i	i^{th} modal frequency [T]$^{-1}$
$\mathbf{f}(\tau)$	system input [L]
g_i	i^{th} ground DOFs [L]
k_i	Pier transversal flexural stiffness [F][L]$^{-1}$
$\mathbf{K}_{11}, \mathbf{K}_{12}, \mathbf{K}_{22}$	Non-dimensional block deck stiffness matrices []
m_b	Deck mass per unit length [F][T]^2[L]$^{-2}$
m	Number of deck DOFs []
$\mathbf{M}_{11}, \mathbf{M}_{12}, \mathbf{M}_{22}$	Non-dimensional deck block mass matrix []
$\mathbf{N}_a$	Non-dimensional influence matrix []
PGA	Peak ground acceleration [L] [T]$^{-2}$
s	Number of supports []
$\mathrm{u}_{d,i}$	i^{th} Bridge deck DOF (including free and constrained DOFs) [L]
u_{yi}	yield displacement of i$^{\text{th}}$ pier [L]
$\mathbf{u}_d$	Bridge deck DOF vector (including free and constrained DOFs) [L]
$\mathbf{u}_g$	Ground DOF vector [L]

$\mathbf{w}$	Deck displacement DOFs (including only free DOFs) []
$\mathbf{x}(\tau)$	the state vector of deck DOFs [L]
$\mathbf{y}(\tau)$	observed output [L]
α	post- to pre-yield stiffness ratio; []
γ_i	i^{th} modal damping ratio []
η_i	i^{th} pier to deck stiffness ratio []
$\boldsymbol{\theta}$	Optimal argument parameter vector []
ϖ	System frequency parameter [Rad][T]$^{-1}$

Chapter 6

Parametric Analysis Scheme for The Linear Bridge System

The contents of this chapter have been partially adapted from the study (Meibodi et al., 2020, Meibodi and Alexander, 2021) that published in:

MEIBODI, A. A. & ALEXANDER, N. A. 2021. Spatiotemporal seismic excitation of bridges with an anti-symmetrical first mode. *Bulletin of Earthquake Engineering*.

MEIBODI, A. A., ALEXANDER, N. A., NORMAN, J. A. & CREWE, A. J. 2020. A theoretical and experimental exploration of the seismic dynamics of multi-span bridges. *Bulletin of Earthquake Engineering*.

6.1 INTRODUCTION

In this chapter, we aim to provide insight into the utility of *geometry only* parameters, the auto-modal participation (AMP) factor $A_{u,i}$, and cross-modal participation (CMP) factor $B_{u,i}$ we seek to compare ISE and MSE analyses. The main scientific question is to explore what factors make it more likely that ISE analyses will be non-conservative?

Therefore, herein, we attempt to find a correlation between bridge geometry parameters and the error between MSE and ISE analyses and find critical bridge configurations where this error is substantial.

6.2 CASE STUDY

The Reference bridge studied in (Lupoi et al., 2005, Crewe and Norman, 2006, Alexander et al., 2006) is chosen to illustrate the proposed model. The benchmark experimental model (1:50 scale) of this bridge was constructed in the laboratory (University of Bristol). The Bridge contains a continuous deck integral supported on three cantilever piers with an equal height of 10m. The total length bridge is 200m with four equal spans (Figure 16). The system identification of the experimental model was performed in section 5.3.3. The damping ratio of the first and second modes are assumed equal to 0.05 in the Rayleigh damping Eq(2.22)

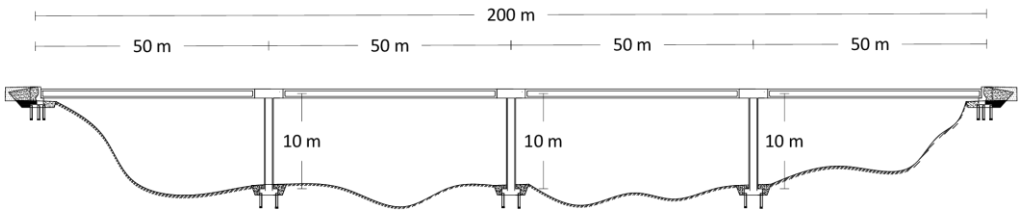

Figure 16; configuration and arrangement of studied prototype bridge.

6.2.1 Estimating reasonable parameter values

The key numerical parameters in Eq (2.29) are (i) system frequency parameter ϖ and (ii) the pier to deck stiffness ratios η_i. In the experiment campaign, we have determined by simplified experimental inverse system identification the values for these parameters. In this section, we aim to choose parameter values that are appropriate for real bridge structures. In the study, (Dusseau and Dubaisi, 1993) measured the vertical and lateral fundamental frequencies for a set of concrete bridges in the Pacific Northwest, USA. Data collected from this paper is used to propose a new empirical formula for generic concrete bridges:

$$f_1 = \frac{996.3}{L_t^{1.19} H^{0.194}} \tag{6.1}$$

where f_1 [Hz] is the fundamental lateral frequency, L_t [m] is the total length of the bridge and H [m] is the maximum pier height. Figure 17 (a) displays the experimental data collected by Dusseau and Dubaisi (Dusseau and Dubaisi, 1993) and the empirical formula Eq (6.1). The empirical fit was obtained by using Matlab curve fitting toolbox and had an $R^2 = 0.96$.

Figure 17 (b) displays the fundamental lateral frequency from the reduced-order model, Eq (6.1). At $\varpi = 18.5$ [rad/s] and pier to deck stiffness ratio, $\eta = 3.5$ the natural

frequency is about $f_1 = 6$ [Hz]. The 200m long prototype structure, that was used to design the experimental model bridge, should have a frequency in the range of 0.43 to 2.7 [Hz] (from Eq (6.1)). This analysis suggests that the experimental model was a little stiffer than ideal if the aim was to parametrically match this prototype. A more reasonable value of ϖ would be about $\varpi = 5$ [rad/s], if we are to place the parametric analysis within the scope of real structures. Therefore, we shall adopt $\varpi = 5$ [rad/s] for the subsequent parametric studies.

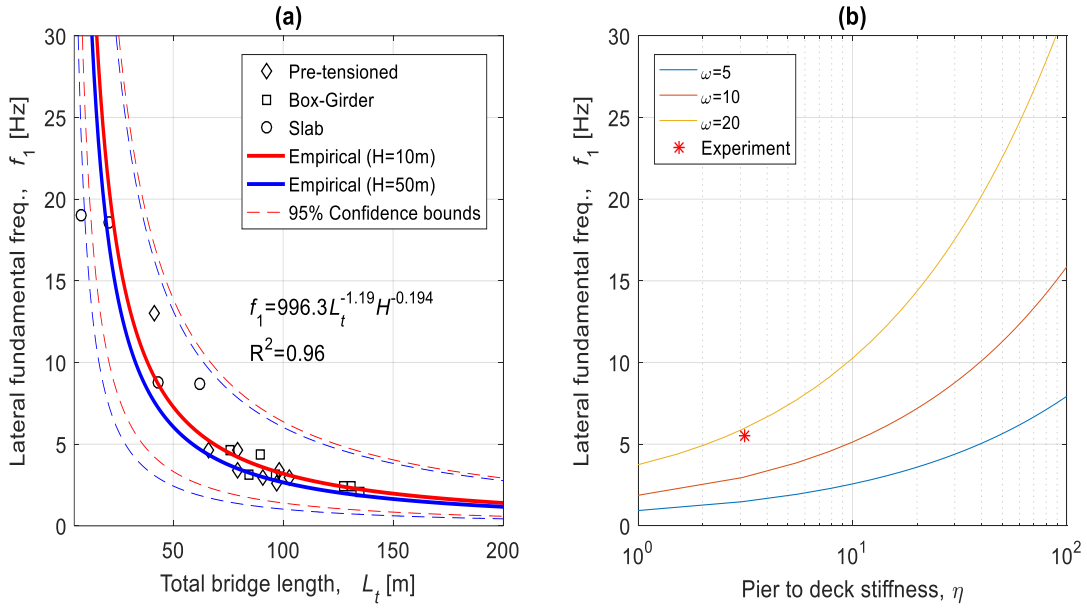

Figure 17; (a) Experimental lateral frequencies vs total bridge length for Concrete Bridges in the Pacific Northwest, USA (Dusseau and Dubaisi, 1993) (b) Theoretical lateral frequencies vs pier to deck stiffness ratio from Eq(2.29) with equal piers $\eta_2 = \eta_3 = \eta_4 = \eta$

6.3 PARAMETRICALLY EXPLORATION OF VALLEY PROFILE.

Figure 18 displays the general form of an archetypal symmetrical multi-span bridge model. To get various bridge configurations with different dynamic properties, it was assumed that the profile of the valley varies so that bridge arrangement remains

symmetrical. Therefore, in order to provide simplification to present spatial variation effect in the parametric study, we introduced the following system parameters:

$$\alpha = \eta_3 / \eta_2 , \qquad \eta = \eta_2 = \eta_4 \tag{6.2}$$

Where α is a ratio of stiffness between the central and outer pier and η is the deck to pier stiffness ratios for outer piers which are calculated for our bridge system in Eq (2.12) .

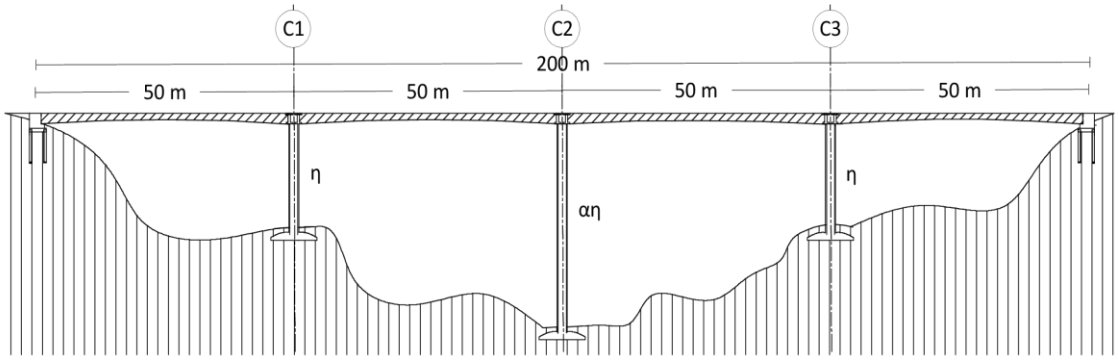

Figure 18; symmetrical bridge arrangement for parametric study

A shorter central column would result in a stiffer column, hence $\alpha > 1$. The suggestion here is that when the central column is stiff enough the fundamental mode must become anti-symmetric about the central pier. This is a key feature of the parametric analyses in this section. Archetypally symmetrical (in geometry) bridges need not have symmetrical first modes of vibration. In this case, when α is large, the first mode is anti-symmetrical. This may induce larger differences between MSE and ISE analyses for larger α.

Figure 19 demonstrates how the parameters (η, α) can define different configurations, both deep and shallow valleys and ones with and without a central rise.

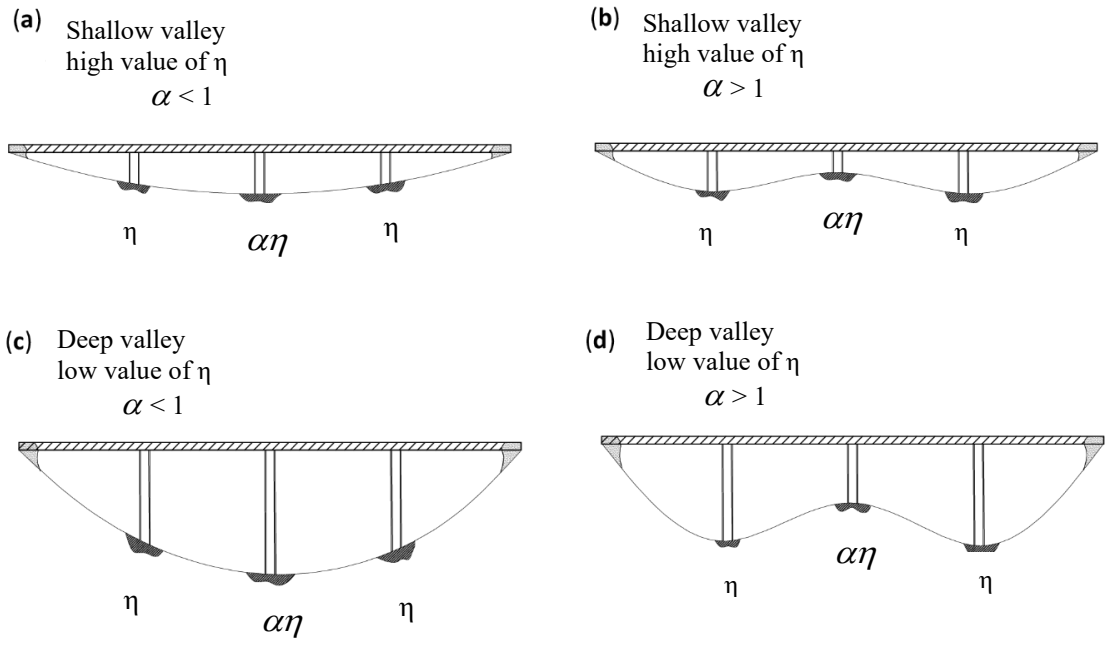

Figure 19; Different bridge configuration (a) a shallow valley with the high value η and $\alpha<1$, (b) a shallow valley including a raise in the middle with a high value η and $\alpha<1$, (c) deep valley with the low value η and $\alpha<1$, (d) deep valley including a raise in middle with the low value η and $\alpha<1$.

6.4 NATURAL VIBRATIONS OF A STUDIED BRIDGES

The natural frequencies and mode shapes for the 7-DOFs system are calculated from Eq (2.29). This eigenvalue problem for natural vibrations for this system is $(\mathbf{D} - \omega_i^2\mathbf{I})\boldsymbol{\phi}_i = 0$. The dynamic matrix **D** is equal to $\mathbf{M}_{11}^{-1}\mathbf{K}_{11}$. In general, **D** is a function of four system parameters (pier-to-deck stiffness ratios η_1, η_2, η_3 for the 1st to 3th pier respectively and frequency parameter ϖ).

A graphical representation of these eigen solutions is shown in Figure 20 for bridges in the parametric study. Notations S1 and S2 represent the first and second symmetric modes while A1 and A2 represent the first and second anti-symmetric modes. Figure 20 (a) shows the variation of modal circular frequencies ω_i with pier-to-deck stiffness ratio η. In this case α=1, thus all three support piers are identical.

At low values of η, this would be for long slender piers, the natural frequencies of transversal horizontal modes are well separated. However, at the larger values of η (on this graph), this would be for shorter stockier piers, the natural frequencies are not so well separated. The first and second modes cross (are equal in frequency) at $\eta = 110.1$ (in Figure 20(a)). Consider, also, the changes in mode shapes that are displayed in Figure 20 (a). For low values $\eta < 110$, as modes are well-separated, the first mode is always symmetrical. However, with $\eta > 110$, the first mode is now always anti-symmetrical. Therefore, this raises the question, will spatially incoherent ground motions (MSE) be more problematic by exciting this anti-symmetrical first mode?

Consider now another case where $\alpha = 3$ (Figure 20(b)) implying the central pier has triple the transversal flexural stiffness of the first and third piers. This could be due to a larger flexural rigidity, a shorter pier height, and/or stiffer foundations. The first and second eigen solutions, for $\alpha = 1$, only intersect at $\eta \approx 110$ as shown in Figure 20 (a). This is not the case where $\alpha = 3$. The first two eigensolutions intersected and cross at $\eta \approx 7$ and again at $\eta \approx 75$ and $\eta \approx 110$. Between the first two intersections, for $7 < \eta < 75$, the first mode is anti-symmetrical. Continuing the argument proposed in the previous paragraph it is likely that analysis of a bridge, for $7 < \eta < 75$ and $110 < \eta$, the ISE analysis case will not be able to excite the first mode that is anti-symmetrical.

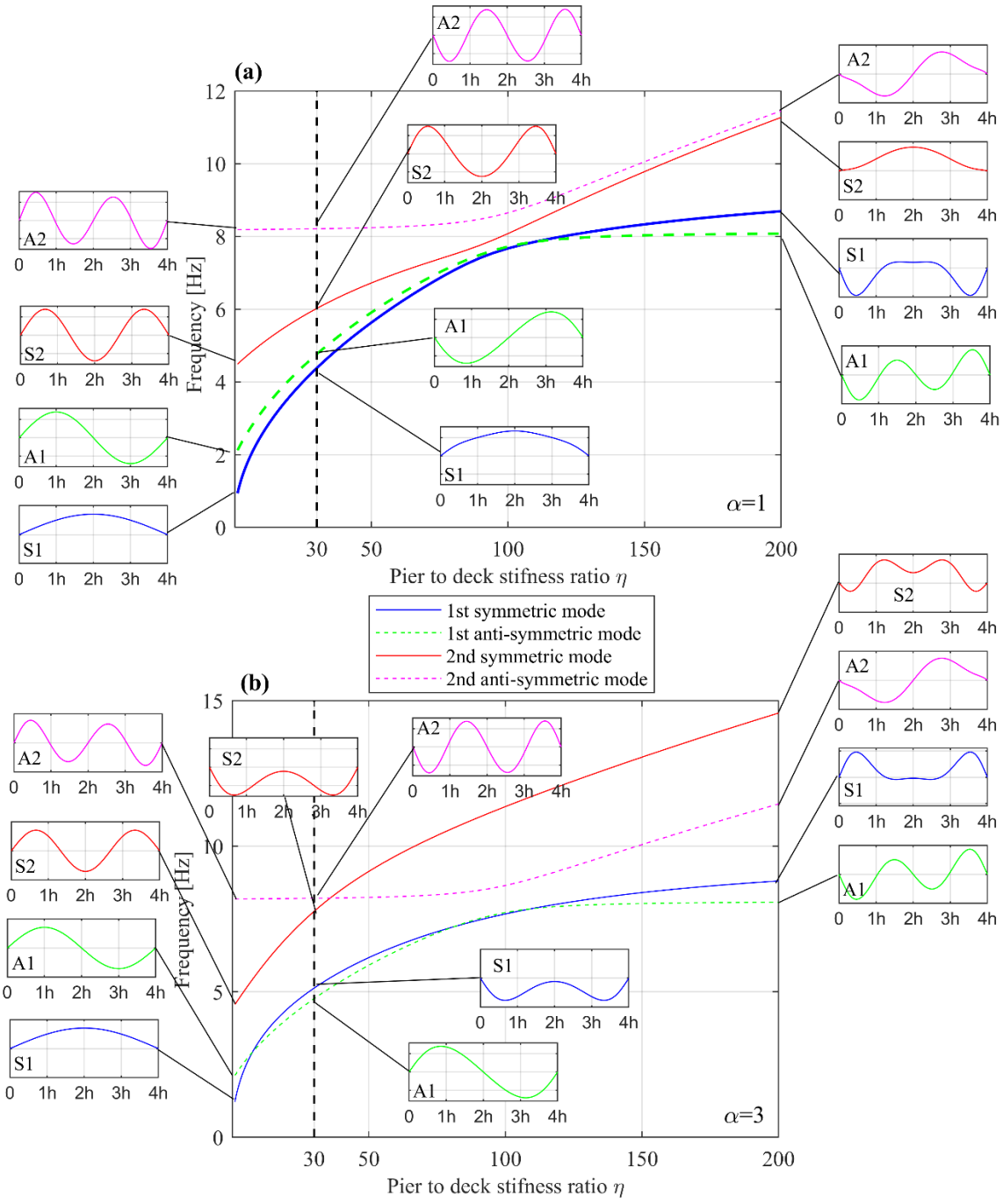

Figure 20; Variation of modal frequencies and mode shapes with structural geometry (a) α=1 (b) α=3

The locus of the frequency intersection points of the first symmetric and anti-symmetric modal frequencies is displayed in Figure 21. In this figure, ω_s and ω_A denote the first circular frequency of symmetrical and anti-symmetrical modes respectively. The red lines correspond to the cases in Figure 20.

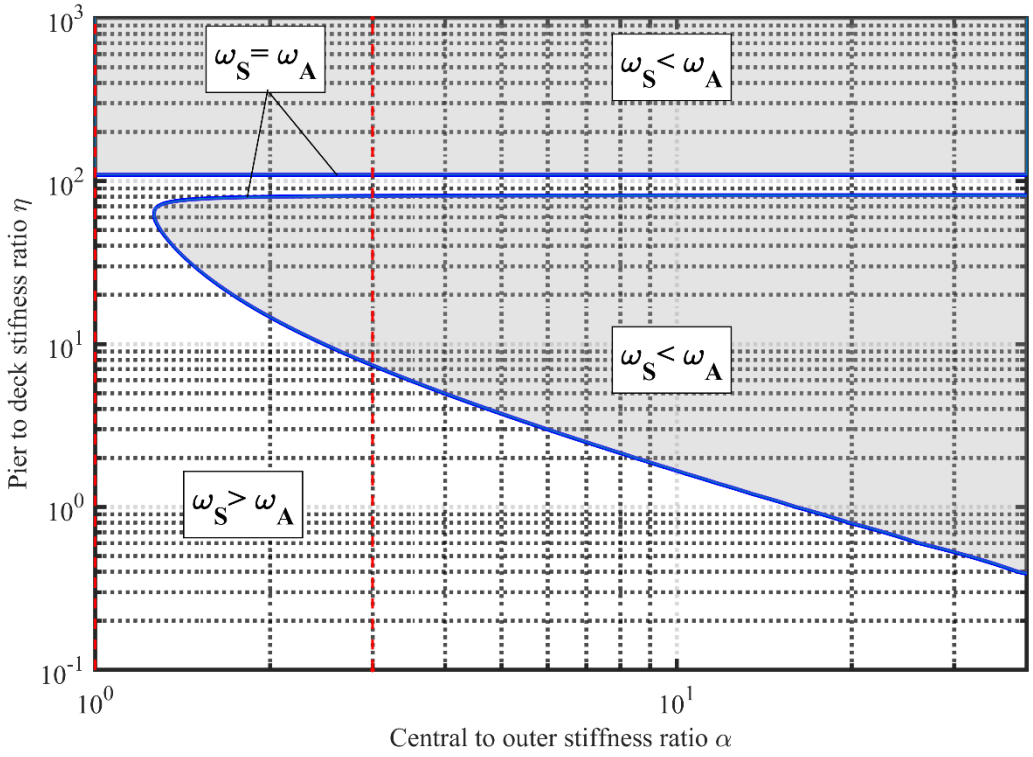

Figure 21; locus of frequencies where first symmetric and anti-symmetric modes are equal.

$\boldsymbol{\omega_s}$ and $\boldsymbol{\omega_A}$ denote the first circular frequency of symmetric and anti-symmetric mode respectively. For a case where $\eta > 109$, the first mode is anti-symmetrical for all values of α. When $\alpha > 1.26$ and $\eta < 109$ then there exist values of η such that the first mode is anti-symmetrical. While for $\alpha < 1.26$ and $\eta < 109$ there exists no region in which this first mode is anti-symmetrical. Thus, increasing the height of the central pier, relative to the other piers, will reduce its stiffness and hence reduce α below 1 and tend to increase the separation of the symmetrical and anti-symmetrical modal frequencies; with the first symmetrical mode always being the fundamental mode.

6.5 THE RELATIONSHIP BETWEEN MODAL PARTICIPATION FACTORS AND MODE SHAPES

The pattern of dynamic response in the frequency-domain is strongly dependent on the behavior of the participation factor $\mathbf{\Gamma}_i$ ((where $\mathbf{\Gamma}_i^T(\omega) = \boldsymbol{\phi}_i^T \mathbf{N}_a = [\Gamma_{i1}, \cdots, \Gamma_{is}] \in \mathbb{R}^{1\times s}$). Similarly, the mode shape of vibration excitation mainly determines the response pattern in the time-domain. Hence, it is hypothetically and physically justified that participation factor and mode shape exhibit a similar trend and behavior. To examine their correlation, let us consider that the stiffness of piers η of prototype bridge (α=1) varies from 1 to 200 as shown in Figure 20. S1 and A1 denote the first symmetric and anti-symmetric modes respectively. Let's consider the symmetrical mode with the low values of η (in Figure 22, the case with η=0.1). The values of Γ_i at abutment (constraint) are substantially higher than corresponding values at the middle piers, although the mode shape behaves the other way around. As the η increase, the trend of Γi become more similar to shape mode (cases with η=100,200). Despite these differences, both mode shape, and Γi exhibits the same behavior in terms of anti-symmetric and symmetric configuration. In this study, the mode shape is used to classify the behavior of the studied bridge.

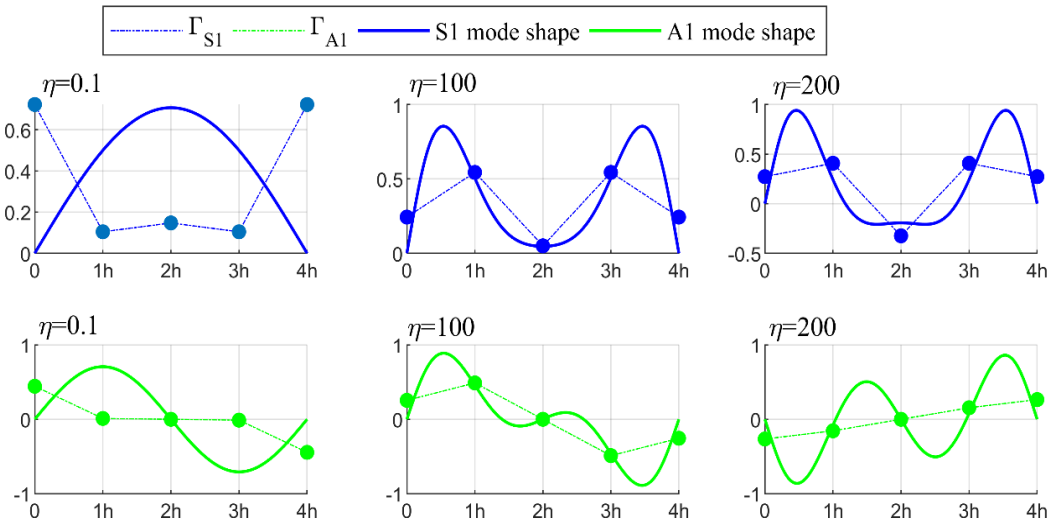

Figure 22; The correlation of participation factors Γ_i and mode shape for first symmetric and anti-symmetric mode.

6.6 BOUNDING ANALYSIS

Previously, in Chapter 2, we defined *geometry only* parameters, the auto-modal participation (AMP) factor $A_{u,i}$, and the cross-modal participation (CMP) factor $B_{u,i}$. These helped to define bounds on the error between MSE and ISE analyses, see Eq (2.49) . To explore their effect, let's consider the (CMP) factor of the pier (C1) for the first mode $B_{2,1}$ and the second mode $B_{2,2}$ (note that the suffix numbering for $B_{u,i}$ is for the u^{th} DOF, and i^{th} mode), Figure 23 depicts the CMP factor ($B_{2,1}$ and $B_{2,2}$) for the bridge with various dynamic parameters α and η. It is entirely consistent with the locus plot in Figure 21.

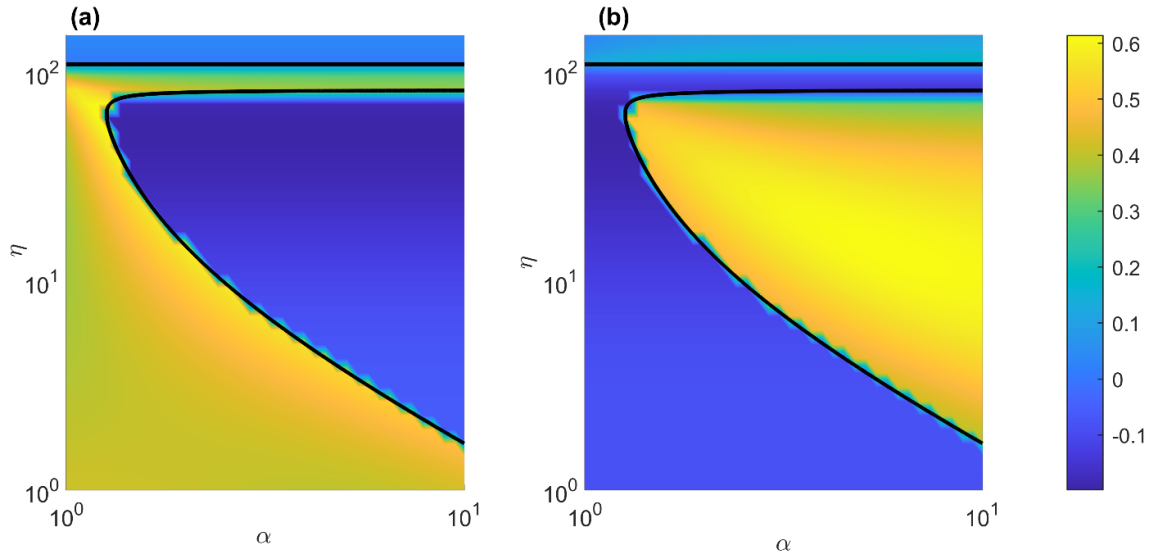

Figure 23; CMP factor for the studied bridge with various dynamic parameters α and η at outer Pier C1 (a) First mode cross-modal participation (CMP) $B_{2,1}$ (b) Second mode cross model participation (CMP) $B_{2,2}$.

The area with positive values represents the cases where the mode shape is symmetrical. Contrarily, the region with negative values shows that the mode shape is anti-symmetrical. In these regions, only MSE ground motion input can properly excite this mode. To explore the modal response of anti-symmetric mode excited by ISE excitation, Let's consider, an anti-symmetrical modal response from Eq (2.34) and Eq (2.40):

$$\left(q_i\right)_{ISE} = h_i R e^{i\theta}\left(\sum_{j=1}^{s} \Gamma_{ij}\right) \tag{6.3}$$

For anti-symmetric mode, $\sum_{j=1}^{s} \Gamma_{ij}$ is equal to zero. Hence, an anti-symmetrical modal response under ISE excitation is zero. It has been concluded in different studies including Zerva and Zervas (2002). Therefore, it seems that bridge cases in the area with a first anti-symmetrical mode, would be excited considerably by MSE seismic input and they cannot be excited by ISE inputs.

While Figure 23 uses the conventional mode numbering (ranked in ascending frequency) it is also instructive to number the modes by their characteristics, i.e. symmetrical and anti-symmetrical. Therefore, exploring the value of AMP and CMP factors for Pier (C1) in Figure 24 and Figure 25 respectively reveals an interesting result. The values of $A_{2,S1}$ and $B_{2,S1}$ are pronounced where the anti-symmetrical mode is fundamental. This suggests that the effect of the first symmetrical mode (mode 2) may also be significant although the first mode is anti-symmetrical. The values of $A_{2,A1}$ (in Figure 24b) and $B_{2,A1}$ (in Figure 25b) appear surprisingly constant and hence of little utility in distinguishing those regions of geometric parameter space susceptible to significant errors between ISE and MSE analyses. As AMP and CMP represent *geometry only* bound estimates we need to also explore what happens when we include ground excitation.

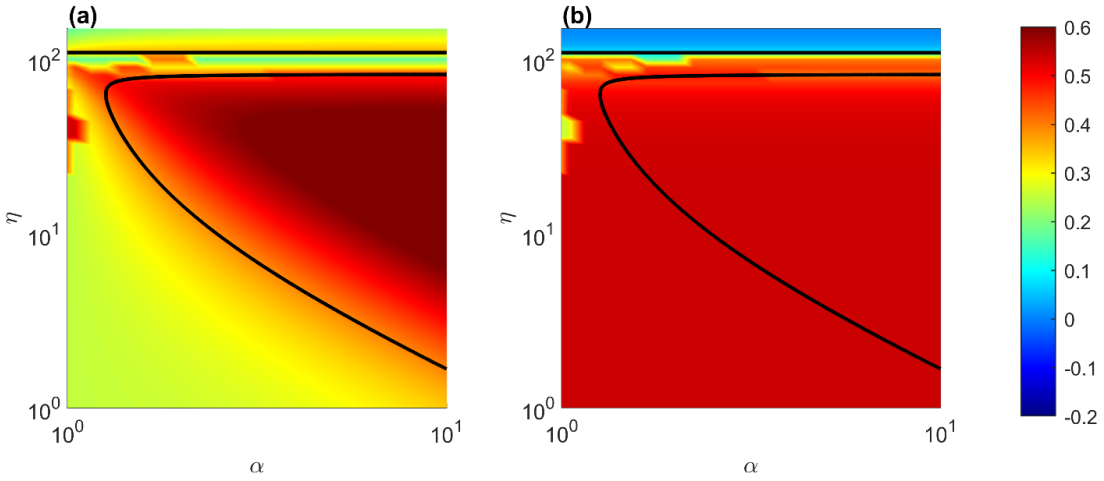

Figure 24; AMP factor for the studied bridge with various dynamic parameters α and η at outer Pier C1 (a) First symmetrical mode's Auto Modal Participation$A_{2,S1}$ (b) First anti-symmetrical mode's Auto Modal Participation$A_{2,A1}$.

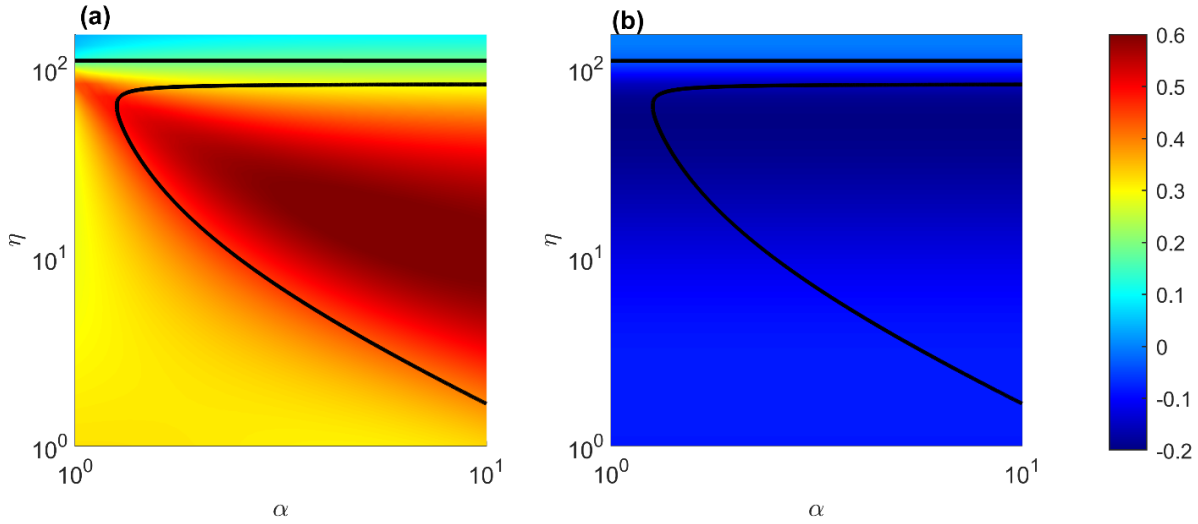

Figure 25; CMP factor for the studied bridge with various dynamic parameters α and η at outer Pier C1 (a) First symmetrical modes' cross model participation (CMP) B2, S1 (b) First anti-symmetrical mode's cross model participation (CMP) B2, A1.

6.7 DYNAMICAL ANALYSIS INCLUDING BOTH GEOMETRY AND LOADING

In the previous sections 6.4 (modal analysis) and 6.6 (bounding analysis), we suggest a hypothesis that in the region where the first mode is anti-symmetrical there may be greater errors between MSE and ISE. Numerical analysis that includes explicitly ground excitation is necessary to confirm these suggestions. Therefore, this section explores the validity of the above observations by comparing with numerical analysis of the heuristic bridge when subjected to real ground motion excitations from the SMART-1 Array. To quantify dynamic responses in the frequency domain, the 'mean-squared' dynamic response of the u^{th} DOF of the structure is defined as (Zerva, 1990):

$$\sigma_u^2 = \int_{-\infty}^{+\infty} S_{uu}(\omega)\mathrm{d}\omega \tag{6.4}$$

where $S_{uu}(\omega)$ is the power spectrum of the responses of the u^{th} DOF and is defined from the total response solution in Eq (2.42).

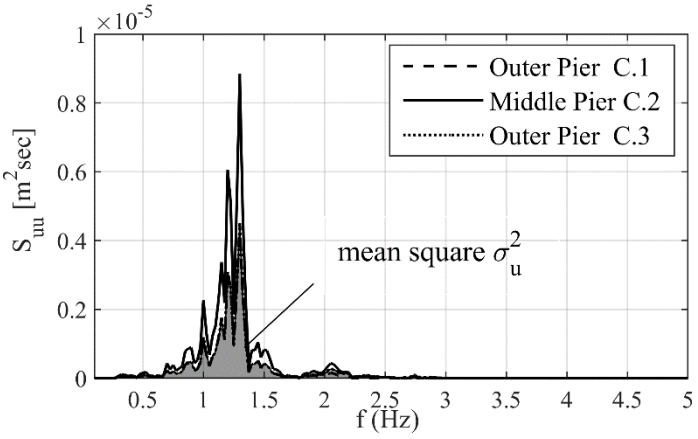

Figure 26; illustration of PSD of dynamic response and mean square σ_u^2 of Pier3 for reference bridge with dynamic parameters $\eta = 2.4, \alpha = 1$ .Performance measures

To make a direct comparison we compare the responses of a bridge when analysed using ISE and then using MSE. Hence, we proposed the following simple performance measures:

$$\chi_u(\eta,\alpha,j) = 100\left\{\frac{\left(\sigma_u^2\right)_{MSE} - \left(\sigma_u^2\right)_{ISE}}{\left(\sigma_u^2\right)_{ISE}}\right\} \tag{6.5}$$

Where dynamic error, $\chi_u(\eta,\alpha,j)$ is the difference (percentage error) in dynamic response between MSE and ISE cases for specific values of parameters α and η. The number $1 \le j \le 12$ determines the bridge orientation. The MSE simulations make use of real spatiotemporal SMART-1 array ground excitation for event 43. In this case, abutments and pier supports have different ground excitation time-series. The ISE simulations employed the ground motion from the central station I00 applied (at the appropriate rotation angle) to the supports of abutments and piers. Due to the symmetrical configuration of the bridge, The middle piers (C.2) become the rest point and can be effected only by symmetric mode as is concluded in the study (Price and Eberhard, 1998).

Therefore, we consider the response of the first outer pier (C.1) in this study. The maximum and minimum of the range of χ_u for all bridge orientation are defined as:

$$\min_{\forall j}\{\chi_u\} \le \chi_u \le \max_{\forall j}\{\chi_u\} \tag{6.6}$$

The negative of these ranges identifies the cases where ISE is conservative. The positive of these ranges identify the cases where ISE is non-conservative.

The contribution of ith mode to the dynamic error can be calculated from modal analysis errors as follow:

$$\chi_{u,i} = 100\frac{\int_{-\infty}^{+\infty}\varepsilon_{u,i}(\omega)\,\mathrm{d}\omega}{\left(\sigma_u^2\right)_{ISE}} \tag{6.7}$$

Similarly, the cross-modal contribution of mode i and j to the dynamic error can be expressed as:

$$\chi_{u,ij} = 100\frac{\int_{-\infty}^{+\infty}\varepsilon_{u,ij}(\omega)\,\mathrm{d}\omega}{\left(\sigma_u^2\right)_{ISE}} \tag{6.8}$$

6.7.1 Dynamic error of total response

Figure 27 shows the dynamic error range for various parameters α and η. This plot represents tens of thousands of different parametric/ground excitation configurations and their numerical solutions. Note that varying both parameters α and η conceptually allows us to explore both deep valleys (high values of η) and shallow valleys (low values of η). In addition values of α greater than 1 start to introduce a central rise profile in the valley.

This is compared with the proposed analytical curves from the previous sections, Figure 21 (modal analysis) and Figure 24 Figure 25 (bounding analysis). The results suggest that for each bridge configuration with a specific set of geometric parameters α and η, it is conceivable to find an input motion combination that the ISE case is either conservative (down to -20%) or non-conservative (up to 40%). Figure 27 shows a close correlation between numerical results (geometry and forcing) and the analytical results (Figure 21 based on geometry alone). Therefore, it appears possible to identify some regions where MSE and ISE analyses could produce very different results based on geometry alone.

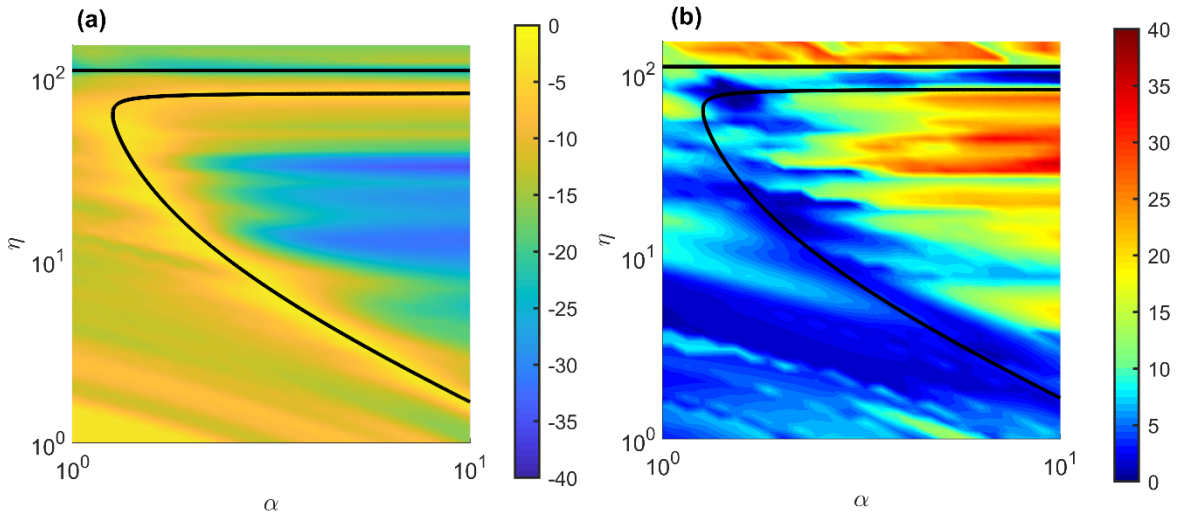

Figure 27; Dynamic error $\chi_p(\eta,\alpha,j)$ (for the top outer pier (C1) in Figure 18) for studied bridges in (a) lower bound error (b) upper bound error.

Thus, results from this dynamic analysis (including geometry and loading) and geometry alone (modal and bounding analyses) appear to show a corroboration if a large enough sample of records is chosen.

This confirms that when the first mode is anti-symmetrical one should avoid just employing ISE analysis. However, the question remains: is this due to the contribution of this anti-symmetrical mode?

6.7.2 Forensic analysis of modal contributions

To explore the effects of certain modes, we expand the dynamic error due to the i^{th} mode $\chi_{u,i}$ in Eq (6.7). Let's consider the modal analysis error $\varepsilon_{u,i}$ introduced in section 2.2.7 for S1

and A1 mode which is normalized by $\left(\sigma_p^2\right)_{ISE}$ in Figure 29 and Figure 30. The area under the curve of modal analysis error in Figure 29 and Figure 30 illustrates the Contribution of ith mode to the percentage error $\chi_{u,i}$. The mathematical expression of modal dynamic error is defined in section 0.

The case with parameters ($\eta = 30, \alpha = 10$) is chosen from the critical area where the first mode is anti-symmetrical. This bridge case has A1 (first mode) and S1 (second mode) modes within the significant frequency range of 3-5 Hz as shown in Figure 28 (which is the transfer function estimate).

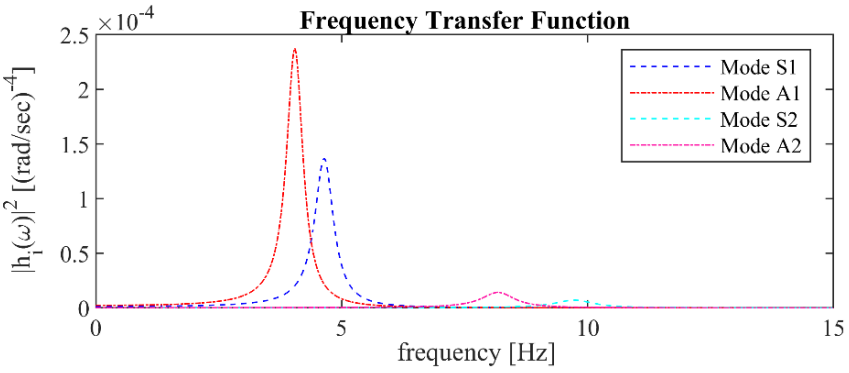

Figure 28; The frequency Transfer Function $|h(\omega)|^2$ at modal frequencies. The system's characteristics are $\omega_0 = 8\pi$ rad/sec and $\gamma_1 = 5\%$.

The cross-modal dynamic error due to the i^{th} and j^{th} modes $\chi_{u,ij}$ is also represented in Figure 29 and Figure 30. The positive and negative maximum dynamic errors are labeled by blue and red boxes respectively. The values of modal dynamic error for the anti-symmetric modes are always positive as these modes mode would only excite bridge in the

MSE cases.

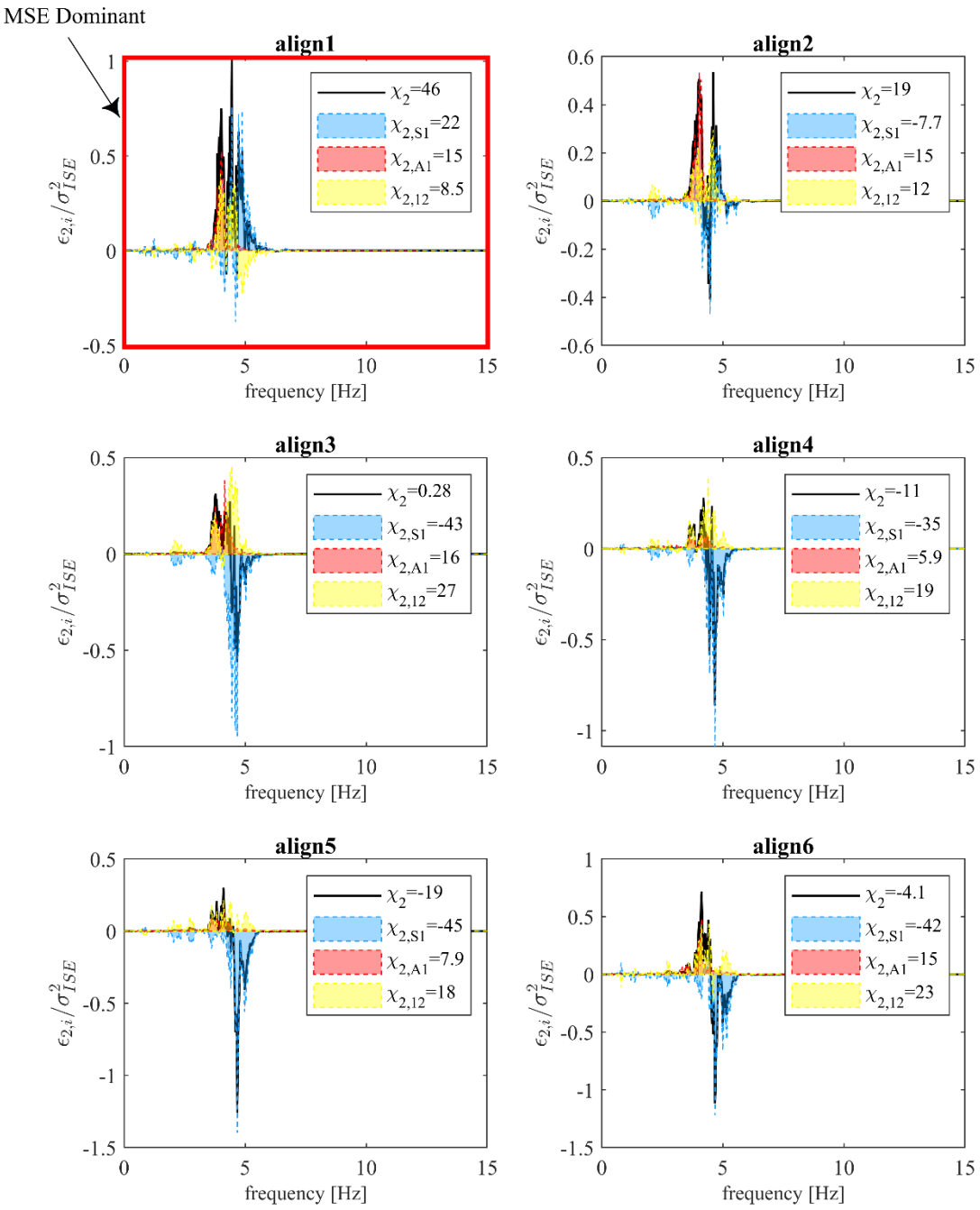

Figure 29; The modal analysis error normalized by σ^2_{ISE} for parameters $\eta = 30, \alpha = 10$ (alignment 1-6).

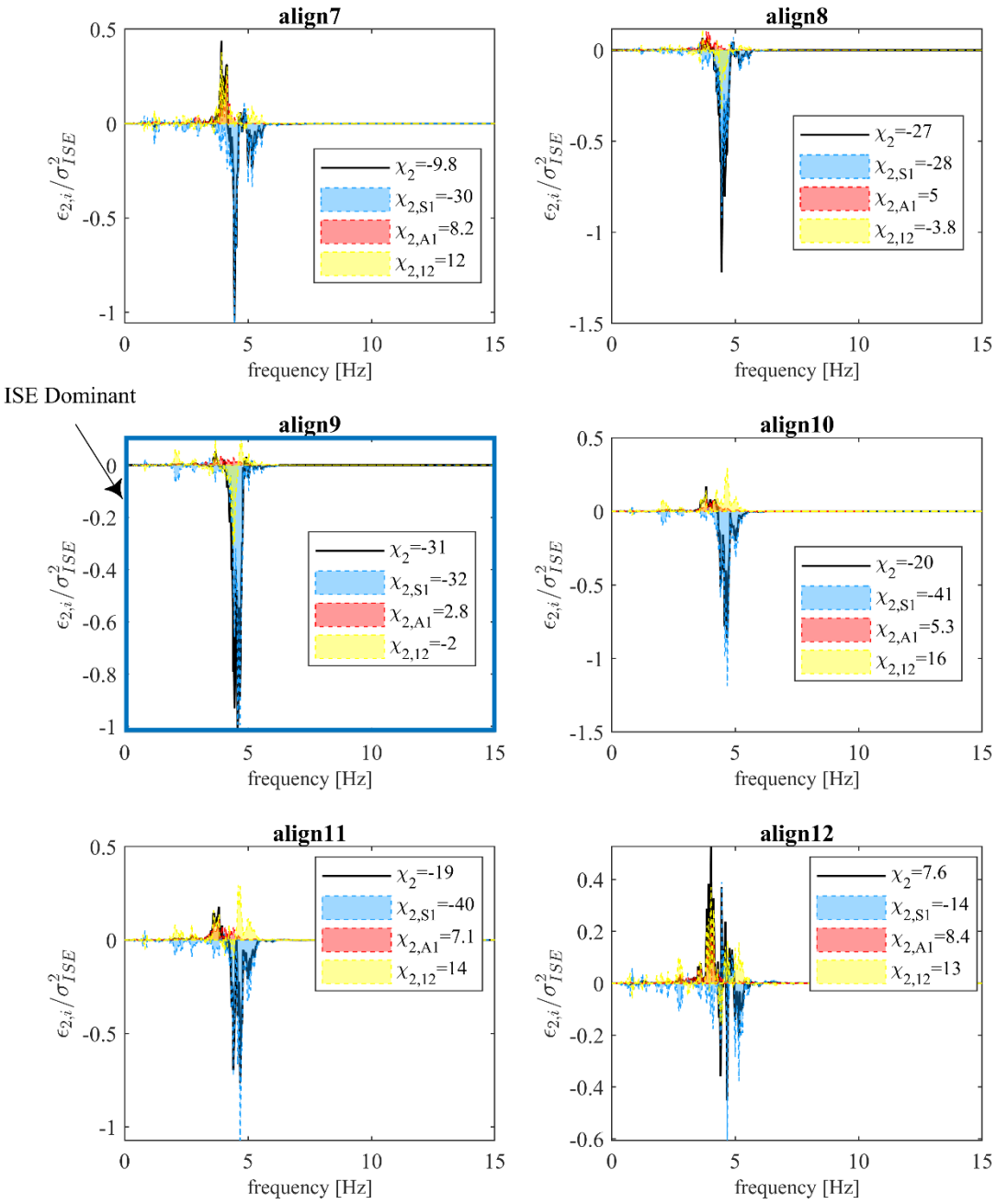

Figure 30; The modal analysis error normalized by σ^2_{ISE} for parameters $\eta = 30, \alpha = 10$ (alignment 7-12).

The interesting result to emerge from Figure 29 and Figure 30 is that the first ant-symmetrical mode (A1) is excited considerably in align.1, align.2, and align.3 although its response is marginal for example in align8, align9, and align10. Thus, even though the transfer function for mode 1 has a higher peak value, this is not necessarily sufficient to result in larger responses for mode 1 (A1).

However, the response pattern is different for the symmetrical mode. The percentage error of S1 mode can be negative which its value is substantially great in align.9, align.10, and align.11. This percentage error can be also positive in another alignment such as align.1 and align.12.

These results highlight the importance of the power/phasing of ground motion inputs. To forensically analyze such effects, we take a closer look at the correlation of ground motion data of the stations at the inner ring with central station C00.

Figure 31 represents the acceleration Power Spectrum of time-series in bridge transversal direction at center station C00 and stations of the inner ring (I01- I12). The bridge orientation where the bridge is more prone to be excited by MSE and ISE cases are labeled by red and blue box respectively. Figure 31 suggests that for orientation with the higher values of power-spectrum of central station (C00-C00) at bridge frequency range (of 3-5 Hz), the symmetrical mode would be induced more substantially in the ISE case. This situation can be seen in align-9 and align-10 where the error of symmetrical mode is negative. This is due to the seismic input at central station C00 chosen for the ISE case has higher overall power than those used for the MSE case inputs. Contrarily, the lower value of the power-spectrum at the central station indicates that symmetrical mode can be more induced by MSE cases. It can be seen in align-1 and align-12 where the dynamic error for both A1 and S1mode is significant and positive.

This result corroborates that there is a correlation between dynamic parameters A_{S1} and power-spectrum. The absolute symmetrical dynamic error has been enlarged for the bridge cases with a bigger value A_{S1}. The sign of error depends on the values of the Power Spectrum at selected stations in the range of transfer function of the first symmetrical mode.

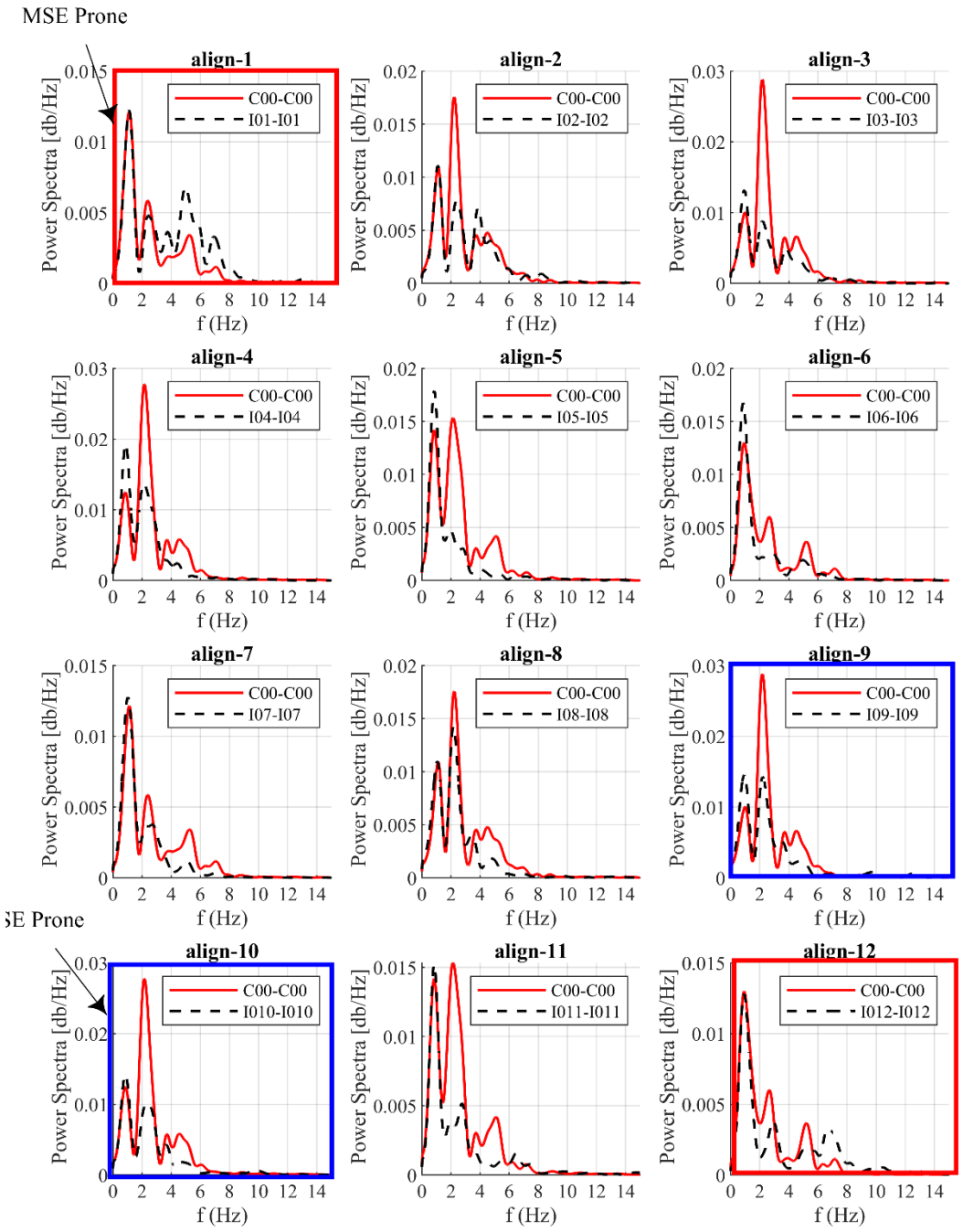

Figure 31; Power Spectrum of acceleration time-series of stations at the inner ring (alignment 1-12) and central station C00. The seismic data at stations are aligned with bridge transvarsal direction at each orientation.

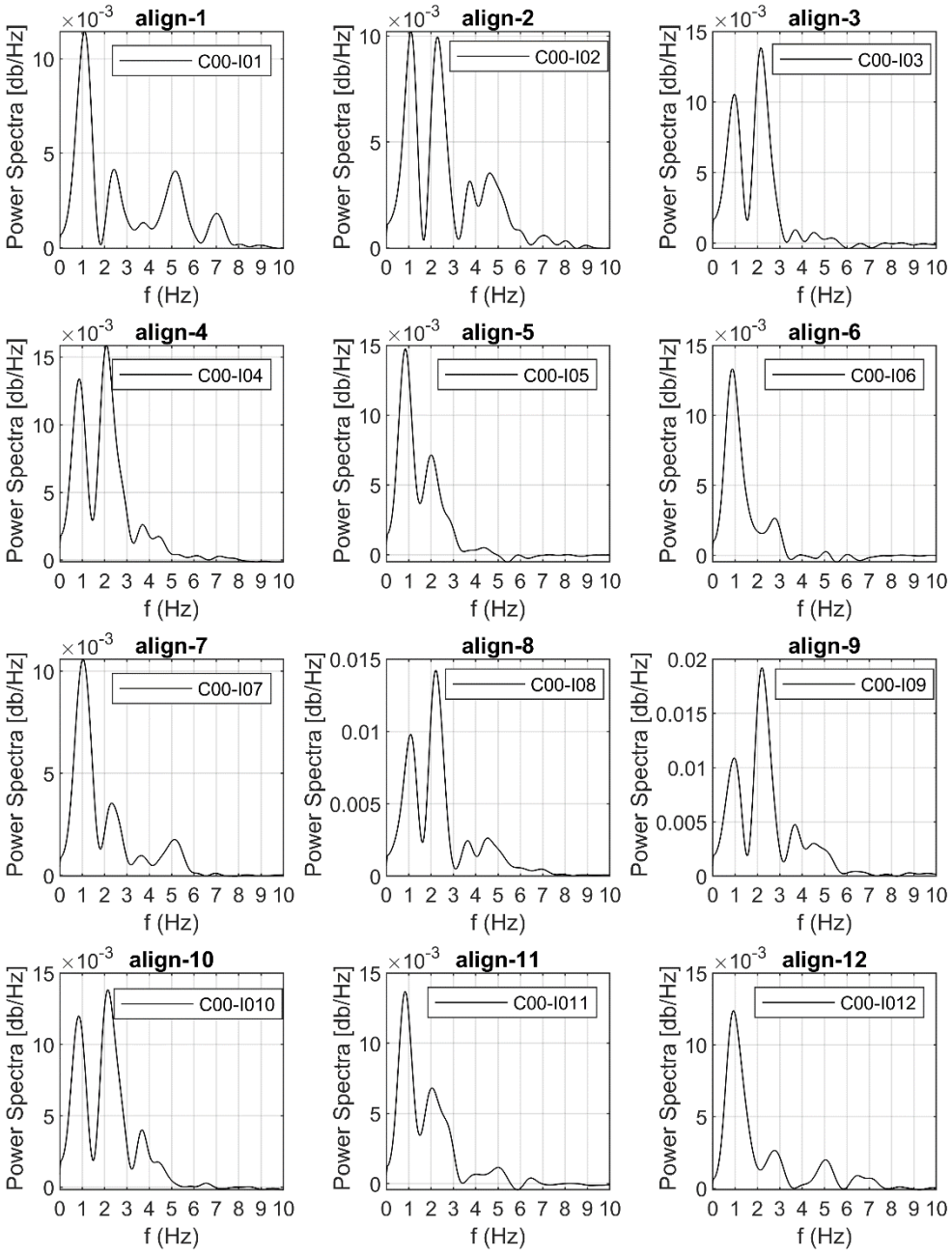

Figure 32; Co-spectrum between C00 and inner ring stations (I01-I12) of SMART-1 array for event 43. The rotated data is aligned with the bridge transversal direction.

Now, consider the co-spectrum between the central station (C00) and stations of the inner ring (I01- I12). The seismic data is rotated with the bridge transversal direction. Despite the fact that the exploration of the CMP factor $B_{u,i}$ shows that this quantity for anti-symmetric mode is negative, it is rather difficult to make a correlation between the response

pattern of anti-symmetric mode in Figure 29 and Figure 30 and co-spectrum in Figure 32. This suggests that a more complicated mechanism exists between anti-symmetric mode response quantity and ground motion input.

Consider now the case where the first mode is now symmetrical, shown in Figure 33 where $(\eta = 30, \alpha = 1)$. This bridge has a very similar transfer function, shown in Figure 33(c), where the bridge's significant frequency range is again between 3-5Hz. Thus, we have very similar frequency ranges filtered by the transfer functions in both cases Figure 31 and 27. However, the errors between MSE and ISE are far lower because of the smaller values of $\alpha_{u,i}(\omega)$ and $\beta_{u,i}(\omega)$ in Eq (2.43) that were predicted by the *geometry only* bounds $\mathrm{A}_{u,i}, \mathrm{B}_{u,i}$.

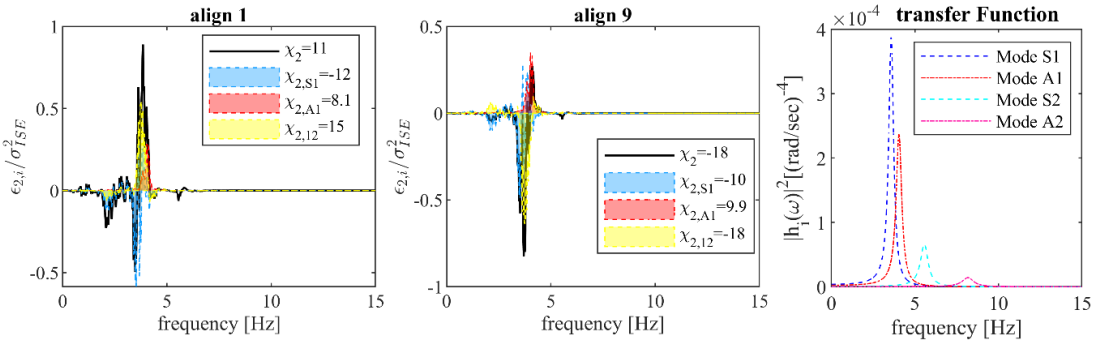

Figure 33; The modal analysis error normalized by σ^2_{ISE} for parameters $\eta = 30, \alpha = 1$. (a) Alignment C00-I01, (b) alignment C00-I09. (c) Frequency transfer function $\gamma_1 = \gamma_1 = 5\%$.

6.8 SUMMARY

A large-scale parametric study was presented herein to explore the sensitivity of the responses to asynchronous excitation of a heuristic bridge where geometry parameters of the bridge differed conceptually due to valley profile.

Firstly, we explore the regions of the *geometry only* parameter space where the first mode of the system is anti-symmetrical (modal analysis). Second, we derive bounds on the modal error between MSE and ISE analyses cases (a bounding analysis) and demonstrate that the errors are likely larger for the cases where the first mode is anti-symmetrical. Both, modal and bounding analyses are *geometry only* analyses that neglect any ground motion characteristics. Therefore, finally, we compare and contrast these predictions with actual time-history analysis (in the frequency domain) that is predicated on both geometry and loading. Results from time-history analysis agree that the error between MSE and ISE analyses could be far larger for the cases where the first mode is anti-symmetrical. It is worth noting that while the maximal/minimal error range between MSE and ISE is larger for the case when the first mode is anti-symmetrical this does not guarantee that for a specific individual loading set that the error will be large. This feature was highlighted by noting that the variation in the bridge system's responses caused by just changing its spatial radial orientation was significant.

Therefore, we concluded that a larger error range between MSE and ISE analyses is likely to occur when the first mode is anti-symmetrical. But is this due to a larger magnitude of the anti-symmetrical mode in the responses? For these bridge configurations, numerical time-history results indicate that the anti-symmetrical mode may occasionally play some significant role in the responses, with a specific ground motion content. However, the main component in the response seems due to the symmetrical mode even when it is not the first mode.

The *geometry only* modal analysis is able to highlight parameter regions where the first mode is anti-symmetrical, and the *geometry only* bounding analysis is able to estimate the likely relative magnitude of the errors between MSE and ISE analyses. Both analyses

have some utility in highlighting the cases where it is expedient to perform both MSE and ISE analyses to ensure a conservative analysis estimate of the responses.

Finally, we highlight that the critical parametric cases of larger error ranges between MSE and ISE occurs when the valley profile is shallow with a central rise. This case results in a first mode that is anti-symmetrical but it is still the case that most of this error is due to the first symmetrical mode (mode 2 here).

6.9 NOMENCLATURE

Dimensions in the following list are force [F], length [L], and time [T] with non-dimensional angles defined in Radians [Rad] and other dimensionless quantities defined by [ ].

$\mathrm{A}_{u,i}$	Auto Modal Participation (AMP) factor of uth DOF due to ith mode []
$\mathrm{B}_{u,i}$	the Cross-Modal Participation (CMP) factor of uth FOF due to ith mode []
f_i	i^{th} modal frequency $[T]^{-1}$
$h_i(\omega)$	i^{th} modal transfer function $[rad]^{-2}[T]^{-2}$
H	maximum pier height [L]
$\mathbf{K}_{11}, \mathbf{K}_{12}, \mathbf{K}_{22}$	Non-dimensional block deck stiffness matrices []
L_t	Total length [L]
m_d	Deck mass per unit length $[F][T]^2[L]^{-2}$
m	Number of deck DOFs []
$\mathbf{M}_{11}, \mathbf{M}_{12}, \mathbf{M}_{22}$	Non-dimensional deck block mass matrix []
n	free DOFs (unknowns) of the deck []

s	Number of supports []
S_{uu}	the power spectral density of the response of the u^{th} DOF. $[L]^2$
t	Time [T]
$\mathbf{u}$	Dynamic bridge deck dDOFof vector [L]
$\mathbf{u}_g$	Ground DOF vector [L]
α	Pier to pier stiffness ratio []
$\alpha_{u,i}(\omega)$	the summation of power terms coefficient in the modal error of u^{th} DOF due to the i^{th} mode []
$\beta_{u,i}(\omega)$	the summation of cross-terms and phases coefficient in the modal error of u^{th} DOF due to the i^{th} mode []
γ_i	i^{th} modal damping ratio []
$\mathbf{\Gamma}_i(\omega)$	i^{th} modal participation vector []
Γ_{ip}	Participation factor i^{th} mode corresponding to p^{th} ground motion input []
$\varepsilon_{u,i}(\omega)$	the modal error of u^{th} DOF due to the i^{th} mode $[L]^2$
$\varepsilon_{u,ij}(\omega)$	modal cross-analysis error of u^{th} DOF due to the i^{th} and j^{th} modes $[L]^2$
η_i	i^{th} pier to deck stiffness ratio []
σ_u^2	The 'mean-squared' dynamic response of the u^{th} DOF of the structure $[L]^3$
Φ	Partial eigenvector matrix []
$\boldsymbol{\phi}_i$	Eigenvector of i^{th} mode []
χ_u	dynamic error in dynamic response between MSE and ISE cases []
$\chi_{u,i}$	contribution of i^{th} mode to the dynamic error []
$\chi_{u,ij}$	cross-modal contribution of mode i and j to the dynamic error
ω	Fourier frequency in the frequency domain $[Rad][T]^{-1}$
ϖ	System frequency parameter $[Rad][T]^{-1}$

ω_A	first circular frequency of anti-symmetrical modes
ω_i	i^{th} modal Natural frequency [Rad][T]$^{-1}$
ω_S	first circular frequency of symmetrical modes

Chapter 7

Parametric Exploration of A Non-linear Bridge System

The contents of this chapter have been adapted from the study (Meibodi and Alexander, 2020) that published in:

MEIBODI, A. & ALEXANDER, N. A. 2020. Exploring a generalized nonlinear multi-span bridge system subject to multi-support excitation using a Bouc-Wen hysteretic model. *Soil Dynamics and Earthquake Engineering*, 135, 106-160.

7.1 INTRODUCTION

Conventional nonlinear finite element analyses use tens of thousands of degrees of freedom for large bridges in 3D and must have a prescribed explicit geometry. Thus, any parametric exploration using large numbers of ground motions places a huge computational burden on any analyst. This makes such systematic and extensive parametric explorations of geometric effects, such as valley profile, etc. very difficult to undertake in practice. As an alternative, we developed a reduced-order nonlinear model in Chapter 3 that enables parametric explorations to be undertaken in a more timely fashion, and thus allows far more parametric cases to be considered.

Hence, first, the proposed nonlinear reduce order model is exemplified as a prototype four-span bridge structure (Lupoi et al., 2005). Next, an extensive parametric analysis scheme is conducted in order to explore the parametric behavior of this nonlinear bridge system.

7.2 EXPLORATION OF A HEURISTIC BRIDGE REFERENCE MODEL

7.2.1 Reference prototype bridge definition

The reference bridge studied in section 5.3.1 is selected to exemplify the proposed procedure. The uniform concrete deck is pre-stressed box girders and bridge piers have a rectangular hollow section. (Figure 34).

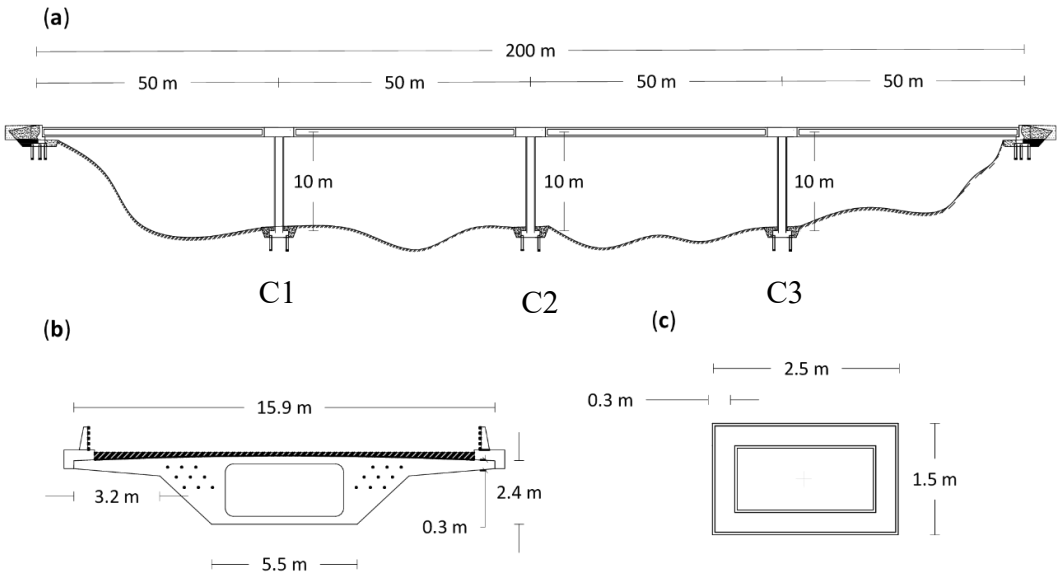

Figure 34; configuration of studied real bridge; (a) bridge arrangement; (b) deck section; (c) pier section.

The nominal yield strain is $\varepsilon_y = 0.0021$ and modulus elasticity of concrete is 34 GPa. The damping ratio of the first and second modes are assumed equal to 0.05 in the Rayleigh damping Eq (3.29). System frequency parameter ϖ equal to 5 (Section 6.2.1) is adopted which is consistent with the prototype bridge frequency range. The values of transversal stiffness k_i for cantilever piers are taken equal to $3EI_i/h_i^3$. The yielding displacement for all columns is calculated to equal 6cm. The summary of section details and dynamic parameters are given in

Table 3.

Table 3; the section property and dynamic parameters for bridge prototype

Parameters	Value	Units
m_b	19.6	[ton/m]
I_d (deck)	156	[m^4]
k_i	1	[m^4]
ϖ	5	[rad/s]
η_i	2.4	[ ]

7.2.2 Nonlinear time history analysis of prototype reference bridge

Figure 35 to Figure 37 show the inelastic responses of the nonlinear time history analysis for the studied bridge when is subjected to real asynchronous excitation. The seismic ground motion data is chosen from the first alignment of the SMART-1 Array in order to represent the spatial variability effect. The maximum of the PGA at stations is equal to 0.23g. The displacement time history for linear-model where α in Eqs (3.17). and (3.32) is set equal to 1 has been also plotted for the sake of comparison.

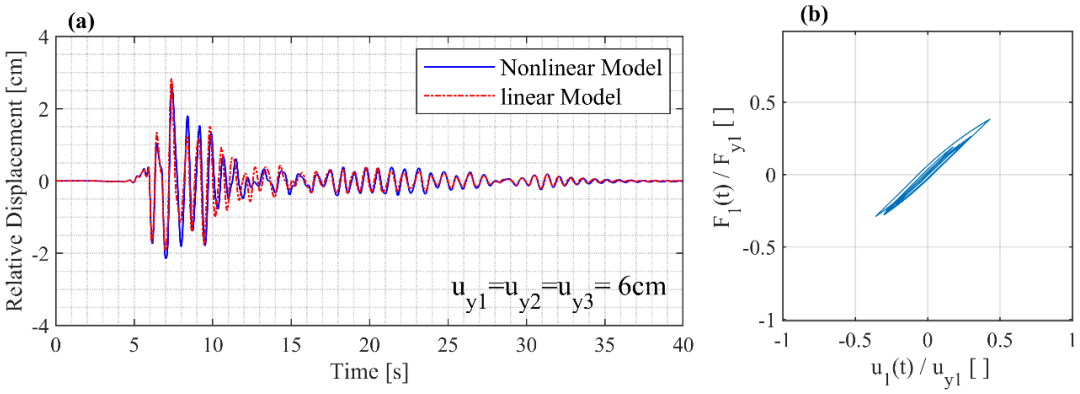

Figure 35;(a) response of outer piers (C1) under asynchronous excitation; (b) normalized displacement-force cycle of outer pier (C1); PGA=0.23g.

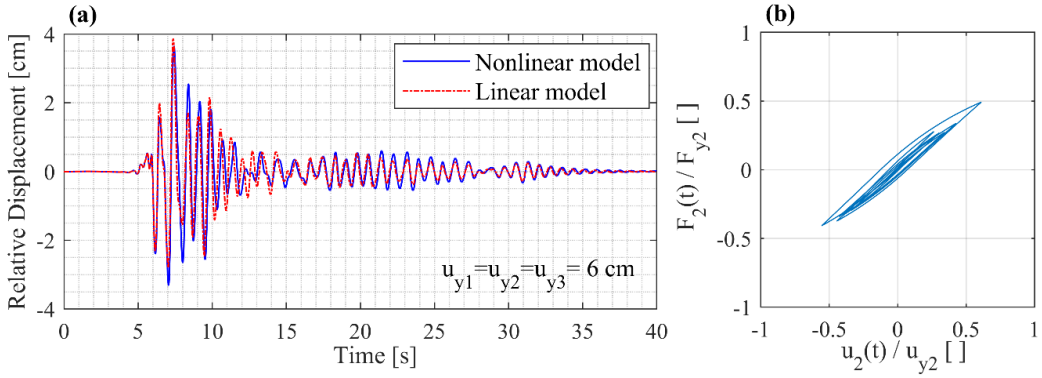

Figure 36; (a) response of middle piers under asynchronous excitation; (b) normalized displacement-force cycle of middle pier (C2); PGA=0.23g.

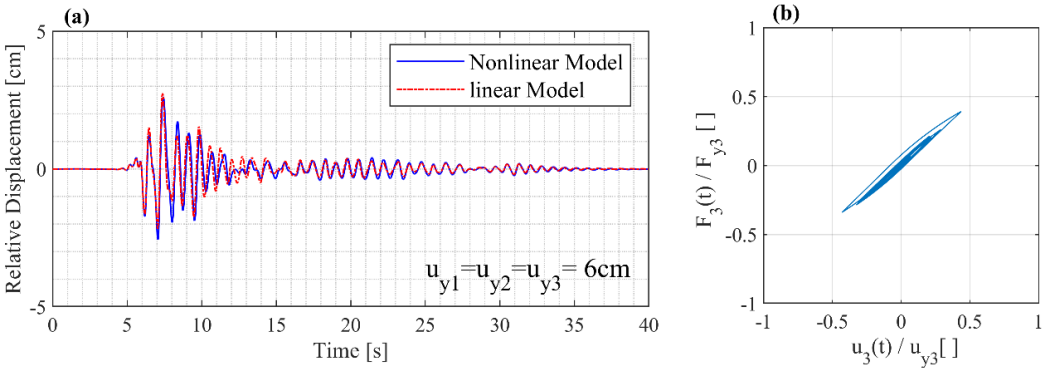

Figure 37;(a) response of outer pier (C3) under asynchronous excitation; (b) normalized displacement-force cycle of outer pier (C3); PGA=0.23g.

As it can be seen, for this configuration, the piers exhibit only slightly hysteresis while the peak transversal deformation does not reach the yielding point (typical of RC sections (Kashani et al., 2019)). The results suggest that piers exhibit limited ductile behavior therefore, the unscaled amplitude of the SMART-1 event 43 is not large enough to demonstrate significant energy dissipation. For a deeper understanding of hysteretic effects, we assumed that the bridge is constructed in a medium to high seismicity area with a design PGA equal to 0.69g. By a simple ground motion amplitude scaling an example of this case is shown in Figure 38 to Figure 40.

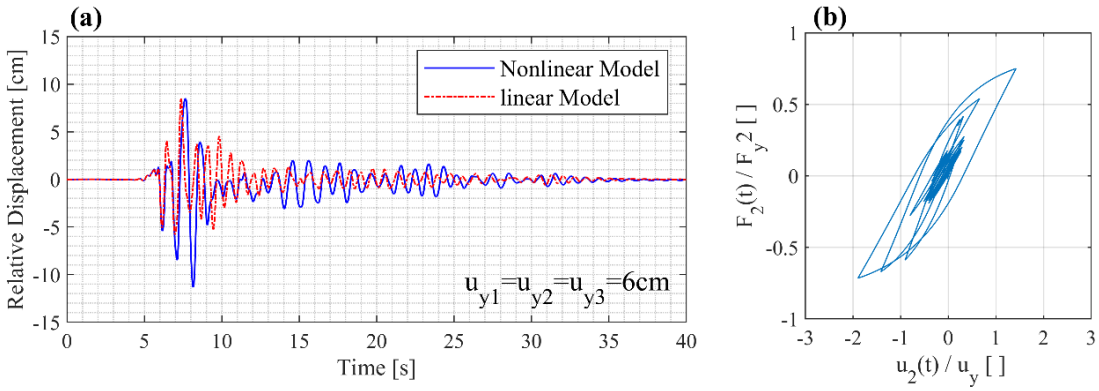

Figure 38;(a) Response of outer pier (C1) under asynchronous excitation; (b) normalized displacement-force cycle of outer pier(C1) ; PGA=0.69g.

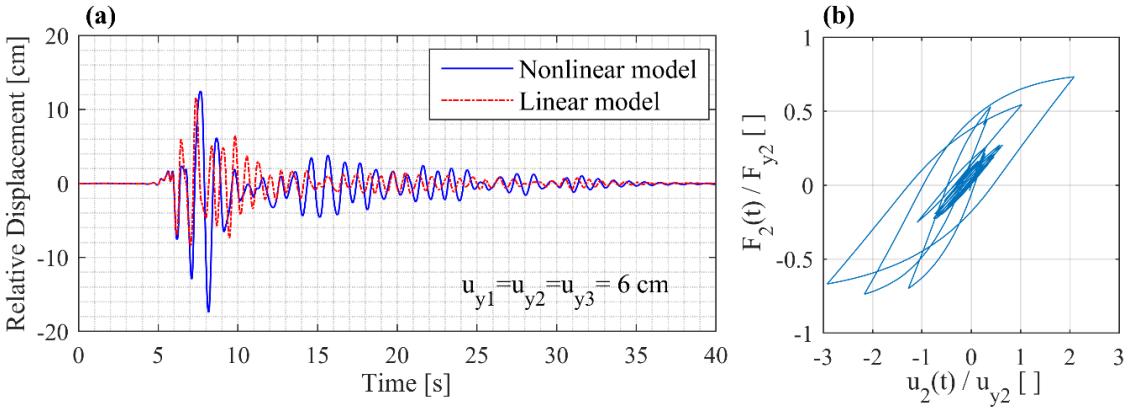

Figure 39; (a) Response of middle pier (C2) under asynchronous excitation; (b) normalized displacement-force cycle of middle piers; PGA=0.69g.

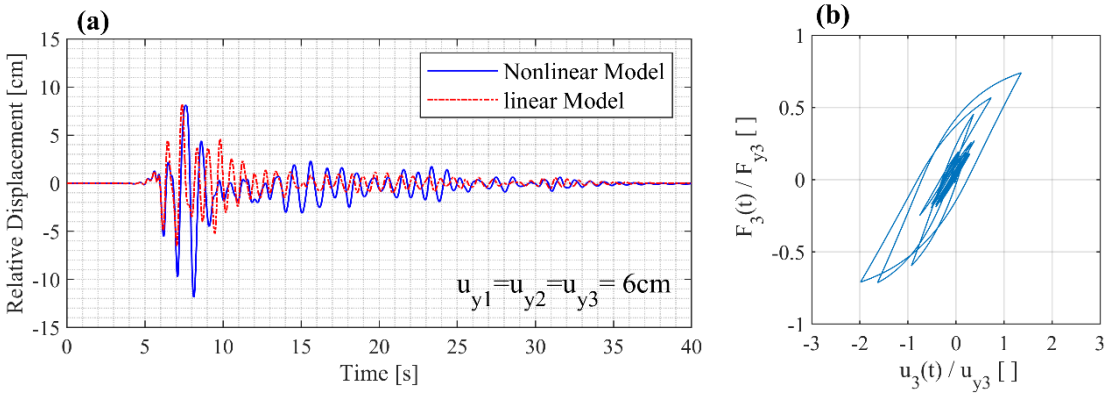

Figure 40; (a) Response of outer pier (C3) under asynchronous excitation; (b) normalized displacement-force cycle of outer piers (C3); PGA=0.69g.

We now explore examples of non-uniform valley profiles. In this set of dynamic configurations, the middle pier exhibits larger ductility where the peak response exceeded the yield displacement. Incorporation of hysteresis pier would increase slightly the peak dynamic response in this case. Let us consider another case Figure 41 where the middle pier height is reduced to 6m.

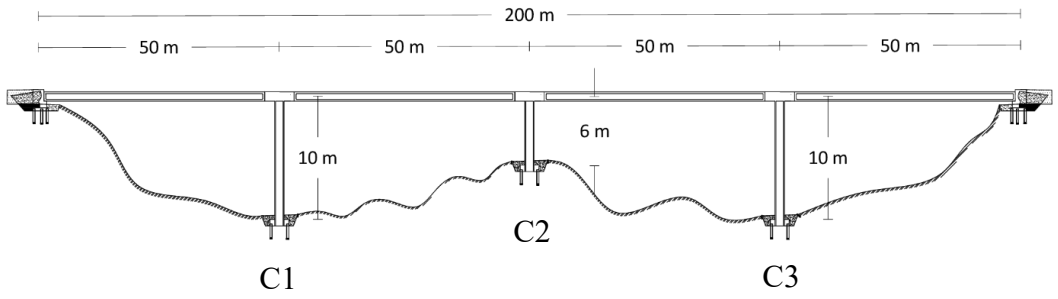

Figure 41; bridge configuration with the shorter middle pier.

The analysis in Figure 42 to Figure 44 show that the peak linear displacements responses are greater than those where nonlinearity is taken to account suggesting that pier hysteresis reduces the displacement responses while Figure 38 to Figure 40 suggest the opposite. Thus, suggesting that the so-called “equal displacement rule” is not generally valid. Results presented in this section are anecdotal examples; so, we seek to extend the generality of these analyses by the large-scale parametric study.

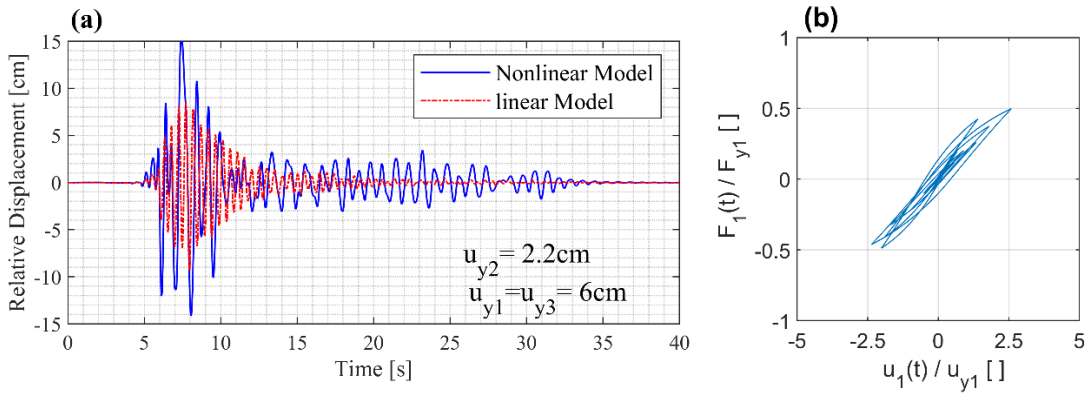

Figure 42; (a) response of outer pier (C1) under asynchronous excitation; (b) normalized displacement-force cycle of outer pier (C1); PGA=0.69g,

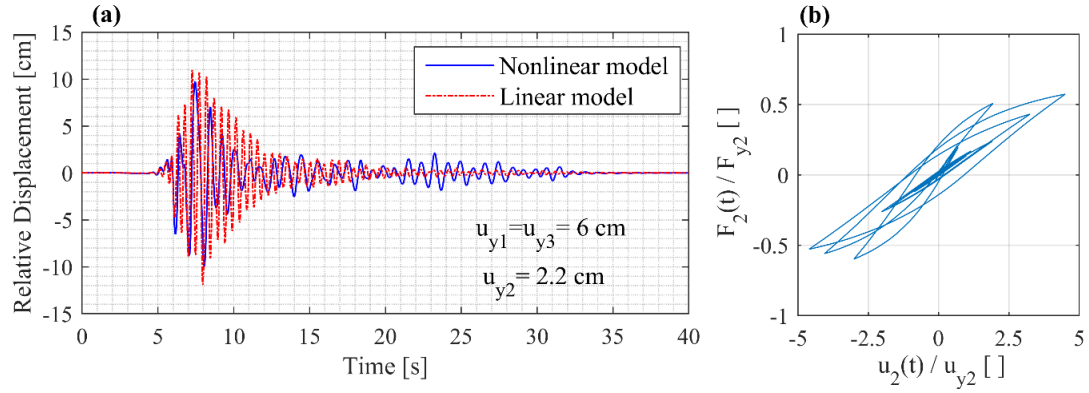

Figure 43; (a) response of middle pier (C2) under asynchronous excitation; (b) normalized displacement-force cycle of middle piers (C2); PGA=0.69g,

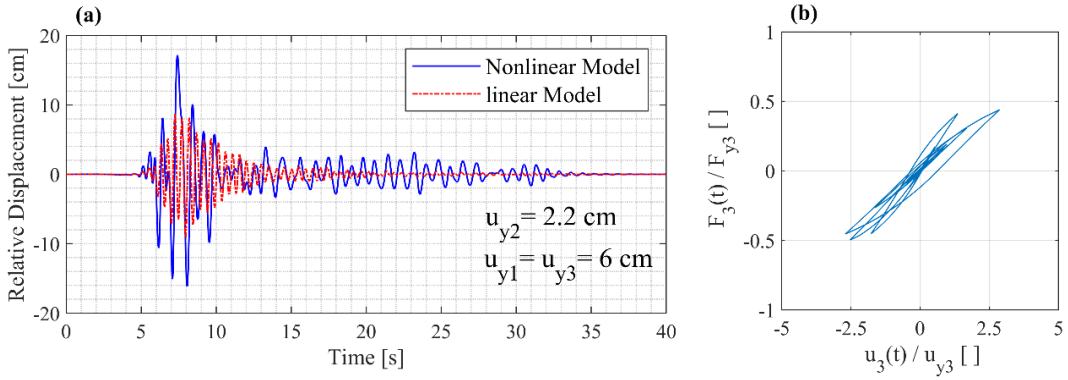

Figure 44;(a) response of outer pier (C3) under asynchronous excitation; (b) normalized displacement-force cycle of outer pier (C3) ; PGA=0.69g,

7.3 LARGE-SCALE PARAMETRIC STUDY

7.3.1 Parametrically exploration of valley profile.

In this section, we investigate the effect of spatial variability on the dynamic response when the pier hysteresis is taken to account. In this setting, we explore such effects where the geometrical configuration of the bridge due to the valley profile of ground is altered. The configuration of bridges and bridge parameters is explained in 6.2 for a linear case. The same framework is employed here. However, some assumptions are considered to incorporate pier nonlinearity into the parametric study. Herein it is supposed that due to topographical change at supports, the height of piers is altered while the section of the piers remains constant. This assumption is expedient for construction purposes, as well as it makes use of a simplified form of yield displacement representation of Eq(3.33). In addition, we change the symbol of the middle Pier to the outer pier stiffness ratio to ρ. It avoids confusion over hysteretic parameters post to pre-yield stiffness ratio (α) in the Bouc-Wen model.

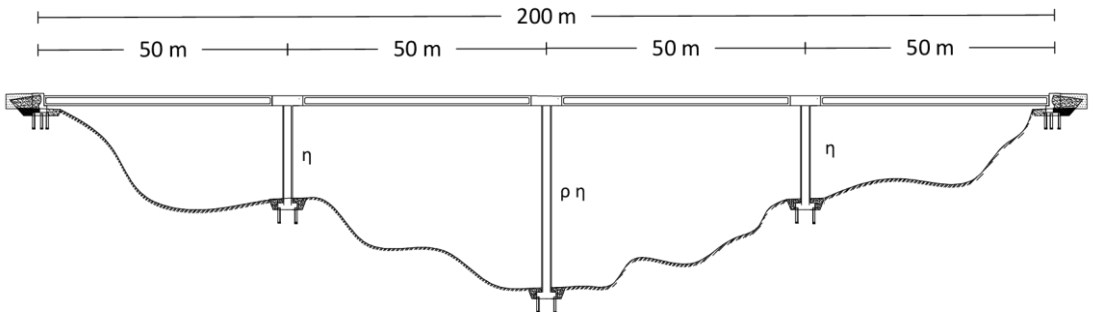

Figure 45; Layout of symmetrical bridges for parametric study

7.3.2 Defining error in ductility estimates using MSE and ISE

To compare the dynamic response of the bridge under sets of ground motion (ISE and MSE), we introduce the performance measure similar to Eq (6.5) as follow:

$$\chi(\eta,\rho,i,j)=100\left\{\frac{\max_t|u_i(t)|_{MSE}-\max_t|u_i(t)|_{ISE}}{\max_t|u_i(t)|_{ISE}}\right\} \tag{7.1}$$

Where $\chi(\eta,\rho,i,j)$ is the percentage difference (error) in pier ductility, for a bridge with (i) parameters η and ρ and (ii) pier i and bridge orientation j, between a MSE and ISE simulations. The number j denotes the bridge orientation which varies from 1 to 12. SMART-1 array ground motion for event 43 is chosen to generate MSE simulations where abutments and pier supports are exposed to different ground motion time-series. For the ISE case, the ground excitation from center station I00 is employed at supports and abutments. As we are only interested in the range of errors with regard to bridge orientation *j* and pier *i,* we consider the following statement:

$$\min_{\forall i,\forall j}\{\chi\}\le\chi\le\max_{\forall i,\forall j}\{\chi\} \tag{7.2}$$

The minimum of this range corresponds to the cases where MSE simulations are non-conservative. The maximum of these ranges corresponds to the cases where MSE is conservative. To evaluate the effect of nonlinearity, we perform Incremental Dynamic Analysis (IDA) to estimate the level of intensities where the bridge excites (i) in an elastic (ii) and a nonelastic range. In the following section, the procedure is explained in full detail.

7.3.3 Incremental dynamic analysis (IDA)

IDA is a parametric study of the structural model involving a series of nonlinear analyses performed under a scaled image of ground motion records (Vamvatsikos and Cornell, 2002). The range of scaled intensity levels is wisely selected to cover an entire range of elastic to the plastic region and finally to structural instability (collapse state).

With the suitable chosen damage index quantity (i.e. maximum ductility), it is possible to identify the linear and nonlinear region and collapse state for a structural system with mild degradation in the IDA curve (Goda et al., 2009). The reference bridge explained in section 7.2.1 is chosen for IDA analysis. The MSE ground motion series used for the studied bridge is selected as unscaled time history. To perform IDA, first, the time series at pier supports and abutments are simultaneously multiplied by a scale factor with the range from 0.01 to 5 to obtain a set of ground motions with different intensity levels. Then, a series of nonlinear analyses are performed under scaled ground motion records to obtain the maximum ductility of the middle pier from time history response at different Peak ground motion (PGA). IDA curve of the middle pier with the Bouc-Wen model of the studied bridge is shown in Figure 46.

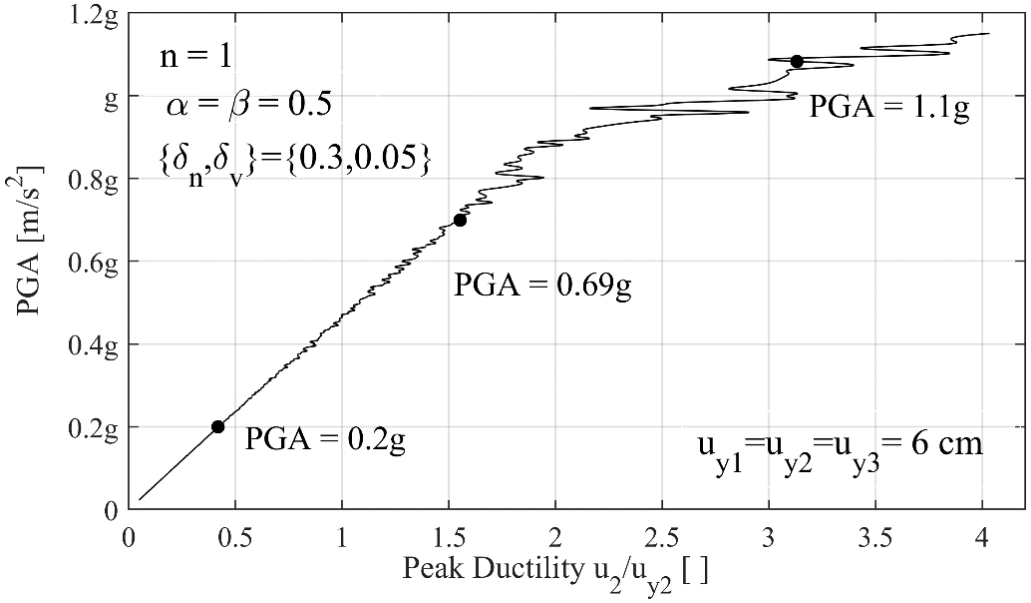

Figure 46; Example of IDA curves for central piers with strength deterioration and stiffness degradation for the prototype bridge with η=2.4, ρ=1, and alignment 3.

As it can be observed from the IDA curve, the pier exhibits almost pure elastic behavior at PGA= 0.2g. From this point onwards, the IDA curve is subjected to small fluctuations and curvature as hysteresis initiates in piers. In this study, we use a PGA of

0.2g (low seismicity), 0.69g (medium seismicity), and 1.1g (high seismicity) as qualitative estimates of the different regions of system behavior.

7.3.4 Effect of different valley profiles, alignment, and ground motion intensity.

Figure 47 shows the sample of inelastic time-history analyses for outer pier 3 under MSE and ISE simulation with PGA=0.69g. Figure 47(a) indicates that maximal ductility for MSE cases is 19% greater than one for ISE cases. Figure 47(b) shows the difference of -22% between ISE and MSE cases implying that ISE is more conservative for this alignment.

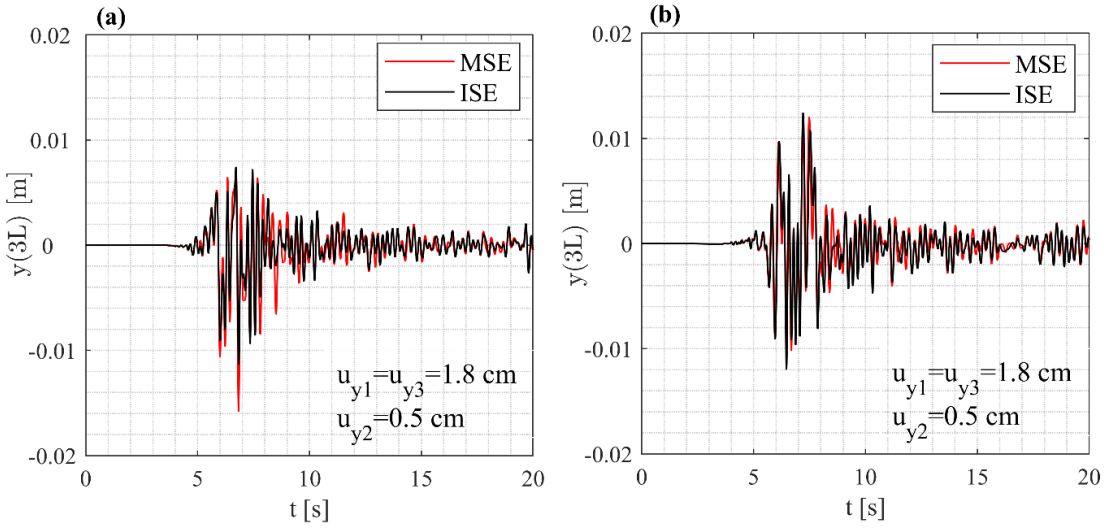

Figure 47; Examples of the outer pier 3 displacement responses for parameters $\eta = 15, \rho = 6,\ PGA = 0.69g$, (a) alignment 1 with an error in ductility of $\chi = 19\%$, (b) alignment 5 with an error in ductility of $\chi = -22\%$

As discussed in sections 6.2.1 and 6.3, the dynamic parameters, middle to outer pier stiffness ratio ρ , and pier to deck stiffness ratio η can be viewed as a proxy for the valley profile. To explore such effects for a wider range of dynamic parameters ρ,η , let's consider the cases with PGA=0.2g where bridges mostly excite in a linear-elastic region. Figure 48 displays the errors in ductility χ (of any pier and alignment) if MSE is not employed. It required a substantial computational effort of 90000 full nonlinear time-history analyses

that make use of 192 different ground motions. Figure 48 (a) shows the lower bound of error for ductility and Figure 48 (b) displays the upper bound of error ductility. From these analyses, it is clear that any configuration of the bridge (ρ, η) ISE could be either conservative or nonconservative. From Figure 48 (b), it is possible to identify the critical regions (the area I with 4< ρ <10, 4< η <30, and area II with 70< η) where MSE analyses are necessary. This numerical result is consistent with analytical findings (Figure 21 based on geometry alone). The analytical curves from Figure 21 are plotted in Figure 48 to Figure 50 for the sake of comparison.

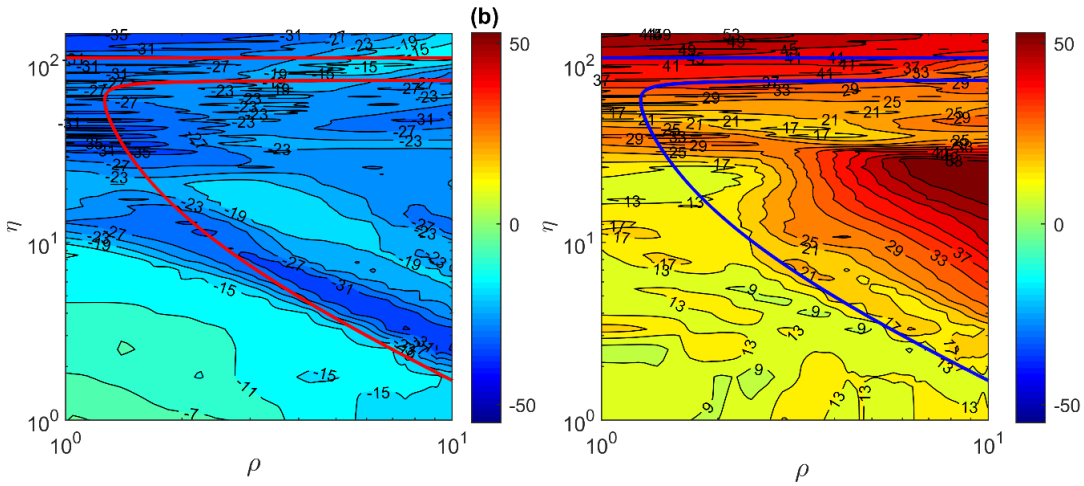

Figure 48; Error range in pier ductility χ for symmetrical bridges for a low seismicity (a) Lower bound of errors (b) upper bound of errors; $-47 \leq \chi \leq 63.7$; PGA=0.2g,

Now, consider the analyses for nonlinear cases with the medium and high-intensity levels as shown in Figure 49 and Figure 50.

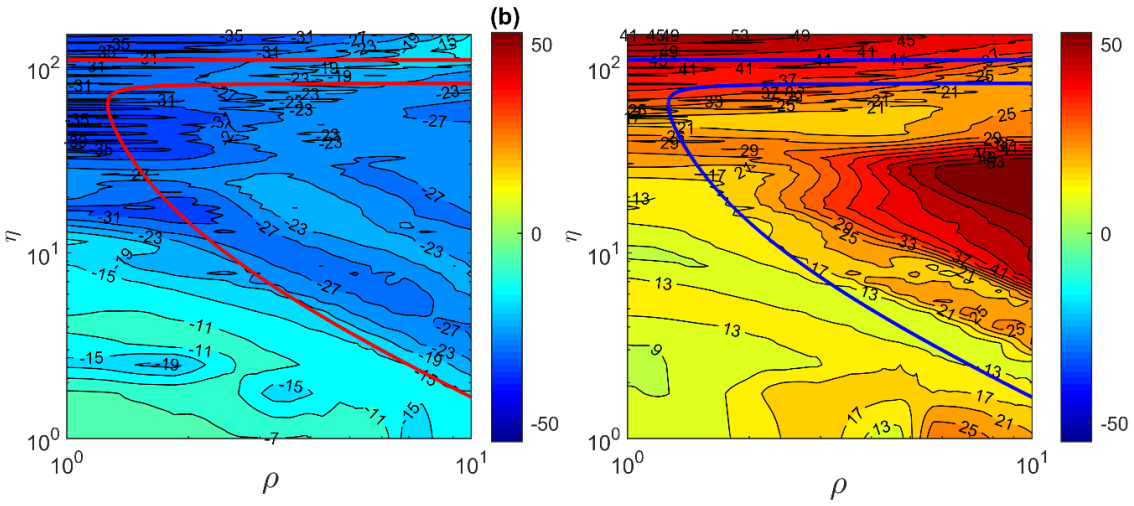

Figure 49; Error range in pier ductility χ for symmetrical bridges for medium seismicity (a) Lower bound of errors (b) upper bound of errors; $-50.93 \le \chi \le 66.08$; PGA=0.69g,

Maximal errors in Figure 48 and Figure 50 occur for high $\eta \simeq 20$ and $\rho > 1$, which from

Figure 19 (b) is a shallow valley with a central rise. The response patterns in Figure 49 and Figure 50, for nonelastic cases, are similar to the linear ones. However, consider the size of the parametric region that shows an error above 50%, in plots Figure 48 and Figure 50. As the PGA increase, there is a small increase in the parametric bridge/valley configurations that show more error in ISE analyses. This trend is also seen for lower bound plots where the maximal negative error slightly decreases to -50.9 and -54.5 for PGA=0.69g and PGA=1.1g respectively.

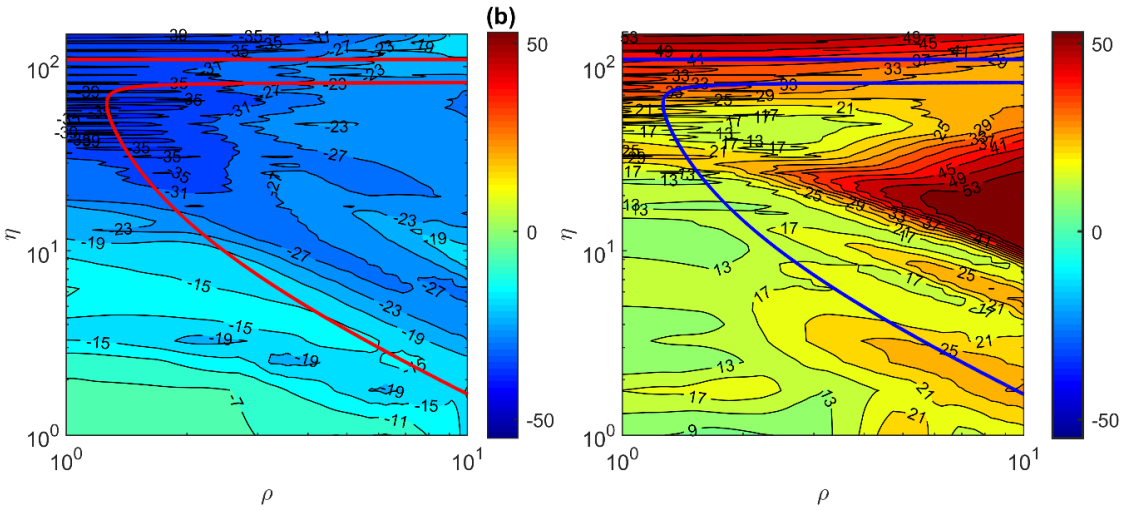

Figure 50; Error range in pier ductility χ for symmetrical bridges for high seismicity (a) Lower bound of errors (b) upper bound of errors; $-54.5 \leq \chi \leq 65.8$; PGA=1.1g,

7.4 SUMMARY

The extensive parametric analyses using the proposed nonlinear dynamic model were performed to explore the detrimental effects of asynchronous excitation while the geometrical configuration of the bridge (due to valley profile) and bridge alignment are varied.

Note that in our heuristic case we were able to model this multi-span bridge effectively with only 3-DOFs rather than thousands of DOFs in a typical FEA. Thus, the computational saving for extensive parametric studies could be considerable.

Incremental Dynamic Analysis (IDA) has been performed to identify the peak ground motion (PGA) when the nonlinear behavior of the bridge model initiates. From this analysis, three points, PGA=0.2g (low seismicity), PGA=0.69g (medium seismicity), and PGA=1.1g (high seismicity) are chosen to explore the nonlinearity effect on the geometrical parametric study.

It can be suggested from the result of the parametric study that as the PGA increase,

the nonlinear behavior of bridge piers tends to reduce the critical regions where MSE analyses are necessary. These critical regions have been labeled by a theoretical curve (Figure 21 based on geometry alone). Although there is a reduction in critical regions for higher seismicity, an increase has been observed in maximal and minimal errors (χ) in ISE analysis estimates.

7.5 NOMENCLATURE

Dimensions in the following list are force [F], length [L], and time [T] with non-dimensional angles defined in Radians [Rad] and other dimensionless quantities defined by [ ].

A, β, γ	Basic hysteresis shape control []
d_c	Depth of the pier's sections [L]
EI_d	Deck flexural rigidity (about z-axis) [F][L]^2
EI_i	ith Pier flexural rigidity [F][L]^2
h_i	Height of i^{th} pier [L]
I_d	The moment of inertia of deck [L]^4
k_i	Pier transversal flexural stiffness [F][L]$^{-1}$
m_b	Deck mass per unit length [F][T]^2[L]$^{-2}$
m	Number of deck DOFs []
n	Sharpness of yield []
PGA	Peak ground acceleration [L] [T]$^{-2}$
s	Number of Piers []

t	Time [T]
u_{yi}	yield displacement of i^{th} pier [L]
$\mathbf{u}$	Bridge deck DOFs vector (including free and constrained DOFs) []
$y\ (x,t)$	transversal displacement relative to the ground at time t [L]
α	post- to preyield stiffness ratio; []
γ_i	i^{th} modal damping ratio []
δ_v	Strength degradation []
δ_n	Stiffness degradation []
ε_y	Nominal yield strain[F] $[L]^{-2}$
η_i	i^{th} pier to deck stiffness ratio []
ρ	Pier to deck stiffness ratio []
χ	Percentage error is pier deformation when using ISE [%]
ϖ	System frequency parameter [Rad]$[T]^{-1}$

Chapter 8

Summary, Conclusion, And Major Finding

8.1 MAJOR DEVELOPMENTS AND FINDINGS

In this thesis, a generalized reduced-order model of a multi-support bridge is set up to take account of the effect of spatially ground motions. Real spatiotemporal ground motion time-series (from the SMART-1 array, Taiwan) are used, as an alternative to employing artificial ground motion based on some spatial incoherence kernels. An extensive parametric study was developed to explore geometric effects, such as valley profile. The main developments and findings of the study are summarized below:

i. A proposed novel reduced order model is highly computationally efficient. It allows us to perform large-scale parametric studies and explores a wider range of

bridge geometry and input seismic motion arrangement. key system parameter groups including pier to deck stiffness ratio, inter-pier stiffness ratio, and the system fundamental frequency parameter are highlighted. In the scope of these parameters, the bounds on the error between MSE and ISE analysis are defined in terms of the (a) Auto Modal Participation (AMP) and (b) Cross-Modal participation (CMP) factors. They are independent of ground motion input therefore, they can provide an estimation of likely error prior to dynamic analysis.

ii. The nonlinearity of the bridge system is defined by assuming plasticity occurs only in the piers (which is typical) via the Bouc-Wen model that includes strength deterioration and stiffness degradation. This proposed nonlinear system provides a considerable reduction of system complexity to perform a robust inelastic time-history analysis.

iii. The modal exploration of *geometry only* parameter reveals the space where the fundamental mode of the bridge system is anti-symmetrical. The bounding analysis demonstrates the modal error where multi-support ground motion is taken to account. It suggests that this error is considerably large for these bridge geometry sets with the first symmetrical mode. Both, modal and bounding analyses are independent of seismic input. Hence, they can be considered an approximate method of predicting the whether or not detrimental effects of asynchronous ground motion might occur for a bridge prior to any nonlinear time-history analyses.

iv. The result from actual numerical analysis confirms these predictions. These actual time-history analyses (in the frequency domain) reflect both effects of *geometry only* parameter and loading. The absolute dynamic error has been enlarged for the bridge cases with a first anti-symmetrical mode. Assessment of whether MSE cases

are conservative or not depends on the value of Power Spectrum at frequency seismic motion input in the range of transfer function of first symmetrical mode.

v. Returning to the hypothesis made in this study, it is now possible to state that the effect of anti-symmetrical mode on dynamic error is occasionally significant for the bridge configuration when the first mode is anti-symmetrical. However, the response error is mainly determined by the contribution of symmetrical mode even when it is not the fundamental mode.

vi. The evidence from this study suggests that the bridge constructed in a shallow valley with a central rise is more susceptible to spatial incoherence of ground excitations. In these cases, the contribution of alignment to the error in ISE is up to 80% of the maximal error. In these cases, the bridge is very sensitive to input ground motion variation caused by alignment.

vii. The results in Chapter 6 and 0 indicate that for each geometry parameter set, the error engendered in ISE varied substantially when the bridge alignment is altered (i.e. the compass bearing of the bridge's longitudinal axis is altered for the case of a given spatiotemporal ground motion). The large range between minimum and maximum errors in ISE suggests that bridge alignment is an arguably more important factor than valley profile.

viii. Pier nonlinearity (with increasing the ground motion intensity) causes a 3% increase in the unconservative maximal error in ISE which is insignificant. However, it does also produce a -16% change in the conservative minimal error in ISE which is more important. Generally, nonlinearity tends to increase the range between maximal and minimal errors in ISE.

8.2 RECOMMENDATIONS FOR FURTHER STUDIES

Further work is required in order to validate the consistency of the above observations using a larger database of real recorded spatiotemporal ground motion and the wider range of bridge configurations. The future study to incorporate the application of the proposed methodology are Recommended as the following:

i. The event-43 from the SMART-1 array occurred at the sedimentary valley which is quite flat. The variation of profile valley only considers the structural effect of bridge configuration on the response. This change is not be reflected in ground motion excitation at the supports. It is required to develop the parametric modeling to incorporate spatial variability effect when the high of the ground under stations alter.

ii. In this dissertation, it is assumed that piers are fully fixed at bases and the ground layer under supports is fairly firm. The proposed model in this study does not explicitly account for the interaction of the foundation with the surrounding soil. the effect of soil-structure interaction is another important aspect that can be considered. A future study can be done for accounting for the effect of the multi-layer soil formation.

iii. The reference bridges used in the parametric study possess a completely symmetrical configuration. The bridge symmetry generates fully symmetrical and anti-symmetrical modes that lead to the above observations. An irregular bridge has only non-symmetric modes. This type of mode can be reshaped in the combination of symmetry and anti-symmetry mode shape using different techniques. The future study can examine the coupling effect of the summation terms on the modal response for irregular mode shape.

iv. In the companion study, the response patterns of the first and second modes have been considered. The future study can implement the proposed model to address the effect of higher modes for the bridges subjected to multi-support excitation.

v. This study demonstrated that the Methodology of the comparison of Dynamic bridge response between MSE and ISE cases should be treated differently. The observation from the parametric study drew a contrary conclusion compared to other studies. The proposed models and conclusions can be implemented in commercial codes.

vi. In this study, we explore pier deformation in the transverse direction. However, the excitation in the longitudinal direction would affect the actual dynamic response. The next study should be done for the evaluation of the vectorial sum of the response in two orthogonal directions.

Appendix A. *Expansion of a sum of n complex numbers*

Consider z_r, the sum of n complex numbers:

$$\begin{aligned} z_r &= \sum_{i=1}^{n} a_{ir} e^{\mathrm{i}\theta_{iq}} = \sum_{i=1}^{n} a_{ir}\cos\left(\theta_{ir}\right) + \mathrm{i}a_{ir}\sin\left(\theta_{ir}\right) \\ &= \sum_{i=1}^{n} a_{ir}c_{ir} + \mathrm{i}\sum_{i=1}^{n} a_{ir}s_{ir} = A_r + \mathrm{i}B_r \end{aligned} \tag{A.1}$$

The modulus/amplitude of this sum is

$$\begin{aligned} \left|z_r\right|^2 &= \left(\sum_{i=1}^{n} a_{ir}c_{ir}\right)^2 + \left(\sum_{i=1}^{n} a_{ir}s_{ir}\right)^2 \\ &= \left\{\begin{matrix} a_{1r}^2c_{1r}^2 + a_{2r}^2c_{2r}^2 + \cdots \\ +a_{1r}^2s_{1r}^2 + a_{2r}^2s_{2r}^2 + \cdots \end{matrix}\right\} + 2\left\{\begin{matrix} a_{1r}c_{1r}a_{2r}c_{2r} + a_{1r}c_{1r}a_{3r}c_{3r} + \cdots \\ +a_{1r}s_{1r}a_{2r}s_{2r} + a_{1r}s_{1r}a_{3r}s_{3r} + \cdots \end{matrix}\right\} \\ &= \sum_{i=1}^{n} a_{ir}^2 + 2\sum_{j=1}^{n-1}\sum_{i=j+1}^{n} a_{ir}a_{jr}\cos\left(\theta_{jr} - \theta_{ir}\right) \end{aligned} \tag{A.2}$$

The argument/phase of this sum, $\zeta_r = \arg\left(A_r + iB_r\right)$, cannot be simplified.

Appendix B. *3 dof formulation of 4 span bridge test case*

A set of 4th order Lagrangian interpolating function for both the ground and deck deformation Ritz vectors defined below.

$$\boldsymbol{\psi} = \boldsymbol{\psi}_g = \begin{bmatrix} \frac{(\xi-1)(\xi-2)(\xi-3)(\xi-4)}{24} \\ \frac{\xi(\xi-1)(\xi-2)(\xi-3)}{24} \\ -\frac{\xi(\xi-2)(\xi-3)(\xi-4)}{6} \\ \frac{\xi(\xi-1)(\xi-3)(\xi-4)}{4} \\ -\frac{\xi(\xi-1)(\xi-2)(\xi-4)}{6} \end{bmatrix}, \quad \mathbf{u}_d = \begin{bmatrix} u_{d,1}=g_1 \\ u_{d,5}=g_5 \\ u_{d,2} \\ u_{d,3} \\ u_{d,4} \end{bmatrix}, \quad \mathbf{u}_g = \begin{bmatrix} g_1 \\ g_5 \\ g_2 \\ g_3 \\ g_4 \end{bmatrix}, \tag{B.1}$$

Thus, the number ground dofs n is the same as the number deck dofs m. After partitioning the system condenses to a 3dof system i.e. u_2 to u_4. Using the symbolic algebra toolbox in Matlab the system matrices can be determined.

$$\mathbf{M}_d = \left[\begin{array}{ccc:cc} 0.206 & -0.020 & 0.209 & -0.123 & 0.040 \\ -0.020 & 0.206 & 0.040 & -0.123 & 0.209 \\ \hdashline 0.209 & 0.040 & 1.264 & -0.271 & 0.181 \\ -0.123 & -0.123 & -0.271 & 1.321 & -0.271 \\ 0.040 & 0.209 & 0.181 & -0.271 & 1.264 \end{array}\right], \mathbf{K}_d = \left[\begin{array}{cc:ccc} 4.117 & 1.450 & -11.467 & 12.033 & -6.133 \\ 1.450 & 4.117 & -6.133 & 12.033 & -11.467 \\ \hdashline -11.467 & -6.133 & 35.200 & -42.133 & 24.533 \\ 12.033 & 12.033 & -42.133 & 60.200 & -42.133 \\ -6.133 & -11.467 & 24.533 & -42.133 & 35.200 \end{array}\right]$$

$$\mathbf{K}_g = \mathbf{K}_{gg} = \left[\begin{array}{cc:ccc} \eta_1 & 0 & 0 & 0 & 0 \\ 0 & \eta_5 & 0 & 0 & 0 \\ \hdashline 0 & 0 & \eta_2 & 0 & 0 \\ 0 & 0 & 0 & \eta_3 & 0 \\ 0 & 0 & 0 & 0 & \eta_4 \end{array}\right] \tag{B.2}$$

Appendix C. *7 dof formulation of 4 span bridge test case*

A set of 8th order Lagrangian interpolating function for deck deformations Ritz vector $\boldsymbol{\psi}$ and a 4th order for the ground Lagrangian interpolating function Ritz vector $\boldsymbol{\psi}_g$ show below:

$$\boldsymbol{\psi} = \begin{bmatrix} \frac{2(\xi-1)(\xi-2)(\xi-3)\left(\xi-\frac{1}{2}\right)(\xi-4)\left(\xi-\frac{3}{2}\right)\left(\xi-\frac{5}{2}\right)\left(\xi-\frac{7}{2}\right)}{315} \\ \frac{2\xi(\xi-1)(\xi-2)(\xi-3)\left(\xi-\frac{1}{2}\right)\left(\xi-\frac{3}{2}\right)\left(\xi-\frac{5}{2}\right)\left(\xi-\frac{7}{2}\right)}{315} \\ -\frac{16\xi(\xi-1)(\xi-2)(\xi-3)(\xi-4)\left(\xi-\frac{3}{2}\right)\left(\xi-\frac{5}{2}\right)\left(\xi-\frac{7}{2}\right)}{315} \\ \frac{8\xi(\xi-2)(\xi-3)\left(\xi-\frac{1}{2}\right)(\xi-4)\left(\xi-\frac{3}{2}\right)\left(\xi-\frac{5}{2}\right)\left(\xi-\frac{7}{2}\right)}{45} \\ -\frac{16\xi(\xi-1)(\xi-2)(\xi-3)\left(\xi-\frac{1}{2}\right)(\xi-4)\left(\xi-\frac{5}{2}\right)\left(\xi-\frac{7}{2}\right)}{45} \\ \frac{4\xi(\xi-1)(\xi-3)\left(\xi-\frac{1}{2}\right)(\xi-4)\left(\xi-\frac{3}{2}\right)\left(\xi-\frac{5}{2}\right)\left(\xi-\frac{7}{2}\right)}{9} \\ -\frac{16\xi(\xi-1)(\xi-2)(\xi-3)\left(\xi-\frac{1}{2}\right)(\xi-4)\left(\xi-\frac{3}{2}\right)\left(\xi-\frac{7}{2}\right)}{45} \\ \frac{8\xi(\xi-1)(\xi-2)\left(\xi-\frac{1}{2}\right)(\xi-4)\left(\xi-\frac{3}{2}\right)\left(\xi-\frac{5}{2}\right)\left(\xi-\frac{7}{2}\right)}{45} \\ -\frac{16\xi(\xi-1)(\xi-2)(\xi-3)\left(\xi-\frac{1}{2}\right)(\xi-4)\left(\xi-\frac{3}{2}\right)\left(\xi-\frac{5}{2}\right)}{315} \end{bmatrix}, \boldsymbol{\psi}_g = \begin{bmatrix} \frac{(\xi-1)(\xi-2)(\xi-3)(\xi-4)}{24} \\ \frac{\xi(\xi-1)(\xi-2)(\xi-3)}{24} \\ -\frac{\xi(\xi-2)(\xi-3)(\xi-4)}{6} \\ \frac{\xi(\xi-1)(\xi-3)(\xi-4)}{4} \\ -\frac{\xi(\xi-1)(\xi-2)(\xi-4)}{6} \end{bmatrix}, \mathbf{u}_d = \begin{bmatrix} u_{d,1}=g_1 \\ u_{d,9}=g_5 \\ u_{d,2} \\ u_{d,3} \\ u_{d,4} \\ u_{d,5} \\ u_{d,6} \\ u_{d,7} \\ u_{d,8} \end{bmatrix}, \mathbf{u}_g = \begin{bmatrix} g_1 \\ g_5 \\ g_2 \\ g_3 \\ g_4 \end{bmatrix}, \tag{C.1}$$

Thus, the number ground dofs n is less than the number of deck dofs m. After partitioning the system condenses to a 7dof system, i.e. u_2 to u_8. Using the symbolic algebra toolbox in Matlab the system matrices can be determined.

$$\mathbf{M} = \begin{bmatrix} 0.083 & -0.003 & 0.142 & -0.202 & 0.251 & -0.225 & 0.137 & -0.052 & 0.009 \\ -0.003 & 0.083 & 0.009 & -0.052 & 0.137 & -0.225 & 0.251 & -0.202 & 0.142 \\ 0.142 & 0.009 & 0.945 & -0.752 & 0.978 & -0.926 & 0.622 & -0.294 & 0.106 \\ -0.202 & -0.052 & -0.752 & 1.700 & -1.582 & 1.571 & -1.149 & 0.628 & -0.294 \\ 0.251 & 0.137 & 0.978 & -1.582 & 2.690 & -2.330 & 1.864 & -1.149 & 0.622 \\ -0.225 & -0.225 & -0.926 & 1.571 & -2.330 & 3.178 & -2.330 & 1.571 & -0.926 \\ 0.137 & 0.251 & 0.622 & -1.149 & 1.864 & -2.330 & 2.690 & -1.582 & 0.978 \\ -0.052 & -0.202 & -0.294 & 0.628 & -1.149 & 1.571 & -1.582 & 1.700 & -0.752 \\ 0.009 & 0.142 & 0.106 & -0.294 & 0.622 & -0.926 & 0.978 & -0.752 & 0.945 \end{bmatrix} \tag{C.2}$$

$$\mathbf{K} = \frac{1}{1000}\begin{bmatrix} 0.073 & 0.010 & -0.296 & 0.600 & -0.819 & 0.796 & -0.538 & 0.246 & -0.071 \\ 0.010 & 0.073 & -0.071 & 0.246 & -0.538 & 0.796 & -0.819 & 0.600 & -0.296 \\ -0.296 & -0.071 & 1.287 & -2.743 & 3.874 & -3.880 & 2.740 & -1.339 & 0.429 \\ 0.600 & 0.246 & -2.743 & 6.163 & -9.115 & 9.561 & -7.154 & 3.783 & -1.339 \\ -0.819 & -0.538 & 3.874 & -9.115 & 14.221 & -15.783 & 12.575 & -7.154 & 2.740 \\ 0.796 & 0.796 & -3.880 & 9.561 & -15.783 & 18.612 & -15.783 & 9.561 & -3.880 \\ -0.538 & -0.819 & 2.740 & -7.154 & 12.575 & -15.783 & 14.221 & -9.115 & 3.874 \\ 0.246 & 0.600 & -1.339 & 3.783 & -7.154 & 9.561 & -9.115 & 6.163 & -2.743 \\ -0.071 & -0.296 & 0.429 & -1.339 & 2.740 & -3.880 & 3.874 & -2.743 & 1.287 \end{bmatrix} \tag{C.3}$$

$$\mathbf{K}_g = \begin{bmatrix} \eta_1 & 0 & 0 & 0 & 0 \\ 0 & \eta_5 & 0 & 0 & 0 \\ 0 & 0 & 0 & 0 & 0 \\ 0 & 0 & \eta_2 & 0 & 0 \\ 0 & 0 & 0 & 0 & 0 \\ 0 & 0 & 0 & \eta_3 & 0 \\ 0 & 0 & 0 & 0 & 0 \\ 0 & 0 & 0 & 0 & \eta_4 \\ 0 & 0 & 0 & 0 & 0 \end{bmatrix}, \quad \mathbf{K}_{gg} = \begin{bmatrix} \eta_1 & 0 & 0 & 0 & 0 \\ 0 & \eta_5 & 0 & 0 & 0 \\ 0 & 0 & \eta_2 & 0 & 0 \\ 0 & 0 & 0 & \eta_3 & 0 \\ 0 & 0 & 0 & 0 & \eta_4 \end{bmatrix} \tag{C.4}$$

Appendix D. *Curve fitting of the experimental bridge model*

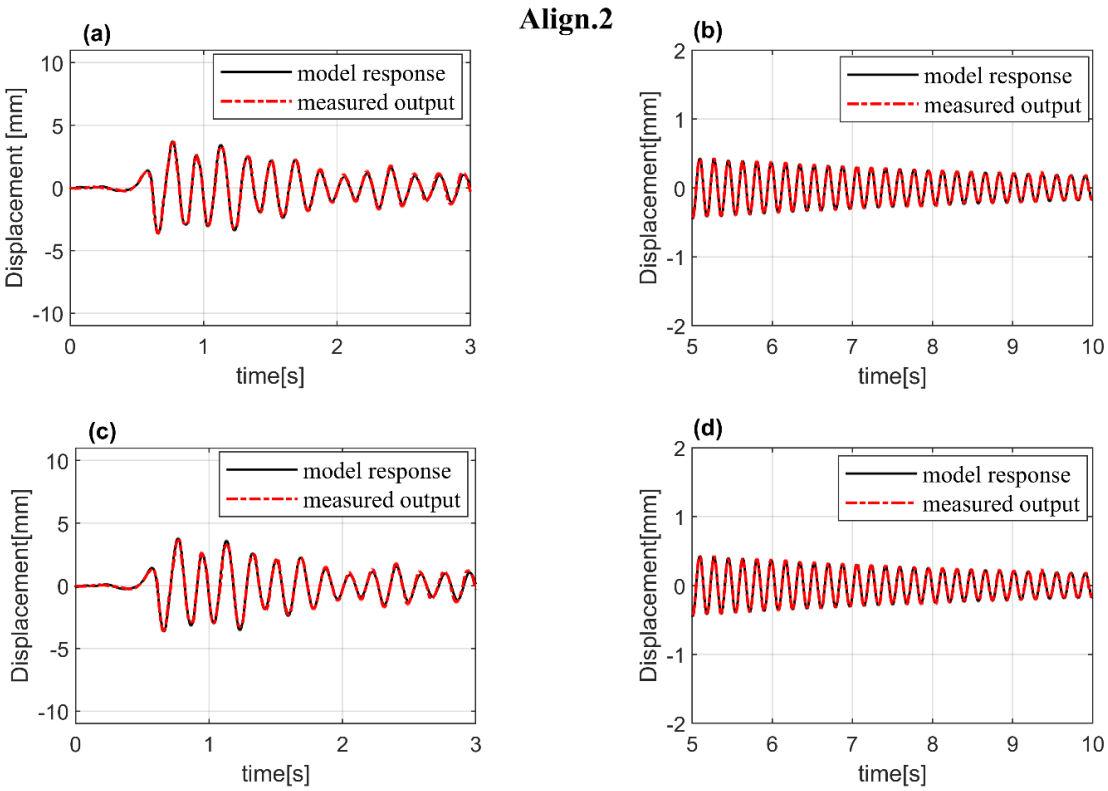

Figure 51; Result of curve fitting of experimental bridge model, alignment C00-I02. (a) 7-Dof system under multi-support excitation, (b) 7-Dof system under free-vibration, (c) 3-Dof system under multi-support excitation and (d) 3-Dof system under free-vibration.

Align.4

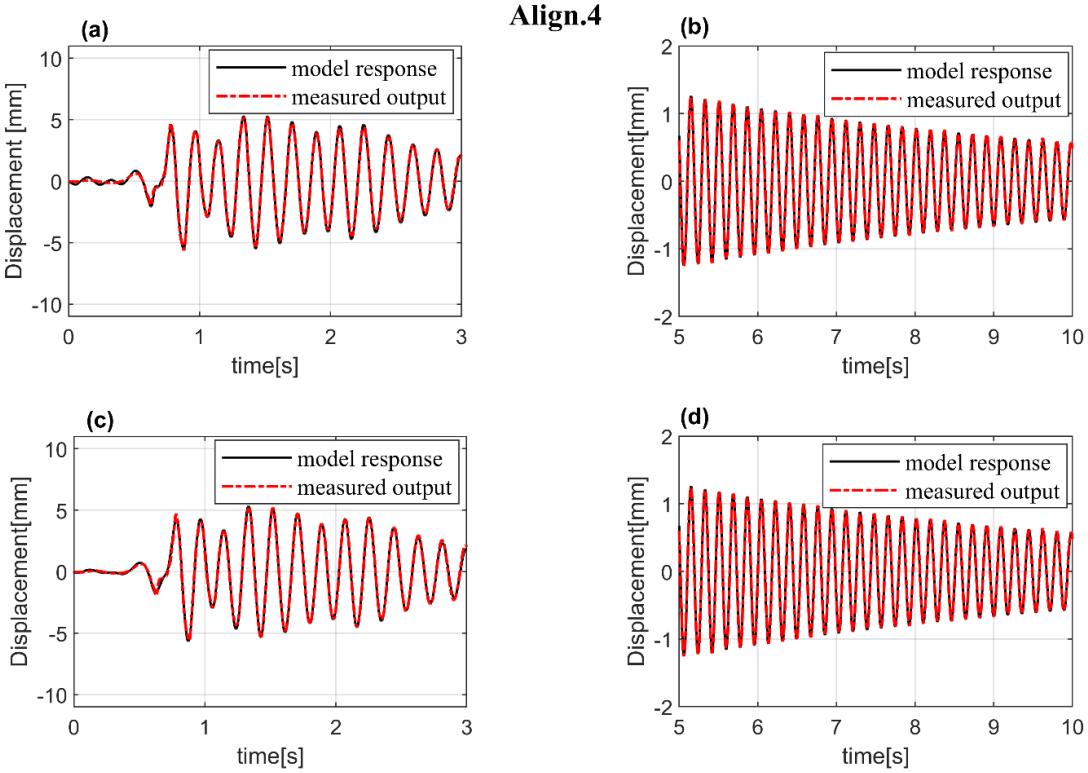

Figure 52; Result of curve fitting of experimental bridge model, alignment C00-I04. (a) 7-Dof system under multi-support excitation, (b) 7-Dof system under free-vibration, (c) 3-Dof system under multi-support excitation, and (d) 3-Dof system under free-vibration.

Align.7

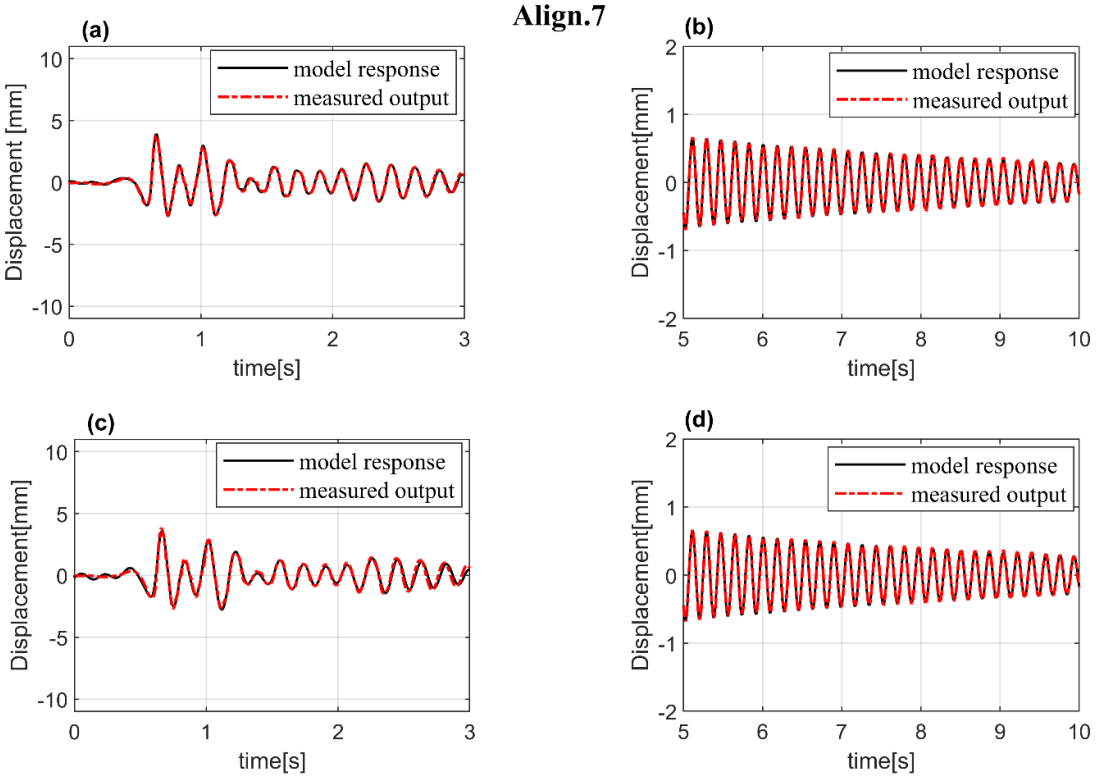

Figure 53;Result of curve fitting of experimental bridge model, alignment C00-I07. (a) 7-Dof system under multi-support excitation, (b) 7-Dof system under free-vibration, (c) 3-Dof system under multi-support excitation and (d) 3-Dof system under free-vibration.

Align.8

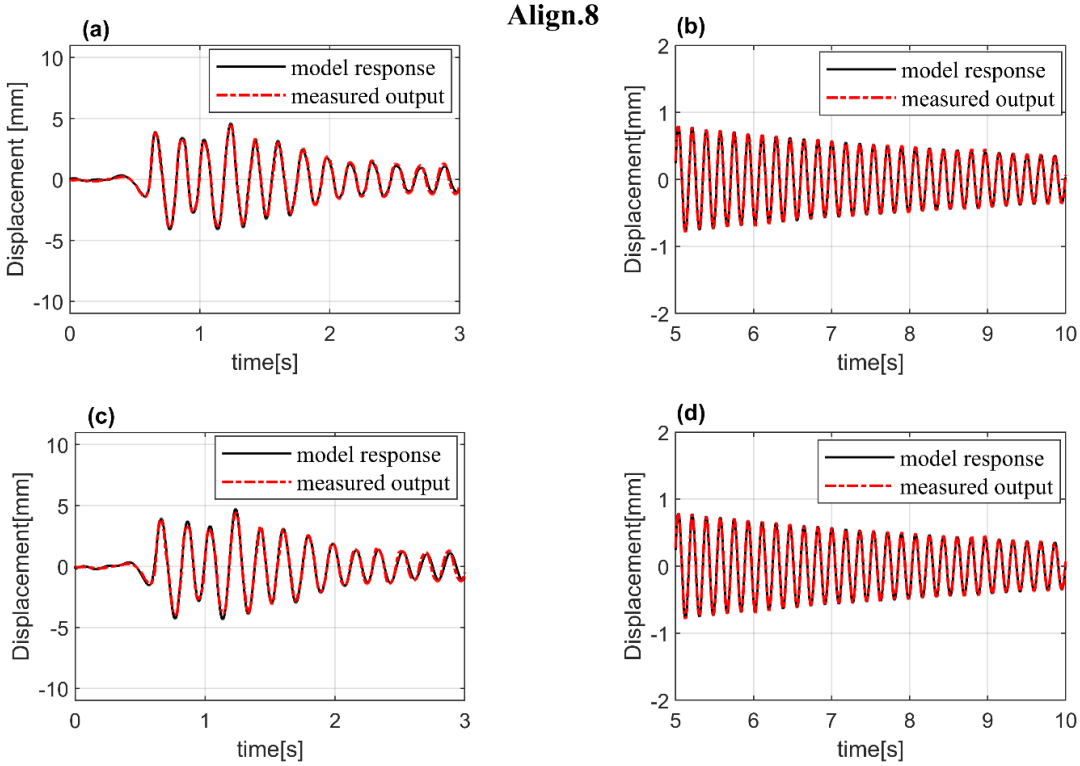

Figure 54; Result of curve fitting of experimental bridge model, alignment C00-I08. (a) 7-Dof system under multi-support excitation, (b) 7-Dof system under free-vibration, (c) 3-Dof system under multi-support excitation, and (d) 3-Dof system under free-vibration.

Align.9

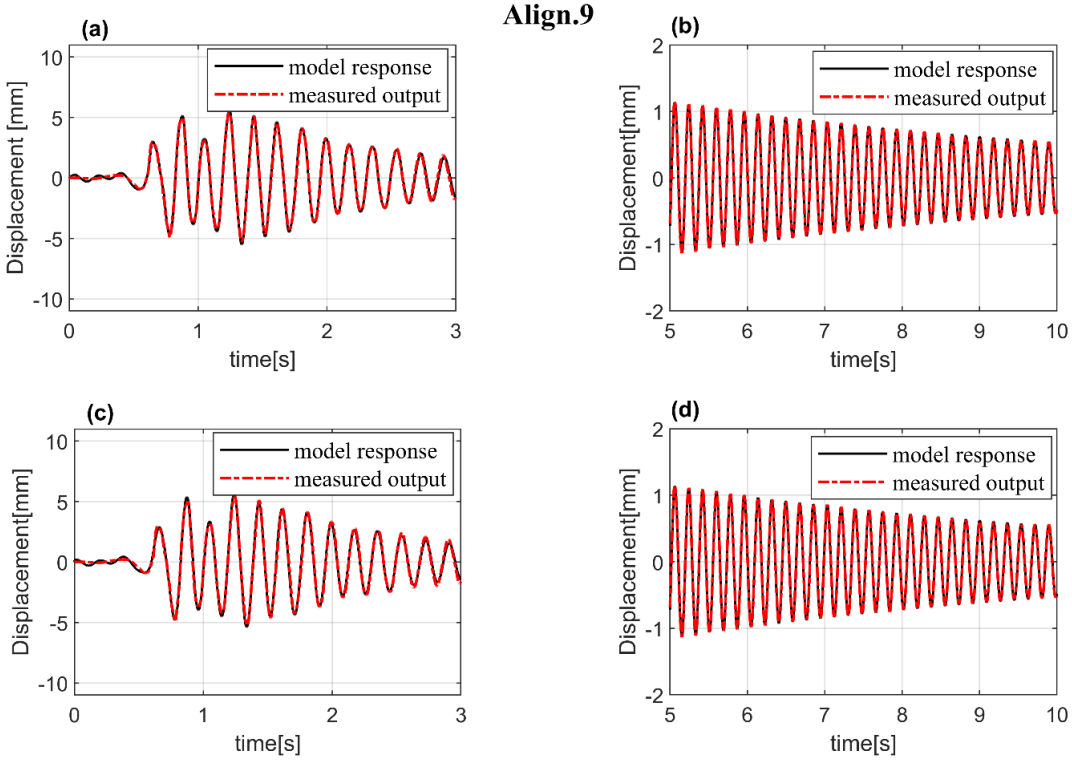

Figure 55; Result of curve fitting of experimental bridge model, alignment C00-I09. (a) 7-Dof system under multi-support excitation, (b) 7-Dof system under free-vibration, (c) 3-Dof system under multi-support excitation, and (d) 3-Dof system under free-vibration.

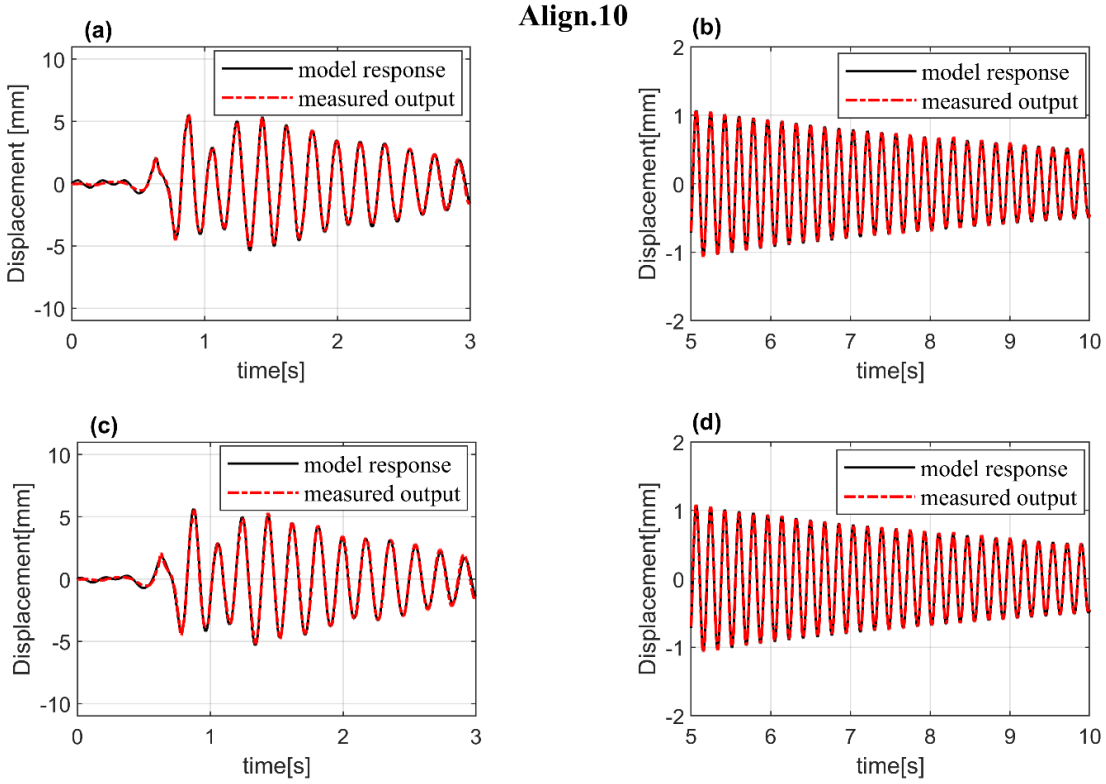

Figure 56; Result of curve fitting of experimental bridge model, alignment C00-I10. (a) 7-Dof system under multi-support excitation, (b) 7-Dof system under free-vibration, (c) 3-Dof system under multi-support excitation, and (d) 3-Dof system under free-vibration.

Align.11

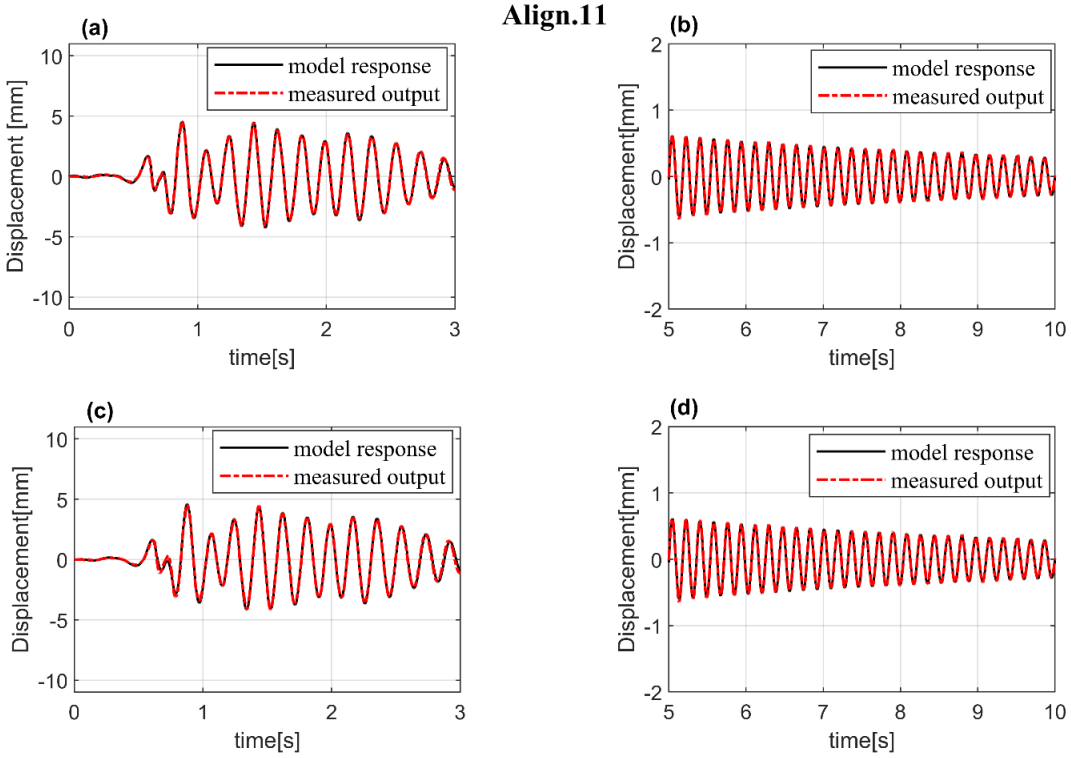

Figure 57; Result of curve fitting of experimental bridge model, alignment C00-I11. (a) 7-Dof system under multi-support excitation, (b) 7-Dof system under free-vibration, (c) 3-Dof system under multi-support excitation, and (d) 3-Dof system under free-vibration.

Align.12

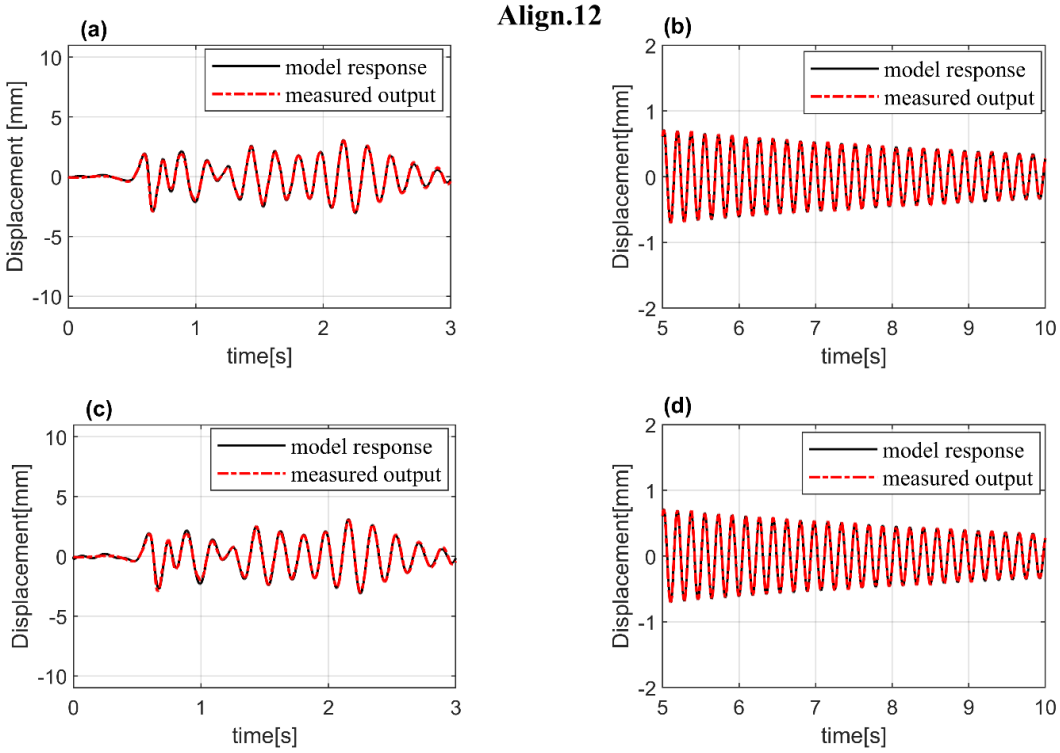

Figure 58; Result of curve fitting of experimental bridge model, alignment C00-I12. (a) 7-Dof system under multi-support excitation, (b) 7-Dof system under free-vibration, (c) 3-Dof system under multi-support excitation, and (d) 3-Dof system under free-vibration.

Appendix E. *Explicit state space form for prototype bridge system*

In order to solve the proposed mathematical model, the nonlinear differential equation of motion is represented in the first-order state-space framework. it is necessary to reduce the second-order differential equation to the first order indenting to use a numerical algorithm. To achieve this goal, the state vector is defined as:

$$\mathbf{x} = \begin{bmatrix} \mathbf{w} \\ \dot{\mathbf{w}} \end{bmatrix} \tag{E.1}$$

Therefore, by substituting of the above state vector in Eq(3.32), State-space models for the adopted dynamical system would take form as:

$$\dot{\mathbf{x}} = \mathbf{B}_1\,\mathbf{x} + \mathbf{B}_2\,\mathbf{z}_l + \mathbf{B}_3\,\mathbf{f} \tag{E.2}$$

$$\mathbf{B}_1 = \begin{bmatrix} \mathbf{0} & \mathbf{I} \\ -\mathbf{M}_{22}^{-1}(\mathbf{K}_{d22} + \mathbf{K}_{u22}) & -\mathbf{M}_{22}^{-1}\mathbf{C} \end{bmatrix}, \quad \mathbf{B}_2 = \begin{bmatrix} \mathbf{0} \\ -\mathbf{M}_{22}^{-1}\,\mathbf{K}_{z22} \end{bmatrix}$$
$$\mathbf{B}_3 = \begin{bmatrix} \mathbf{0} & \mathbf{0} & \mathbf{0} & \mathbf{0} \\ -\mathbf{M}_{22}^{-1}\,\mathbf{L}_{12}^{T} & -\mathbf{M}_{22}^{-1}\,\mathbf{L}_{22} & -\mathbf{M}_{22}^{-1}\,\mathbf{K}_{g12}^{T} & -\mathbf{M}_{22}^{-1}\,\mathbf{K}_{g22} \end{bmatrix} \tag{E.3}$$

where the ground motion input vector $\mathbf{f}(t) = [\ddot{\mathbf{g}}_E; \ddot{\mathbf{g}}_I; \mathbf{g}_E; \mathbf{g}_I]$, and $\mathbf{z}_l(t)$ is the state vector representing hysteretic displacement at piers. For the proposed bridge system in this study, 4th order Lagrangian interpolating function is used to define the shape function of both ground and deck DOFs as:

$$\mathbf{M}=\begin{bmatrix} 0.206 & 0.209 & -0.123 & 0.0395 & -0.0205 \\ 0.209 & 1.26 & -0.271 & 0.181 & 0.0395 \\ -0.123 & -0.271 & 1.32 & -0.271 & -0.123 \\ 0.0395 & 0.181 & -0.271 & 1.26 & 0.209 \\ -0.0205 & 0.0395 & -0.123 & 0.209 & 0.206 \end{bmatrix},\quad \mathbf{K}_d=\begin{bmatrix} 103.0 & -287.0 & 301.0 & -153.0 & 36.2 \\ -287.0 & 880.0 & -1066.0 & 613.0 & -153.0 \\ 301.0 & -1066.0 & 1500.0 & -1066.0 & 301.0 \\ -153.0 & 613.0 & -1066.0 & 880.0 & -287.0 \\ 36.2 & -153.0 & 301.0 & -287.0 & 103.0 \end{bmatrix},$$

$$\frac{\mathbf{K}_u}{\alpha}=\frac{\mathbf{K}_z}{1-\alpha}=\mathbf{K}_g=\begin{bmatrix} 0 & 0 & 0 & 0 & 0 \\ 0 & 0 & 0 & 0 & 0 \\ 0 & 0 & \eta_1 & 0 & 0 \\ 0 & 0 & 0 & \eta_2 & 0 \\ 0 & 0 & 0 & 0 & \eta_3 \end{bmatrix},\quad \mathbf{L}=\begin{bmatrix} 0.206 & 0.209 & -0.123 & 0.0395 & -0.0205 \\ 0.209 & 1.26 & -0.271 & 0.181 & 0.0395 \\ -0.123 & -0.271 & 1.32 & -0.271 & -0.123 \\ 0.0395 & 0.181 & -0.271 & 1.26 & 0.209 \\ -0.0205 & 0.0395 & -0.123 & 0.209 & 0.206 \end{bmatrix} \tag{E.4}$$

Where $\mathbf{M}$ is the mass matrix and $\mathbf{K}_u, \mathbf{K}_z, \mathbf{K}_g$ denote the pier, the hysteretic and the ground stiffness matrix respectively. $\mathbf{L}$ is denominated in this study as the excitation factor matrix. The imaginary hysteresis displacements in $\mathbf{z}_l(t)$ are determined from following auxiliary ordinary differential equation for the studied bridge.

$$\begin{bmatrix} \dot{z}_1 \\ \dot{z}_2 \\ \dot{z}_3 \end{bmatrix}=\begin{bmatrix} \dfrac{1}{1+0.3\epsilon_1}\left\{1-\left(1+0.05\epsilon_1\right)\left(0.5\,\mathrm{sgn}(\dot{u}_1 z_1)+0.5\right)\left|z_1\right|\right\}\dfrac{\dot{u}_1}{u_{y1}} \\ \dfrac{1}{1+0.3\epsilon_2}\left\{1-\left(1+0.05\epsilon_2\right)\left(0.5\,\mathrm{sgn}(\dot{u}_2 z_2)+0.5\right)\left|z_2\right|\right\}\dfrac{\dot{u}_2}{u_{y2}} \\ \dfrac{1}{1+0.3\epsilon_3}\left\{1-\left(1+0.05\epsilon_3\right)\left(0.5\,\mathrm{sgn}(\dot{u}_3 z_3)+0.5\right)\left|z_3\right|\right\}\dfrac{\dot{u}_3}{u_{y3}} \end{bmatrix} \tag{E.5}$$

References

ABDEL-GHAFFAR, A. M. & RUBIN, L. I. 1982. Suspension bridge response to multiple-support excitations. *Journal of the engineering mechanics division,* 108**,** 419-435.

ABRAHAMSON, N., BOLT, B., DARRAGH, R., PENZIEN, J. & TSAI, Y. 1987. The SMART I accelerograph array (1980-1987): a review. *Earthquake spectra,* 3**,** 263-287.

ABRAHAMSON, N., SCHNEIDER, J. & STEPP, J. 1991. Empirical spatial coherency functions for application to soil-structure interaction analyses. *Earthquake spectra,* 7**,** 1-27.

AHMADI-KASHANI, K. Seismic design of Egnatia motorway bridges, Greece. Proceedings of the Institution of Civil Engineers-Bridge Engineering, 2004. Thomas Telford Ltd, 83-91.

ALEXANDER, N., CHANERLEY, A. & GOORVADOO, N. A review of procedures used for the correction of seismic data. Sept 19th-21st, 2001, Eisenstadt-Vienna, Austria, Proc of the 8th International Conference on Civil & Structural Engineering ISBN 0-948749-75-X, 2001.

ALEXANDER, N., NORMAN, J., VIRDEN, D., CREWE, A., WAGG, D. & CHANERLEY, A. Effects of orientation to the epicentre on the response of long span bridges subject to multiple support excitation using SMART-1 array data and corroborative experimental results. Proc. 8th Nat. Conf. on Earthquake Eng, 2006. Citeseer.

ALEXANDER, N. A. 2008. Multi-support excitation of single span bridges, using real seismic ground motion recorded at the SMART-1 array. *Computers & structures,* 86**,** 88-103.

ALVIN, K., ROBERTSON, A., REICH, G. & PARK, K. 2003. Structural system identification: from reality to models. *Computers & structures,* 81**,** 1149-1176.

AMERICAN SOCIETY OF CIVIL, E. 1987. *Seismic Analysis of Safety-related Nuclear Structures, and Commentary on Standard for Seismic Analysis of Safety Related Nuclear Structures*, American Society of Civil Engineers.

ATALIK, T. S. & UTKU, S. 1976. Stochastic linearization of multi-degree-of-freedom non-linear systems. *Earthquake Engineering & Structural Dynamics,* 4**,** 411-420.

BARDAKIS, V. G. & FARDIS, M. N. 2011. Nonlinear dynamic v elastic analysis for seismic deformation demands in concrete bridges having deck integral with the piers. *Bulletin of Earthquake Engineering,* 9**,** 519-535.

BI, K., HAO, H. & CHOUW, N. 2011. Influence of ground motion spatial variation, site condition and SSI on the required separation distances of bridge structures to avoid seismic pounding. *Earthquake Engineering & Structural Dynamics,* 40**,** 1027-1043.

BOGDANOFF, J., GOLDBERG, J. & SCHIFF, A. 1965. The effect of ground transmission time on the response of long structures. *Bulletin of the Seismological Society of America,* 55**,** 627-640.

BOUC, R. Forced vibrations of mechanical systems with hysteresis. Proc. of the Fourth Conference on Nonlinear Oscillations, Prague, 1967, 1967.

BSI 2005. EN 1998-2:2005. Eurocode 8: Design of structures for earthquake resistance – Part 2: Bridges. Brussels: CEN.

BYCROFT, G. N. 1980. El Centro, California, differential ground motion array. US Geological Survey.

CAMARA, A. & ASTIZ, M. 2012. Pushover analysis for the seismic response prediction of cable-stayed bridges under multi-directional excitation. *Engineering Structures,* 41**,** 444-455.

CAMARA, A., ASTIZ, M. & YE, A. 2014. Fundamental mode estimation for modern cable-stayed bridges considering the tower flexibility. *Journal of Bridge Engineering,* 19**,** 04014015.

CHANERLEY, A. & ALEXANDER, N. 2007. Correcting data from an unknown accelerometer using recursive least squares and wavelet de-noising. *Computers & Structures,* 85**,** 1679-1692.

CHANERLEY, A. & ALEXANDER, N. 2008. Using the total least squares method for seismic correction of recordings from unknown instruments. *Advances in Engineering Software,* 39**,** 849-860.

CHANERLEY, A. & ALEXANDER, N. 2010. Obtaining estimates of the low-frequency 'fling', instrument tilts and displacement timeseries using wavelet decomposition. *Bulletin of earthquake engineering,* 8**,** 231-255.

CHARALAMPAKIS, A. & KOUMOUSIS, V. 2006. Parameter estimation of Bouc-Wen hysteretic systems using a Sawtooth Genetic Algorithm.

CHOPRA, A. K. 2007. *Dynamics of structures: theory and applications to earthquake engineering*, Pearson/Prentice Hall Upper Saddle River, NJ.

CLOUGH, R. W. & PENZIEN, J. 1995. Dynamics of Structures. Berkeley: Computers & Structures. Inc.

CREWE, A. J. & NORMAN, J. A. Experimental modelling of multiple support excitation of long span bridges. Proceedings of the 4th international conference on earthquake engineering, 2006.

DER KIUREGHIAN, A. 1996. A coherency model for spatially varying ground motions. *Earthquake Engineering & Structural Dynamics,* 25**,** 99-111.

DER KIUREGHIAN, A., KESHISHIAN, P. & HAKOBIAN, A. 1997. Multiple support response spectrum analysis of bridges including the site-response effect and the MSRS code.

DIANA, T. 2010. DIANA user's manual, analysis procedures. *TNO DIANA bv, Delft Google Scholar*.

DING, Y., LIN, W. & LI, Z.-X. 2007. Non-stationary Random Seismic Analysis of Long-span Spatial Structures under Multi-support and Multi-dimensional Earthquake Excitations [J]. *Engineering mechanics,* 3**,** 97-101.

DUSSEAU, R. A. & DUBAISI, H. N. 1993. *Natural frequencies of concrete bridges in*

the Pacific Northwest.

DWAIRI, H. & KOWALSKY, M. 2006. Implementation of inelastic displacement patterns in direct displacement-based design of continuous bridge structures. *Earthquake Spectra,* 22**,** 631-662.

FAJFAR, P. 2000. A nonlinear analysis method for performance-based seismic design. *Earthquake spectra,* 16**,** 573-592.

FARDIS, M. N. 2005. *Designers' guide to EN 1998-1 and EN 1998-5 Eurocode 8: design of structures for earthquake resistance: general rules, seismic actions, design rules for buildings, foundations and retaining structures*, Thomas Telford Services Limited.

GIARALIS, A. & SPANOS, P. D. 2013. Derivation of equivalent linear properties of Bouc-Wen hysteretic systems for seismic response spectrum analysis via statistical linearization.

GODA, K., HONG, H. & LEE, C. 2009. Probabilistic characteristics of seismic ductility demand of SDOF systems with Bouc-Wen hysteretic behavior. *Journal of Earthquake Engineering,* 13**,** 600-622.

GRUBER, M. H. 1997. Statistical digital signal processing and modeling. Taylor & Francis Group.

GULKAN, P. & SOZEN, M. A. Inelastic responses of reinforced concrete structure to earthquake motions. Journal Proceedings, 1974. 604-610.

GUYADER, A. C. & IWAN, W. D. 2006a. Determining equivalent linear parameters for use in a capacity spectrum method of analysis. *Journal of Structural Engineering,* 132**,** 59-67.

GUYADER, A. C. & IWAN, W. D. J. J. O. S. E. 2006b. Determining equivalent linear parameters for use in a capacity spectrum method of analysis. 132**,** 59-67.

HAHN, G. & LIU, X. 1994. Torsional response of unsymmetric buildings to incoherent ground motions. *Journal of Structural Engineering,* 120**,** 1158-1181.

HAO, H. 1991. Response of multiply supported rigid plate to spatially correlated seismic excitations. *Earthquake engineering & structural dynamics,* 20**,** 821-838.

HAO, H. & DUAN, X. 1995. Seismic response of asymmetric structures to multiple ground motions. *Journal of structural engineering,* 121**,** 1557-1564.

HAO, H., OLIVEIRA, C. & PENZIEN, J. 1989. Multiple-station ground motion processing and simulation based on SMART-1 array data. *Nuclear Engineering and Design,* 111**,** 293-310.

HARICHANDRAN, R. S., HAWWARI, A. & SWEIDAN, B. N. 1996. Response of long-span bridges to spatially varying ground motion. *Journal of Structural Engineering,* 122**,** 476-484.

HARICHANDRAN, R. S. & VANMARCKE, E. H. 1986. Stochastic variation of earthquake ground motion in space and time. *Journal of Engineering Mechanics,* 112**,** 154-174.

HILTON, P. J. 1958. *Differential calculus,* London

Routledge & K. Paul.

IBRAHIM, S. R. 2002. A time domain vibration test technique.

IES 1980- 1990. SMART-1 Array data repository Taiwan: Institute of Earth Science

IWAN, W. 1980. Estimating inelastic response spectra from elastic spectra. *Earthquake Engineering & Structural Dynamics,* 8**,** 375-388.

JOHNSON, N. & GALLETLY, R. 1972. The comparison of the response of a highway bridge to uniform ground shock and moving ground excitation. *Shock vib. bull,* 42**,** 75-85.

JOYNER, W. B. & BOORE, D. M. 1981. Peak horizontal acceleration and velocity from strong-motion records including records from the 1979 Imperial Valley, California, earthquake. *Bulletin of the Seismological Society of America,* 71**,** 2011-2038.

KAPPOS, A. J. 2010. Current Trends in the Seismic Design and Assessment of Buildings. *Earthquake Engineering in Europe.* Springer.

KASHANI, M. M., GE, X., DIETZ, M. S., CREWE, A. J. & ALEXANDER, N. A. 2019. Significance of non-stationary characteristics of ground-motion on structural damage: shaking table study. *Bulletin of Earthquake Engineering***,** 1-23.

KAWASHIMA, K. & UNJOH, S. 2004. Seismic design of highway bridges. *Journal of Japan Association for Earthquake Engineering,* 4**,** 174-183.

KAZAKOV, I. 1966a. Generalization of the method of statistical linearization to multidimensional systems(Generalized statistical linearization method for multivariable systems and arbitrary periodic and random signal effect on nonlinear automatic system). *Automation and Remote control,* 26**,** 1201-1206.

KAZAKOV, I. E. 1966b. Generalization of the method of statistical linearization to multidimensional systems(Generalized statistical linearization method for multivariable systems and arbitrary periodic and random signal effect on nonlinear automatic system). *Automation and Remote control,* 26**,** 1201-1206.

KIUREGHIAN, A. D. & NEUENHOFER, A. 1992. Response spectrum method for multi-support seismic excitations. *Earthquake Engineering & Structural Dynamics,* 21**,** 713-740.

KONAKLI, A. 2011. *Stochastic dynamic analysis of bridges subjected to spatially varying ground motions.* UC Berkeley.

KONAKLI, K. & DER KIUREGHIAN, A. 2014. Investigation of 'equal displacement'rule for bridges subjected to differential support motions. *Earthquake Engineering & Structural Dynamics,* 43**,** 23-39.

KOUGIOUMTZOGLOU, I. A. & SPANOS, P. D. 2013. Nonlinear MDOF system stochastic response determination via a dimension reduction approach. *Computers & Structures,* 126**,** 135-148.

KOWALSKY, M. J. 2002. A displacement-based approach for the seismic design of continuous concrete bridges. *Earthquake Engineering & Structural Dynamics,* 31**,** 719-747.

KUNNATH, S. K., MANDER, J. B. & FANG, L. 1997. Parameter identification for

degrading and pinched hysteretic structural concrete systems. *Engineering Structures,* 19**,** 224-232.

LAI, S. S. P. 1982. Statistical characterization of strong ground motions using power spectral density function. *Bulletin of the Seismological Society of America,* 72**,** 259-274.

LAVORATO, D., FIORENTINO, G., BERGAMI, A. V., BRISEGHELLA, B., NUTI, C., SANTINI, S. & VANZI, I. 2018. Asynchronous earthquake strong motion and RC bridges response. *Journal of Traffic and Transportation Engineering (English Edition),* 5**,** 454-466.

LAVORATO, D., VANZI, I., NUTI, C. & MONTI, G. 2017. Generation of Non-synchronous Earthquake Signals. *In:* GARDONI, P. (ed.) *Risk and Reliability Analysis: Theory and Applications: In Honor of Prof. Armen Der Kiureghian.* Cham: Springer International Publishing.

LEE, V. 2002. Empirical scaling of strong earthquake ground motion: part I: attenuation and scaling of response spectra. *ISET Journal of Earthquake Technology,* 39**,** 219-254.

LEE, Y., POON, W. & NG, C. 2006. Anti-symmetric mode vibration of a curved beam subject to autoparametric excitation. *Journal of Sound and Vibration,* 290**,** 48-64.

LEGER, P., IDE, I. & PAULTRE, P. 1990. Multiple-support seismic analysis of large structures. *Computers & Structures,* 36**,** 1153-1158.

LIAO, S. & LI, J. 2002. A stochastic approach to site-response component in seismic ground motion coherency model. *Soil Dynamics and Earthquake Engineering,* 22**,** 813-820.

LIN, J., ZHANG, Y., LI, Q. S. & WILLIAMS, F. W. 2004. Seismic spatial effects for long-span bridges, using the pseudo excitation method. *Engineering Structures,* 26**,** 1207-1216.

LIU, G., LIAN, J., LIANG, C., LI, G. & HU, J. 2016. An improved complex multiple-support response spectrum method for the non-classically damped linear system with coupled damping. *Bulletin of Earthquake Engineering,* 14**,** 161-184.

LJUNG, L. 1987. *System identification: theory for the user*, Prentice-hall.

LJUNG, L. 1995. *System identification toolbox: User's guide*, Citeseer.

LJUNG, L. 2010. Perspectives on system identification. *Annual Reviews in Control,* 34**,** 1-12.

LOH, C.-H. & KU, B.-D. 1995. An efficient analysis of structural response for multiple-support seismic excitations. *Engineering structures,* 17**,** 15-26.

LOH, C.-H. & LIN, S.-G. 1990. Directionality and simulation in spatial variation of seismic waves. *Engineering Structures,* 12**,** 134-143.

LOH, C., PENZIEN, J. & TSAI, Y. 1982. Engineering analyses of SMART 1 array accelerograms. *Earthquake Engineering & Structural Dynamics,* 10**,** 575-591.

LOU, L. & ZERVA, A. 2005. Effects of spatially variable ground motions on the seismic response of a skewed, multi-span, RC highway bridge. *Soil Dynamics and*

Earthquake Engineering, 25**,** 729-740.

LUCO, J. & WONG, H. 1986. Response of a rigid foundation to a spatially random ground motion. *Earthquake Engineering & Structural Dynamics,* 14**,** 891-908.

LUPOI, A., FRANCHIN, P., PINTO, P. & MONTI, G. 2005. Seismic design of bridges accounting for spatial variability of ground motion. *Earthquake engineering & structural dynamics,* 34**,** 327-348.

MA, F., ZHANG, H., BOCKSTEDTE, A., FOLIENTE, G. C. & PAEVERE, P. 2004. Parameter analysis of the differential model of hysteresis. *Journal of Applied Mechanics,* 71**,** 342-349.

MASRI, S. 1976. Response of beams to propagating boundary excitation. *Earthquake Engineering & Structural Dynamics,* 4**,** 497-509.

MEIBODI, A. & ALEXANDER, N. A. 2020. Exploring a generalized nonlinear multi-span bridge system subject to multi-support excitation using a Bouc-Wen hysteretic model. *Soil Dynamics and Earthquake Engineering,* 135**,** 106-160.

MEIBODI, A. A. & ALEXANDER, N. A. 2021. Spatiotemporal seismic excitation of bridges with an anti-symmetrical first mode. *Bulletin of Earthquake Engineering*.

MEIBODI, A. A., ALEXANDER, N. A., NORMAN, J. A. & CREWE, A. J. 2020. A theoretical and experimental exploration of the seismic dynamics of multi-span bridges. *Bulletin of Earthquake Engineering*.

MITSEAS, I. P., KOUGIOUMTZOGLOU, I. A., GIARALIS, A. & BEER, M. 2018. A novel stochastic linearization framework for seismic demand estimation of hysteretic MDOF systems subject to linear response spectra. *Structural Safety,* 72**,** 84-98.

MONTEIRO, R., MARQUES, M., ADHIKARI, G., CASAROTTI, C. & PINHO, R. 2014. Spectral reduction factors evaluation for seismic assessment of frame buildings. *Engineering structures,* 77**,** 129-142.

MONTI, G., NUTI, C. & PINTO, P. E. 1996. Nonlinear response of bridges under multisupport excitation. *Journal of Structural Engineering,* 122**,** 1147-1159.

MORÉ, J. J. 1978. The Levenberg-Marquardt algorithm: implementation and theory. *Numerical analysis.* Springer.

NAZMY, A. S. & ABDEL-GHAFFAR, A. M. 1992. Effects of ground motion spatial variability on the response of cable-stayed bridges. *Earthquake Engineering & Structural Dynamics,* 21**,** 1-20.

NING, C.-L., WANG, L. & DU, W. 2019. A practical approach to predict the hysteresis loop of reinforced concrete columns failing in different modes. *Construction and Building Materials,* 218**,** 644-656.

NORMAN, J. & CREWE, A. Development and control of a novel test rig for performing multiple support testing of structures. Proceedings of the 14th world conference on earthquake engineering, Beijing, paper, 2008. 0051.

NORMAN, J., VIRDEN, D., CREWE, A. & WAGG, D. Physical Modelling of bridges subject to multiple support excitation. 8th National conference on earthquake engineering, San Francisco, California, US, Paper, 2006.

NORMAN, J. A. 2006. *Multiple support excitation of long span bridges: an experimental and numerical study.* University of Bristol.

OLIVEIRA, C. S., HAO, H. & PENZIEN, J. 1991. Ground motion modeling for multiple-input structural analysis. *Structural Safety,* 10**,** 79-93.

PAPADOPOULOS, S. P. & SEXTOS, A. G. 2018. Anti-symmetric mode excitation and seismic response of base-isolated bridges under asynchronous input motion. *Soil Dynamics and Earthquake Engineering,* 113**,** 148-161.

PARASKEVA, T., KAPPOS, A. & SEXTOS, A. 2006. Extension of modal pushover analysis to seismic assessment of bridges. *Earthquake engineering & structural dynamics,* 35**,** 1269-1293.

PRICE, T. E. & EBERHARD, M. O. 1998. Effects of spatially varying ground motions on short bridges. *Journal of Structural Engineering,* 124**,** 948-955.

PRIESTLEY, M. 2000. Performance based seismic design. *Bulletin of the New Zealand society for earthquake engineering,* 33**,** 325-346.

RAYLEIGH, J. W. S. B. 1896. *The theory of sound*, Macmillan.

ROBERTS, J. B. & SPANOS, P. D. 2003. *Random vibration and statistical linearization*, Courier Corporation.

SEXTOS, A. G. & KAPPOS, A. J. 2009. Evaluation of seismic response of bridges under asynchronous excitation and comparisons with Eurocode 8-2 provisions. *Bulletin of Earthquake Engineering,* 7**,** 519.

SEXTOS, A. G., KAPPOS, A. J. & PITILAKIS, K. D. 2003a. Inelastic dynamic analysis of RC bridges accounting for spatial variability of ground motion, site effects and soil–structure interaction phenomena. Part 2: Parametric study. *Earthquake Engineering & Structural Dynamics,* 32**,** 629-652.

SEXTOS, A. G., PITILAKIS, K. D. & KAPPOS, A. J. 2003b. Inelastic dynamic analysis of RC bridges accounting for spatial variability of ground motion, site effects and soil–structure interaction phenomena. Part 1: Methodology and analytical tools. *Earthquake engineering & structural dynamics,* 32**,** 607-627.

SHINOZUKA, M. & DEODATIS, G. 1991. Simulation of stochastic processes by spectral representation.

SIVASELVAN, M. V. & REINHORN, A. M. 2000. Hysteretic models for deteriorating inelastic structures. *Journal of Engineering Mechanics,* 126**,** 633-640.

SÖDERSTRÖM, T. & STOICA, P. 1988. *System identification*, Prentice-Hall, Inc.

SONG, J. & DER KIUREGHIAN, A. 2006. Generalized Bouc–Wen model for highly asymmetric hysteresis. *Journal of engineering mechanics,* 132**,** 610-618.

SOYLUK, K. 2004. Comparison of random vibration methods for multi-support seismic excitation analysis of long-span bridges. *Engineering Structures,* 26**,** 1573-1583.

SPANOS, P. D. & GIARALIS, A. 2013. Third-order statistical linearization-based approach to derive equivalent linear properties of bilinear hysteretic systems for seismic response spectrum analysis. *Structural Safety,* 44**,** 59-69.

TZANETOS, N., ELNASHAI, A. S., HAMDAN, F. H. & ANTONIOU, S. 2000. Inelastic

dynamic response of RC bridges subjected to spatial non-synchronous earthquake motion. *Advances in structural engineering,* 3**,** 191-214.

VAMVATSIKOS, D. & CORNELL, C. A. 2002. Incremental dynamic analysis. *Earthquake Engineering & Structural Dynamics,* 31**,** 491-514.

WAGG, D. & NEILD, S. 2010. Nonlinear Vibration with Control: For Flexible and Adaptive Structures. Solid mechanics and its applications. *Cham, Switzerland: Springer*.

WELCH, P. 1967. The use of fast Fourier transform for the estimation of power spectra: a method based on time averaging over short, modified periodograms. *IEEE Transactions on audio and electroacoustics,* 15**,** 70-73.

WEN, Y.-K. 1976. Method for random vibration of hysteretic systems. *Journal of the engineering mechanics division,* 102**,** 249-263.

YASHINSKY, M. & OSTROM, T. 2000. Caltrans' new seismic design criteria for bridges. *Earthquake spectra,* 16**,** 285-307.

YE, J., ZHANG, Z. & CHU, Y. 2011. Strength behavior and collapse of spatial-reticulated structures under multi-support excitation. *Science China Technological Sciences,* 54**,** 1624.

ZANARDO, G., HAO, H. & MODENA, C. 2002. Seismic response of multi-span simply supported bridges to a spatially varying earthquake ground motion. *Earthquake engineering & structural dynamics,* 31**,** 1325-1345.

ZAPICO-VALLE, J. L., ALONSO-CAMBLOR, R., GONZÁLEZ-MARTÍNEZ, M. P. & GARCÍA-DIÉGUEZ, M. 2010. A new method for finite element model updating in structural dynamics. *Mechanical Systems and Signal Processing,* 24**,** 2137-2159.

ZAPICO, J., GONZALEZ, M., FRISWELL, M., TAYLOR, C. & CREWE, A. 2003. Finite element model updating of a small scale bridge. *Journal of Sound and Vibration,* 268**,** 993-1012.

ZERVA, A. 1990. Response of multi-span beams to spatially incoherent seismic ground motions. *Earthquake Engineering & Structural Dynamics,* 19**,** 819-832.

ZERVA, A. 1991. Effect of spatial variability and propagation of seismic ground motions on the response of multiply supported structures. *Stochastic Structural Dynamics 2.* Springer.

ZERVA, A. 2016. *Spatial variation of seismic ground motions: modeling and engineering applications*, Crc Press.

ZERVA, A. & HARADA, T. 1997. Effect of surface layer stochasticity on seismic ground motion coherence and strain estimates. *Soil Dynamics and Earthquake Engineering,* 16**,** 445-457.

ZERVA, A. & SHINOZUKA, M. 1991. Stochastic differential ground motion. *Structural Safety,* 10**,** 129-143.

ZERVA, A. & ZERVAS, V. 2002. Spatial variation of seismic ground motions: an overview. *Applied Mechanics Reviews,* 55**,** 271-297.

ZHAO, B., WANG, Y., CHEN, Z., SHI, Y., JIANG, Y. & WANG, Y. 2015. Research on

the random seismic response analysis for multi-and large-span structures to multi-support excitations. *Earthquake Engineering and Engineering Vibration,* 14**,** 527-538.

ZHOU, W. & CHELIDZE, D. 2008. Generalized eigenvalue decomposition in time domain modal parameter identification. *Journal of Vibration and Acoustics,* 130.